Search for the decay $B_s^0 \to \eta\eta$ at $\Upsilon(5S)$ resonance

Kamal Jyoti Nath

A thesis
submitted for the degree of
Doctor of Philosophy

Department of Physics
Indian Institute of Technology Guwahati
Guwahati 781039, India

February 2019

Search for the decay $B_s^0 \to \eta\eta$ at $\Upsilon(5S)$ resonance

Kamal Jyoti Nath

A thesis
submitted for the degree of
Doctor of Philosophy

Supervisor:
Prof. Bipul Bhuyan

Department of Physics
Indian Institute of Technology Guwahati
Guwahati 781039, India

October 2018

Declaration

The work in this thesis is based on research carried out at the Department of Physics, Indian Institute of Technology Guwahati, India under the supervision of Prof. Bipul Bhuyan. No part of this thesis has been submitted elsewhere for the award of any other degree or qualification. Works presented in this thesis are entirely my own unless referenced to the contrary in the text.

Signed: Kamaljyoti Nath.

Date: 08/02/19.

Prof. Bipul Bhuyan
Department of Physics
Indian Institute of Technology Guwahati
Guwahati - 781039, INDIA
Email: bhuyan@iitg.ac.in

CERTIFICATE

It is certified that the work contained in the thesis entitled " ***Search for the decay $B_s^0 \to \eta\eta$ at $\Upsilon(5S)$ resonance***" by Mr. Kamal Jyoti Nath, a PhD student of the Department of Physics, IIT Guwahati was carried out under my supervision and has not been submitted elsewhere for award of any degree.

Bipul Bhuyan

Date: 06/02/2019

Prof. Bipul Bhuyan

Acknowledgements

At first, I want to express my sincere gratitude to my supervisor Prof. Bipul Bhuyan for his guidance, motivation and continuous support during my research work. I am thankful to him for giving me the opportunity to work in the international collaboration, Belle, with a group of renowned physicists around the world. I will always remember his help during my visits to Japan, U.S.A., research institutes and in attending various conferences, workshops and schools.

I am also thankful to my doctoral committee members Prof. Poulose Poulose , Dr. Arunansu Sil and Prof. Sreedeep S. for reviewing my progress and for giving me their frank comments and suggestions. I am also thankful to all the faculty members, staff and all other members of Physics Department for their friendly behavior. I express my gratitude to the members of high energy physics group.

I am grateful to the entire Belle and Belle II collaboration members for getting the opportunity to work with them. I am thankful to Kay Kinoshita, convener, Roman Mizuk, co-convener of the $\Upsilon(5S)$ group of the Belle collaboration and all other members of the group for their valuable comments and suggestions on my analysis. I am also thankful to the entire members of the Belle India collaboration for their help and support.

I am thankful to my referees Vipin Gaur, Luo Tau and Takeo Kawasaki for reviewing my analysis and for their valuable suggestions which helped me to complete this analysis in time.

I thank Shohei Nishida for his guidance, help and support on my work on Belle II ARICH detector at KEK, Japan and help in various analysis related issues. I am also thankful to all other members of the ARICH detector group for their help and support. I want to thank Takanori Hara for his help and guidance during my Monte Carlo shifts for Belle II and all other helps during my Ph.D period. My sincere thanks extend to my colleagues in the collaboration who were responsible for data taking, maintaining the quality of data and for the maintenance of the KEK computing resources.

I am thankful to Prof. Yoshihide SAKAI for giving me the invitation to visit KEK, High Energy Research Organization, Japan to work on the Belle and Belle

II experiments. I am thankful to the Belle secretaries and other members of KEK family for their help and cooperation during my stay in Japan.

I am thankful to my senior, Dr. Deepanwita Dutta for her help during my Ph.D period. I am thankful to my lab mates Nitin, Deepanjali, Maharnab, Dibya, Devender and Jyotirmoy for creating a pleasant work environment and for helping me throughout my PhD career. I am thankful to my friends Biswa Ranjan, Kamal Dutta, Bipul, Ranjan, Hemen, Bhrigu and others for their friendly behaviour and cooperation. We spent many enjoyable moments together which I will always treasure. I am thankful to my Belle collaboration friends Abdul, Prasanth, Nibedita, Subhashree, Vipin, Saurav, Varghese and others for various analysis related discussions. I thank all my teachers whose efforts and blessings have helped me to reach here.

I am extremely grateful to my brother, sisters and brother in laws for their love, care, support and encouragement throughout my life. I thank them for staying beside me in my good and bad days. I want to simply thank to my paramour, Munmi, for her love, care and support. I thank my well wishers and all people who have helped me directly or indirectly, whose name I may have inadvertently forgotten.

I am thankful to Ministry of Human Resource Development (MHRD) and Department of Science and Technology (DST), India for providing me financial support to carry on my research work. I am thankful to DST for supporting my KEK, Japan visit. I am also thankful to Science and Engineering Research Board, DST, India for the International Travel Support to present our research work at ICHEP 2016, Chicago, U.S.A..

Last but not the least, I want to thank entire IITG family for providing such a beautiful and enjoyable campus to carry out academic works. I will dearly miss this campus.

Abstract

We search for the decay $B_s^0 \to \eta\eta$ *using 121.4*fb^{-1} *of data collected at* $\Upsilon(5S)$ *resonance by the Belle detector at the KEKB asymmetric energy* e^+e^- *collider located at the High Energy Accelerator Research Organization, Japan. In the Standard Model (SM), this decay is a neutral charmless decay which can occur through a variety of processes such as Cabibbo suppressed* $b \to u$ *transition with a further color suppression with respect to the charged modes. Contributions can also arise from electroweak penguins. It has been studied theoriticaly in the framework of SCET, PQCD and QCDF. The predictions of the branching ratio (BR) of the decay are* $(8.0^{+2.6+4.7+0.0}_{-1.9-2.5-0.0}) \times 10^{-6}$, $(15.6^{+1.6+9.9+2.2+13.5}_{-1.5-6.8-2.5-5.5}) \times 10^{-6}$ *and* $(7.1 \pm 6.4 \pm 0.2 \pm 0.8) \times 10^{-6}$, *respectively. All of these predictions have large uncertainties, which are mostly due to the QCD uncertainties. The present experimental upper limit on the BR for* $B_s \to \eta\eta$ *is* 1.5×10^{-3} *at* 90% *confidence level (CL). This analysis will be the first attempt to search for this decay using the available dataset from the Belle experiment with an expectation of reaching the SM sensitivity.*

Preface

This thesis reports the search for the decay $B_s^0 \to \eta\eta$ at high energy e^+e^- collisions at Υ(5S) energy. In the Standard Model (SM), this decay is a neutral charmless decay which can occur through a variety of processes such as Cabibbo suppressed $b \to u$ transition with a further color suppression with respect to the charged modes. Contributions can also arise from electroweak penguins. It has been studied theoritically in the framework of SCET, PQCD and QCDF. The predictions of the branching ratio (BR) of the decay are $(8.0^{+2.6+4.7+0.0}_{-1.9-2.5-0.0}) \times 10^{-6}$, $(15.6^{+1.6+9.9+2.2+13.5}_{-1.5-6.8-2.5-5.5}) \times 10^{-6}$ and $(7.1 \pm 6.4 \pm 0.2 \pm 0.8) \times 10^{-6}$, respectively. All of these predictions have large uncertainties, which are mostly due to the QCD uncertainties. The present experimental upper limit on the BR for $B_s \to \eta\eta$ is 1.5×10^{-3} at 90% confidence level (CL). This analysis will be the first attempt to search for this decay using the available dataset from the Belle experiment with an expectation of reaching the SM sensitivity.

This thesis presents the results of the search for the decay $B_s^0 \to \eta\eta$ at high energy e^+e^- collisions. The search is done using $121.4 fb^{-1}$ of data collected by the Belle detector at $\Upsilon(5S)$ energy. No significant signal yield is observed for the decay $B_s^0 \to \eta\eta$ and in the absence of any significant signal yield, we set the 90% CL UL on its BF to be 56.53×10^{-6}. This is an improvement of about two orders of magnitude from the previous measurement of UL by the L3 experiment. With a dedicated run at $\Upsilon(5S)$ resonance to collect an order of magnitude more statistics, the Belle II experiment has the potential to make a discovery of the charmless $B_s^0 \to \eta\eta$ decay. LHCb has the limitation in the measurement of the BF for this decay since the reconstruction of η and π^0 candidates require detection of single energy clusters in the calorimeter, which may be difficult at LHCb.

This thesis contains the following chapters:

Chapter 1 provides an introduction to the SM of particle physics, the dynamics of electroweak and strong interaction and the associated gauge transformations. It then provides a brief overview of Cabibbo-Kobayashi-Maskawa (CKM) matrix, GIM mechanism and FCNC processes. A brief introduction to renormalization and effective field theory is then presented. Various analysis techniques namely, PQCD, SCET and the QCDFi are discussed briefly. This chapter concludes with a brief discussion on the current status of the decay $B_s^0 \to \eta\eta$.

Chapter 2 provides a brief discussion on KEKB accelerator, the Belle detector, data acquisition and the trigger system.

Chapter 3 provides a description of the analysis strategy, the Belle datasets, Monte Carlo event generation procedure and the blind analysis technique used to study the decay $B_s^0 \to \eta\eta$. The skim, candidate and signal selection criteria for these analyses are then discussed. Possible backgrounds are analyzed, and their suppression studied and discussed in details in this chapter.

Chapter 4 presents the PDF parameterizations of signal and background for $B_s^0 \to \eta\eta$ analysis. It provides a brief discussion on the fit strategy for both the analyses. Pesudo-experiments are then performed to test the stability of the fitters. This chapter presents the results of these pseudo-experiments. The final fit results are then presented.

Chapter 5 provides a brief discussion on systematic uncertainties. Various sources of systematic uncertainties and their estimation procedure are discussed in details in this chapter.

Chapter 6 summarizes the final results for $B_s^0 \to \eta\eta$ analysis. The estimation of 90% CL upper limit for the decay $B_s^0 \to \eta\eta$ is presented in details in this chapter. This chapter concludes with a brief discussion on the possible implications of the results of this analysis.

Contents

List of Figures

List of Tables

Chapter 1

Theoretical Framework and Motivations

This chapter provides a brief introduction to the Standard Model (SM) of particle physics, the dynamics of strong and electroweak interactions and the associated gauge transformations. It then provides a brief overview of Cabibbo-Kobayashi-Maskawa (CKM) matrix and flavor changing processes. A brief introduction to effective field theory (EFT) and various analysis techniques used in the study of the rare decays are also presented. This thesis is devoted to the study of the rare decay $B_s^0 \to \eta\eta$. Precision measurements of the rare decays allow us to access new particles produced virtually through loop processes, thus providing a way to search for new physics and test the SM at higher energy scales. This chapter concludes with a brief discussion on the present status of the studies of such rare process.

1.1 The Standard Model of Particle Physics

High Energy Physics tries to understand the fundamental building blocks of Nature and their interactions. The most successful explanation comes through SM, which is formulated using relativistic quantum field theory that describes and unifies the three of the four known fundamental interactions namely, electromagnetic, weak and strong interaction using Gauge symmetry. According to this model, the basic building blocks of Nature are the quarks and the leptons (fermions) and they interact with each other through three kind of forces: EM, weak and strong. The interactions happen through the exchange of the Gauge bosons: the boson that mediates the EM interaction is called photon which is massless whereas the weak interaction is mediated by the massive bosons, $W^\pm$ and Z^0; the strong interaction is mediated by gluons. The Gauge symmetry of the SM is represented by $SU(3)_C \otimes SU(2)_L \otimes U(1)_Y$ group. The group $SU(3)_C$ represents the strong interaction and is formed by color charges. The group $SU(2)_L$ represents the weak interaction and is formed by the weak isospin which governs how quarks and leptons behave during weak interaction. $U(1)_Y$ group describes the EM interaction and is formed by another quantum number called hypercharge.

Gauge invariance refers to continuous transformations under a group $\mathcal{G}$, which leaves the Lagrangian (or the system) invariant. The simplest of such transformation is $\psi \mapsto \psi' = e^{-i\beta}\psi$, where ψ is a fermion field and β is a constant (this is a transformation belonging to the global $U(1)$ group). The Lagrangian density of massless fermion fields, given by:

$$\mathcal{L} = \bar{\psi} i\gamma^\mu \partial_\mu \psi \tag{1.1}$$

is invariant under this transformation (i.e., $\mathcal{L}' = e^{-i\beta}\mathcal{L} = \mathcal{L}$) since the observables depend on $|\psi|^2$. For local $U(1)$ symmetry (e.g., the electromagnetic field) when we introduce a space-time dependence on ψ ($\psi \mapsto e^{-i\chi(x,t)}\psi$), the Lagrangian is not invariant anymore, but can be made invariant by replacing the derivative ∂_μ by a covariant derivative D_μ defined by:

$$D_\mu \equiv \partial_\mu - igA_\mu(x) \tag{1.2}$$

where g is a constant (coupling constant) and A_μ is a $U(1)$ gauge field. This formalism can be extended to more complicated groups like $SU(2)$ and $SU(3)$ (non-abelian groups), by introducing the corresponding generators in the transformations and organizing the fermions in multiplets of gauge groups. The full covariant derivative incorporating the electromagnetic, weak and strong interactions [3] can be written as:

$$D_\mu \equiv \partial_\mu - ig_1\frac{Y}{2}F_\mu(x) - ig_2\frac{\tau^i}{2}.W_\mu^i - ig_3\frac{\lambda^a}{2}.G_\mu^a \tag{1.3}$$

where, F_μ, W_μ and G_μ are the spin-1 gauge fields that represent the electromagnetic, weak and strong interaction, respectively. τ^i's (i=1,2,3) and λ^a's (a=1,...,8) are the generators of $SU(2)$ and $SU(3)$ groups representing the weak and strong force respectively. Y (which is just a number) is the $U(1)$ hypercharge generator and g's are the coupling constants for various interactions. For $SU(2)$ and $SU(3)$ symmetry, ψ transforms like $\psi \mapsto \psi' = e^{-i\vec{\epsilon}.\vec{\tau}/2}$ and $\psi \mapsto \psi' = e^{-i\vec{\alpha}.\vec{\lambda}/2}$, where ϵ's and α's denote the rotation parameters of $SU(2)$ and $SU(3)$ space.

The SM Lagrangian [4, 5] can be written as:

$$\boxed{\mathcal{L}^{4}_{\mathrm{SM}} = \mathcal{L}_{\mathrm{QCD}} + \mathcal{L}_{\mathrm{ew}} + \mathcal{L}_{H} + \mathcal{L}_{\mathrm{Yu}}} \tag{1.4}$$

The superscript (4) indicates that the Lagrangian has mass dimensions 4.

$\mathcal{L}_{\mathrm{QCD}}$ is the quantum chromodynamics (QCD) Lagrangian [3–5] given as:

$$\boxed{\mathcal{L}_{\mathrm{QCD}} = \sum_{j} \bar{q}_j i\gamma^{\mu}\left(\partial_\mu - i\frac{g_3}{2}\vec{\lambda}.\vec{G}_\mu\right) q_j - \frac{1}{4}\, G^{a}_{\mu\nu} G^{\mu\nu}_{a}} \tag{1.5}$$

which describes the color interaction between quarks and gluons, with $SU(3)$ symmetry. Here, q_j is a color triplet quark field (the index j runs over the 6 flavors) and $G^{a}_{\mu\nu}$'s are the strength tensors of 8 gluon fields $\vec{G}_\mu$, expressed as:

$$G^{a}_{\mu\nu} = \partial_\mu G^{a}_{\nu} - \partial_\nu G^{a}_{\mu} - g_3 f^{abc} G^{b}_{\mu} G^{c}_{\nu}$$

where, f^{abc} is the structure constant corresponding to $SU(3)$ interaction.

$\mathcal{L}_{\mathrm{ew}}$ represents the electroweak Lagrangian term [3–5] that describes the interactions between fermions and vector bosons through the symmetry groups $SU(2)_L \otimes U(1)_Y$ which can be written as:

$$\boxed{\mathcal{L}_{\mathrm{ew}} = \sum_{i} \bar{\psi}^{i} i\gamma^{\mu}\left(\partial_\mu - i\frac{g_1}{2} Y_W F_\mu - i\frac{g_2}{2}\vec{\tau}.\vec{W}_\mu\right)\psi_i - \frac{1}{4} F_{\mu\nu} F^{\mu\nu} - \frac{1}{4} W^{j}_{\mu\nu} W_{j}^{\mu\nu}} \tag{1.6}$$

ψ^i represents the fermion wave functions and are represented in terms of $SU(2)$ left handed doublets (ψ_L) and right handed singlets (ψ_R) as:

$$\psi_L \in \left\{ \begin{pmatrix} \nu_e \\ e^- \end{pmatrix}_L, \begin{pmatrix} \nu_\mu \\ \mu^- \end{pmatrix}_L, \begin{pmatrix} \nu_\tau \\ \tau^- \end{pmatrix}_L, \begin{pmatrix} u' \\ d' \end{pmatrix}_L, \begin{pmatrix} c' \\ s' \end{pmatrix}_L, \begin{pmatrix} t' \\ b' \end{pmatrix}_L \right\},$$

$$\psi_R \in \left\{ e_R, \mu_R, \tau_R, q_R \right\} \quad \text{where, } q \in \left\{ u', d', c', s', t', b' \right\}.$$

Here, the quarks are represented with primed symbols since the electroweak eigenstates don't necessarily coincide with the mass eigenstates. $F_{\mu\nu}$ and $W^i_{\mu\nu}$'s are the strength tensors of the photon field $\overrightarrow{F}_\mu$ and 3 weak boson fields $\overrightarrow{W}_\mu$ given as:

$$\begin{aligned} F_{\mu\nu} &= \partial_\mu F_\nu - \partial_\nu F_\mu \quad \text{and} \\ W^i_{\mu\nu} &= \partial_\mu W^i_\nu - \partial_\nu W^i_\mu - g_2 \Sigma^{ijk} W^j_\mu W^k_\nu \end{aligned}$$

where, Σ^{ijk} is the structure constant corresponding to the $SU(2)$ interaction. The first term of equation 1.6 is the fermion boson interaction term [5, 6] and is given by:

$$\mathcal{L}_{\text{int,ew}} = \mathcal{L}_{\text{CC}} + \mathcal{L}_{\text{NC}} = \frac{g_2}{\sqrt{2}} \left(j_L^{\mu+} W_\mu^+ + j_L^{\mu-} W_\mu^- \right) + \left(e j^\mu_{\text{em}} F_\mu + g_z j^\mu_Z Z_\mu \right) \qquad (1.7)$$

where, $e = g_1$ is the electromagnetic coupling constant; $g_z = \frac{g_2}{2\cos\theta_W}$ is the weak coupling constant corresponding to the Z boson with $\sin\theta_W = \frac{g_1}{\sqrt{g_1^2 + g_2^2}}$ and $\cos\theta_W = \frac{g_2}{\sqrt{g_1^2 + g_2^2}}$, θ_W being the Weinberg angle; $j^\mu_{\text{em}} = \sum_f e\bar{f}\gamma^\mu f$ and $j^\mu_Z = \sum_f \bar{f}\gamma^\mu (g^f_v - g^f_A \gamma^5) f$ are the neutral currents carried by the photon (γ) and Z boson, respectively with $g^f_v = I^3_f - 2q_f \sin^2\theta_W$ and $g^f_A = I^3_f$ where, 'f' represents the fermion states; q_f and I^3_f denote the charge and the third component of weak isospin respectively. The terms:

$$j_L^{\mu+} = \left(\bar{u}'_L \gamma^\mu d'_L + \bar{c}'_L \gamma^\mu s'_L + \bar{t}'_L \gamma^\mu b'_L + \sum_l \nu_{lL} \gamma^\mu l_L \right) \quad \text{and} \quad j_L^{\mu^-} = \left(j_L^{\mu^+} \right)^\dagger$$

are the left handed (charged) currents carried by the physical bosons $W^\pm$. The physical bosons $W^\pm$ and Z can be written in terms of generators of weak interaction as:

$$W^\pm_\mu = \frac{W^1_\mu \mp i W^2_\mu}{\sqrt{2}}, \quad Z_\mu = W^3_\mu.$$

The Higgs term in the SM Lagrangian is required to account for the masses of the fermions and the gauge bosons. The Higgs Lagrangian [3, 5] has the form:

$$\boxed{\mathcal{L}_H = (D_\mu\phi\dagger)(D^{\mu}\phi) - V(\phi) \equiv (D_\mu\phi\dagger)(D^{\mu}\phi) - M^2\phi^\dagger\phi - \Lambda\ (\phi^\dagger\phi)^2} \tag{1.8}$$

Here, the first term $(D_\mu\phi\dagger)(D^{\mu}\phi)$ represents the dynamical Higgs term and $V(\phi) = M^2\phi^\dagger\phi - \Lambda\ (\phi^\dagger\phi)^2$ denotes the Higgs potential. M and Λ are the parameters in the Higgs potential. The field ϕ is a complex spinor (doublet) representing the Higgs field, while the Higgs particle mass is given as $m_H = \sqrt{2\Lambda^2\mathfrak{v}^2} = \sqrt{-M^2}$, where $\mathfrak{v}$ is the vacuum expectation value of the field ϕ.

The Yukawa term [3] describes the interaction of Higgs field with the matter fields. It is of the form:

$$\begin{aligned}\boxed{\mathcal{L}_{\mathrm{Yu}} = Y_{i,j}^{\,u}\ (\bar{Q}'_{Li}\tilde{\phi})\ u'_{Rj} + Y_{i,j}^{\,d}\ (\bar{Q}'_{Li}\phi)\ d'_{Rj} + Y_{i,j}^{\,e}\ (\bar{Q}'_{Li}\phi)\ e'_{Rj} + h.c.} \\ = Y_{i,j}^{\,u}(\bar{u}'_{Li}\frac{\mathfrak{v}}{\sqrt{2}})\ u'_{Rj} + Y_{i,j}^{\,d}\ (\bar{d}'_{Li}\frac{\mathfrak{v}}{\sqrt{2}})\ d'_{Rj} + Y_{i,j}^{\,e}\ (\bar{e}'_{Li}\frac{\mathfrak{v}}{\sqrt{2}})\ e'_{Rj} + h.c.\end{aligned} \tag{1.9}$$

where, $\tilde{\phi} = i\tau_2\phi$. The Yukawa matrices (couplings) $Y^{u,d,e}$ are arbitrary 3×3 complex matrices for the three generations (i, j) of quarks; $h.c.$ represents the Hermitian conjugate.

Thus, the SM Lagrangian ($\mathcal{L}_{\mathrm{SM}}^{(4)}$) represented by equation 1.4 can be written as:

$$\boxed{\begin{aligned}\mathcal{L}_{\mathrm{SM}}^{4} = -\frac{1}{4}\, G_{\mu\nu}^{\,a}G_{a}^{\,\mu\nu} - \frac{1}{4}\, W_{\mu\nu}^{\,j}W_{j}^{\,\mu\nu} - \frac{1}{4}\, F_{\mu\nu}F^{\,\mu\nu} + \Big[(D_\mu\phi\dagger)(D^{\mu}\phi) - \\ M^2\phi^\dagger\phi - \lambda\ (\phi^\dagger\phi)^2\Big] + i\left(\bar{l}\not{D}l + \bar{e}\not{D}e + \bar{q}\not{D}q + \bar{u}\not{D}u + \bar{d}\not{D}d\right) \\ - \Big[Y_{i,j}^{\,u}\ (\bar{Q}'_{Li}\tilde{\phi})\ u'_{Rj} + Y_{i,j}^{\,d}\ (\bar{Q}'_{Li}\phi)\ d'_{Rj} + Y_{i,j}^{\,e}\ (\bar{Q}'_{Li}\phi)\ e'_{Rj} + h.c.\Big]\end{aligned}} \tag{1.10}$$

The Yukawa couplings give rise to lepton and quark masses. Thus, $M^u_{ij} = \mathfrak{v}Y^u_{ij}/\sqrt{2}$, $M^d_{ij} = \mathfrak{v}Y^d_{ij}/\sqrt{2}$ and $M^e_{ij} = \mathfrak{v}Y^e_{ij}/\sqrt{2}$. Therefore,

$$\begin{aligned}\mathcal{L}_{Yu} &= \bar{u}'_{Li}M^u_{ij}u'_{Rj} + \bar{d}'_{Li}M^d_{ij}d'_{Rj} + \bar{e}'_{Li}M^e_{ij}e'_{Rj} + h.c. \\ &= \bar{u}'_{Li}(V^{u\dagger}_L V^u_L)M^u_{ij}(V^{u\dagger}_R V^u_R)u'_{Rj} + \bar{d}'_{Li}(V^{d\dagger}_L V^d_L)M^d_{ij}(V^{d\dagger}_R V^d_R)d'_{Rj} \\ &\qquad + \bar{e}'_{Li}(V^{e\dagger}_L V^e_L)M^e_{ij}(V^{e\dagger}_R V^e_R)e'_{Rj} + h.c.\end{aligned}$$

The matrices M^u, M^d and M^e should be diagonalized using unitary matrices V^u, V^d and V^e as:

$$M^d_{\text{diag}} = V^d_L M^d V^{d\dagger}_R, \quad M^u_{\text{diag}} = V^u_L M^u V^{u\dagger}_R \quad \text{and} \quad M^e_{\text{diag}} = V^e_L M^e V^{e\dagger}_R$$

to obtain the proper mass terms. The mass eigenstates $(u,d)_{L,R}$ can thus be written in terms of interaction eigenstates $(u,d)'_{L,R}$ as: $(u,d)_{Li} = (V^{u,d}_L)_{ij}(u,d)'_{Lj}$ and $(u,d)_{Ri} = (V^{u,d}_R)_{ij}(u,d)'_{Rj}$. Therefore,

$$\boxed{\boldsymbol{\mathcal{L}_{\text{Yu}} = \bar{u}_{Li}(M^u_{ij})_{\text{diag}}u_{Rj} + \bar{d}_{Li}(M^d_{ij})_{\text{diag}}d_{Rj} + \bar{e}_{Li}(M^e_{ij})_{\text{diag}}e_{Rj} + h.c.}} \tag{1.11}$$

Unfortunately, when introducing a mass term in the Lagrangian, the $SU(2) \otimes U(1)$ symmetry is spontaneously broken to electromagnetic $U(1)_{\text{QED}}$. This is called spontaneous symmetry breaking (SSB) [4].

$$\boxed{\boldsymbol{SU(3)_C \otimes SU(2)_L \otimes U(1)_Y \xrightarrow{\text{SSB}} SU(3)_C \otimes U(1)_{\text{QED}}}} \tag{1.12}$$

The SM Lagrangian after SSB, can be obtained by replacing the Yukawa term in equation 1.10 by equation 1.11.

At present, only 3 generations of quarks and leptons have been observed. 4 or more generations of quarks are considered to be unlikely as this will induce slight modifications to various electroweak observables which are strongly disfavored by experimental measurements [7]. Furthermore, the measured width of the Z boson rules out a fourth quark generation with a 'light' neutrino (neutrino having mass less than about 45 GeV/c^2) [8–10].

During the last few decades, many experimental studies have been performed in order to test the validity of the SM and so far no large discrepancies have been found. Also the SM has so far been successful in explaining the vast amount of existing experimental data. However, the SM provides poor explanations for the flavor dependence of particle properties (mass, number of families, etc), hierarchical structure of CKM matrix, matter-antimatter asymmetry [8, 11], existence of dark matter [8, 12] and the presence of symmetries like conservation of baryon and lepton numbers [8]. Further, it couldn't account for the neutrino oscillations [8, 13]. Neutrinos are considered to be massless in the SM. However, the observation of neutrino mixing indicates that they are massive. Whether the SM is an approximation of a more general theory, valid in some scales still needs to be ascertained. Answering these questions requires probing matter up to very small distances, which requires high energies through particle colliders or either precision measurements rare processes at the intensity frontier.

1.2 Flavor Changing Process: CKM matrix

The charged current term of the electroweak interaction Lagrangian (equation 1.7) is given by:

$$\mathcal{L}_{CC} = \frac{g_2}{\sqrt{2}}\left(j_L^{\mu+} W_\mu^+\right) + h.c., \text{ where } j_L^{\mu+} = \sum_{ij} \bar{u}'_i \gamma^\mu \left(\frac{1-\gamma^5}{2}\right) d'_j + \sum_i \bar{\nu}_i \gamma^\mu \left(\frac{1-\gamma^5}{2}\right) e_i$$

and the neutral current term (mediated by the Z boson) is given by:

$$(\mathcal{L}_{NC})_Z = g_z j_Z^\mu Z_\mu, \text{ where } j_Z^\mu = \sum_f g_L^f \bar{f} \gamma^\mu \left(\frac{1-\gamma^5}{2}\right) f + \sum_f g_R^f \bar{f} \gamma^\mu \left(\frac{1+\gamma^5}{2}\right) f$$

Now,

$$\sum_{ij} \bar{u}'_i \gamma^\mu (1-\gamma^5) d'_j = \begin{pmatrix} \bar{u}' & \bar{c}' & \bar{t}' \end{pmatrix} \gamma^\mu (1 - \gamma^5) \begin{pmatrix} d' \\ s' \\ b' \end{pmatrix}$$

$$= V_{\rm CKM} \, (\, \bar{u} \;\; \bar{c} \;\; \bar{t}\,) \, \gamma^\mu (1 - \gamma^5) \begin{pmatrix} d \\ s \\ b \end{pmatrix} \qquad (1.13)$$

where,

$$\begin{pmatrix} u' \\ c' \\ t' \end{pmatrix} = U_U \begin{pmatrix} u \\ c \\ t \end{pmatrix} \quad \text{and} \quad \begin{pmatrix} d' \\ s' \\ b' \end{pmatrix} = U_D \begin{pmatrix} d \\ s \\ b \end{pmatrix} .$$

$V_{\rm CKM} = U_U^\dagger U_D$ is a unitary matrix known as CKM matrix represented in the standard parametrization [14] as:

$$V_{\rm CKM} = \begin{pmatrix} V_{ud} & V_{us} & V_{ub} \\ V_{cd} & V_{cs} & V_{cb} \\ V_{td} & V_{ts} & V_{tb} \end{pmatrix}$$

$$= \begin{pmatrix} c_{12}c_{13} & s_{12}s_{13} & s_{13}e^{-i\delta} \\ -s_{12}c_{23} - c_{12}s_{23}s_{13}e^{i\delta} & c_{12}s_{23} - s_{12}s_{23}s_{23}e^{i\delta} & s_{23}c_{13} \\ s_{12}c_{23} - c_{12}s_{23}s_{13}e^{i\delta} & -s_{23}c_{12} - s_{12}c_{23}s_{13}e^{i\delta} & c_{23}c_{13} \end{pmatrix} (1.14)$$

where, θ_{12}, θ_{23}, and θ_{13} are the three Euler angles and δ is the CP violating phase. The symbols s_{ij}'s and c_{ij}'s denote the sines and cosines of these angles. θ_{12} is the Cabibbo angle.

In Wolfenstein parametrization [15], the CKM matrix can be written as:

$$V_{\rm CKM} = \begin{pmatrix} 1 - \frac{\lambda^2}{2} & \lambda & A\lambda^3(\rho - i\eta) \\ \lambda & 1 - \frac{\lambda^2}{2} & A\lambda^2 \\ A\lambda^2(1-\rho-i\eta) & -A\lambda^2 & 1 \end{pmatrix} + \mathcal{O}(\lambda^4) \qquad (1.15)$$

where A, λ, ρ and η are the four parameters represented as $s_{12} = \lambda$, $s_{23} = A\lambda^2$ and $s_{13}e^{-i\delta} = A\lambda^3(\rho - i\eta)$. Therefore,

$$\rho = \frac{s_{13}}{s_{12}s_{23}}\cos\delta \quad , \quad \eta = \frac{s_{13}}{s_{12}s_{23}}\sin\delta.$$

The η parameter is the complex phase parameter that is responsible for the CP violation in the SM. $\mathcal{O}(\lambda^4)$ denotes terms of the order of λ^4.

The CKM matrix elements are measured by different experiments. The present best value of them are given below (PDG).

$$V_{\rm CKM} = \begin{pmatrix} 0.974 & 0.225 & 0.003 \\ 0.225 & 0.973 & 0.041 \\ 0.008 & 0.040 & 0.999 \end{pmatrix}, \tag{1.16}$$

We observe non-zero off-diagonal elements in the CKM matrix, which indicates that generation changing charged currents are possible in the SM. The same operation for neutral current interaction for the up-sector yields:

$$(\, \bar{u}' \;\; \bar{c}' \;\; \bar{t}' \,)\, \gamma^\mu (1 - \gamma^5) \begin{pmatrix} u' \\ c' \\ t' \end{pmatrix} = (\, \bar{u} \;\; \bar{c} \;\; \bar{t} \,)\, \gamma^\mu (1 - \gamma^5) U_U^\dagger U_U \begin{pmatrix} u \\ c \\ t \end{pmatrix} \tag{1.17}$$

Unitarity of U_U ensures that $U_U^\dagger U_U = 1$ i.e., there is no generation changing neutral currents in the up-sector. The same holds true for the down-sector (the neutral current terms conserve flavor). Flavor Changing Neutral Current (FCNC) transitions, such as $b \to s$ and $b \to d$ are thus forbidden at tree level in the SM. However, FCNCs are possible at higher orders since, contributions from different quark loops don't cancel exactly due to their different masses. At one loop level, the FCNC transitions can be summarized by a set of basic triple and quartic effective vertices known as penguin diagrams (ΔF = 1, F being the flavor of the quarks) and box diagrams (ΔF = 2), respectively [16, 17]. Penguin processes involve the emission of a neutral boson, either a gluon, photon or Z boson [18]. They can thus be classified into: (i) radiative, in which an external photon is emitted (Figure 1.1(a)), (ii) electroweak, in which the emitted virtual photon or Z boson produce lepton pairs

(Figure 1.1(b)), (iii) annihilation penguin processes, in which the loop connects two quarks of the B meson (Figure 1.1(c) and (d)) and (iv) gluonic penguins, in which a gluon is emitted from the loop (Figure 1.1(e)). Figure 1.1(f) represents the box diagram. Since, FCNC processes occur through box or penguin diagrams, they are suppressed by a loop factor of $g_2^2/16\pi^2 \equiv 10^{-2}$. They are further suppressed due to GIM mechanism [19]. Due to the large suppression in the SM, the FCNC decays are ideal places to look for evidences of new physics. Precision measurements of these rare FCNC processes represent a sensitive probe for new-physics, as many new physics processes or extensions of the SM such as, super-symmetry with multi-Higgs doublets, extra quark models, fourth generation models, extra-dimensions, etc., can enhance or suppress FCNC decay rates [16]. This allows the indirect search for new physics. Measurements of FCNCs are model independent tests of any new-physics model that can contribute to change the overall properties (or observables) of the decay.

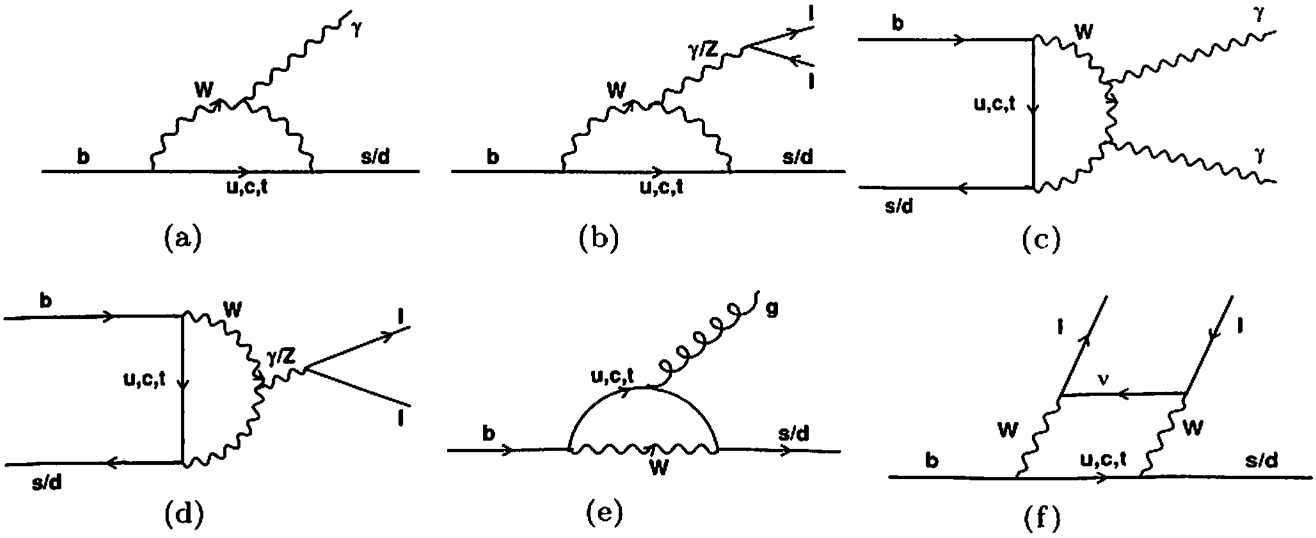

(a) (b) (c)

(d) (e) (f)

FIGURE 1.1: *Examples of FCNC processes.*

(a) Radiative penguin processes e.g., $b \to s\gamma, d\gamma$ *(b) electroweak penguins e.g.,* $b \to sl^+l^-, dl^+l^-$ *(c) annihilation penguins and (d)* $b \to l^+l^-, B_s \to l^+l^-$ *(e) gluonic penguins e.g.,* $b \to sg, dg$ *(f) box diagrams e.g.,* $b \to sl^+l^-, dl^+l^- \text{or} B_{s(d)} \to l^+l^-$.

1.3 Renormalization and Effective Field Theory (EFT)

The basic principle of EFT [6, 17, 20–24] is that the dynamics of elementary particles at low energy doesnot depend on the details of the dynamics at high energies. As a result, physics at low energy scales can be described using an effective Lagrangian that contains only a few degrees of freedom, ignoring the additional degrees of freedom present at higher energies. For example, we do not need to know about the bottom quarks to describe the hydrogen atom. The process of integrating out the (irrelevant) heavy degrees of freedom from 'explicitly' appearing in the theory is called renormalization [6, 25]. The SM is also an EFT. In the absence of knowledge about the full theory, the observables for any decay process can be calculated using EFT. Information about physics beyond the SM can be obtained by comparing the experimental and the EFT result for rare decays. In the framework of an EFT, the Lagrangian can be written as an infinite expansion:

$$\mathcal{L}_{\Lambda}^{eff} = \sum_{i} \frac{C_i(R)}{\Lambda^{d_i-4}} \mathcal{Q}_i \tag{1.18}$$

where, C_i's are dimensionless coefficients called the Wilson coefficients, which are related to the couplings of the full theory; $\mathcal{Q}_i$'s are the operators having dimension d_i's, built out of fields appearing in the theory; Λ is the characteristic energy scale of theory and R is the cutoff scale chosen just below Λ. Since the mass dimension of Lagrangian is 4, operators having mass dimension greater than 4 are numerically suppressed by powers of fundamental scale (i.e., Λ) of the theory. The higher the dimension of the operator, the more it will be suppressed. Thus, the lower dimensional operators are the important ones and the higher dimensional ones can be neglected. Physics from distances smaller than R^{-1} (i.e., contributions from scales higher than R or the high energy interactions) is contained in the Wilson coefficients C_i and that from distances greater than that (i.e., the low energy interactions) are accounted for by the operators. This approach of expressing the Lagrangian in this form is called operator product expansion (OPE) [6, 17, 18, 20–24]. The Wilson coefficients and the local operators, both depend on the renormalization scale R and renormalization scheme. The scale and scheme dependence of C_i's must be cancelled by the similar dependence of operators making the physical observables independent of them. R is typically chosen of the order of the decaying hadron $\mathcal{O}(m_b)$, $\mathcal{O}(m_c)$ and $\mathcal{O}(1-2\text{ GeV})$ for B, D and K mesons. Depending on the precision goal one can truncate the series and thus, only a finite number of operators and couplings need to be retained.

The similarity of FCNC processes, in decays and mixing, allows us to describe all of them in terms of four fermion local operators. At tree level, the leading order effective Lagrangian for the four fermion process can be written as:

$$\mathcal{L}_{4f}^{eff} = \frac{G_F}{\sqrt{2}} J_{L\mu}^{-} J_L^{\mu+} \equiv \frac{G_F}{\sqrt{2}} \sum_i \mathcal{C}_i \mathcal{Q}_i \tag{1.19}$$

where, $\frac{G_F}{\sqrt{2}} \equiv \frac{g_2^2}{8M_W^2}$, G_F being the Fermi constant.

For four-fermion interaction, since each fermion line has a mass dimension of 3/2, so the operators involved in this case should have at least dimension 6. So, a M_W^{-2} scaling law for Wilson coefficients at leading order is needed. Thus, the non-local product of two charged current interactions can be expanded into a series of local operators, whose contributions are weighted by the effective coupling constants. In the SM, the dimension-6 operators can be classified in 6 categories. In the notation of [17]:

Current-Current (Figure 1.2(a))

$$\mathcal{Q}_1 = (\bar{s}_{\alpha L}\gamma_\mu c_{\beta L})\,(\bar{c}_{\beta L}\gamma^\mu b_{\alpha L}) \tag{1.20}$$

$$\mathcal{Q}_2 = (\bar{s}_L\gamma_\mu c_L)\,(\bar{c}_L\gamma^\mu b_L) \tag{1.21}$$

QCD-Penguins (Figure 1.2(b))

$$\mathcal{Q}_3 = (\bar{s}_L\gamma_\mu b_L) \sum_{q=u,d,s,c,b} (\bar{q}_L\gamma^\mu q_L) \tag{1.22}$$

$$\mathcal{Q}_4 = (\bar{s}_{\alpha L}\gamma_\mu b_{\beta L}) \sum_{q=u,d,s,c,b} (\bar{q}_{\beta L}\gamma^\mu q_{\alpha L}) \tag{1.23}$$

$$\mathcal{Q}_5 = (\bar{s}_L\gamma_\mu b_L) \sum_{q=u,d,s,c,b} (\bar{q}_R\gamma^\mu q_R) \tag{1.24}$$

$$\mathcal{Q}_6 = (\bar{s}_{\alpha L}\gamma_\mu b_{\beta L}) \sum_{q=u,d,s,c,b} (\bar{q}_{\beta R}\gamma^\mu q_{\alpha R}) \tag{1.25}$$

Electroweak-Penguins (Figure 1.2(c))

$$Q_{3Q} = \frac{3}{2}\,(\bar{s}_L\gamma_\mu b_L) \sum_{q=u,d,s,c,b} e_q\,(\bar{q}_R\gamma^\mu q_R) \tag{1.26}$$

$$Q_{4Q} = \frac{3}{2}\,(\bar{s}_{L\alpha}\gamma_\mu b_{L\beta}) \sum_{q=u,d,s,c,b} e_q\,(\bar{q}_{R\beta}\gamma^\mu q_{R\alpha}) \tag{1.27}$$

$$Q_{5Q} = \frac{3}{2}\,(\bar{s}_L\gamma_\mu b_L) \sum_{q=u,d,s,c,b} e_q\,(\bar{q}_L\gamma^\mu q_L) \tag{1.28}$$

$$Q_{6Q} = \frac{3}{2}\,(\bar{s}_{L\alpha}\gamma_\mu b_{L\beta}) \sum_{q=u,d,s,c,b} e_q\,(\bar{q}_{L\beta}\gamma^\mu q_{L\alpha}) \tag{1.29}$$

Magnetic-Penguins (Figure 1.2(d))

$$Q_7 = \frac{e}{16\pi^2} m_b \bar{s}_{\alpha L}\sigma^{\mu\nu} b_{\alpha R} F_{\mu\nu} \tag{1.30}$$

$$Q_8 = \frac{g}{16\pi^2} m_b \bar{s}_{\alpha L}\sigma^{\mu\nu} T^a_{\alpha\beta}\, b_{\beta R}\, G^a_{\mu\nu} \tag{1.31}$$

ΔF = 2 (ΔS = 2 or ΔB = 2) Operators (Figure 1.2(e))

$$Q(\Delta S = 2) = (\bar{s}_L\gamma_\mu d_L)\,(\bar{s}_L\gamma^\mu d_L) \tag{1.32}$$

$$Q(\Delta B = 2) = (\bar{b}_L\gamma_\mu d_L)\,(\bar{b}_L\gamma^\mu d_L) \tag{1.33}$$

Semi-Leptonic Operators (Figure 1.2(f))

$$Q_9 = \frac{e^2}{16\pi^2}(\bar{s}_L\gamma_\mu b_L)\,(\bar{l}\gamma^\mu l) \tag{1.34}$$

$$Q_{10} = \frac{e^2}{16\pi^2}(\bar{s}_L\gamma_\mu b_L)\,(\bar{l}\gamma^\mu\gamma_5 l) \tag{1.35}$$

$$Q_{\nu\bar{\nu}} = \frac{\alpha_{em}}{4\pi}(\bar{s}_L\gamma_\mu b_L)\,(\bar{\nu}_L\gamma^\mu\nu_L) \tag{1.36}$$

$$Q_{\mu\bar{\mu}} = \frac{\alpha_{em}}{4\pi}(\bar{s}_L\gamma_\mu b_L)\,(\bar{\mu}_L\gamma^\mu\mu_L) \tag{1.37}$$

where, the subscripts L and R refer to the left and right-handed components of the fermion field given by $q_{L,R} = (1 \mp \gamma_5/2)\,q$. e and g represent the electromagnetic and strong coupling constants (g_1 and g_3), e_q is the electric charge of the relevant quark and $T^a_{\alpha\beta} \equiv \lambda^a_{\alpha\beta}$ (a=1,...8) are the $SU(3)$ color generators, α and β being the color indices. The above set of operators is characteristic for any consideration of the interplay of QCD and electroweak effects. Since the ratio α/α_s ($\equiv 10^{-2}$) of the

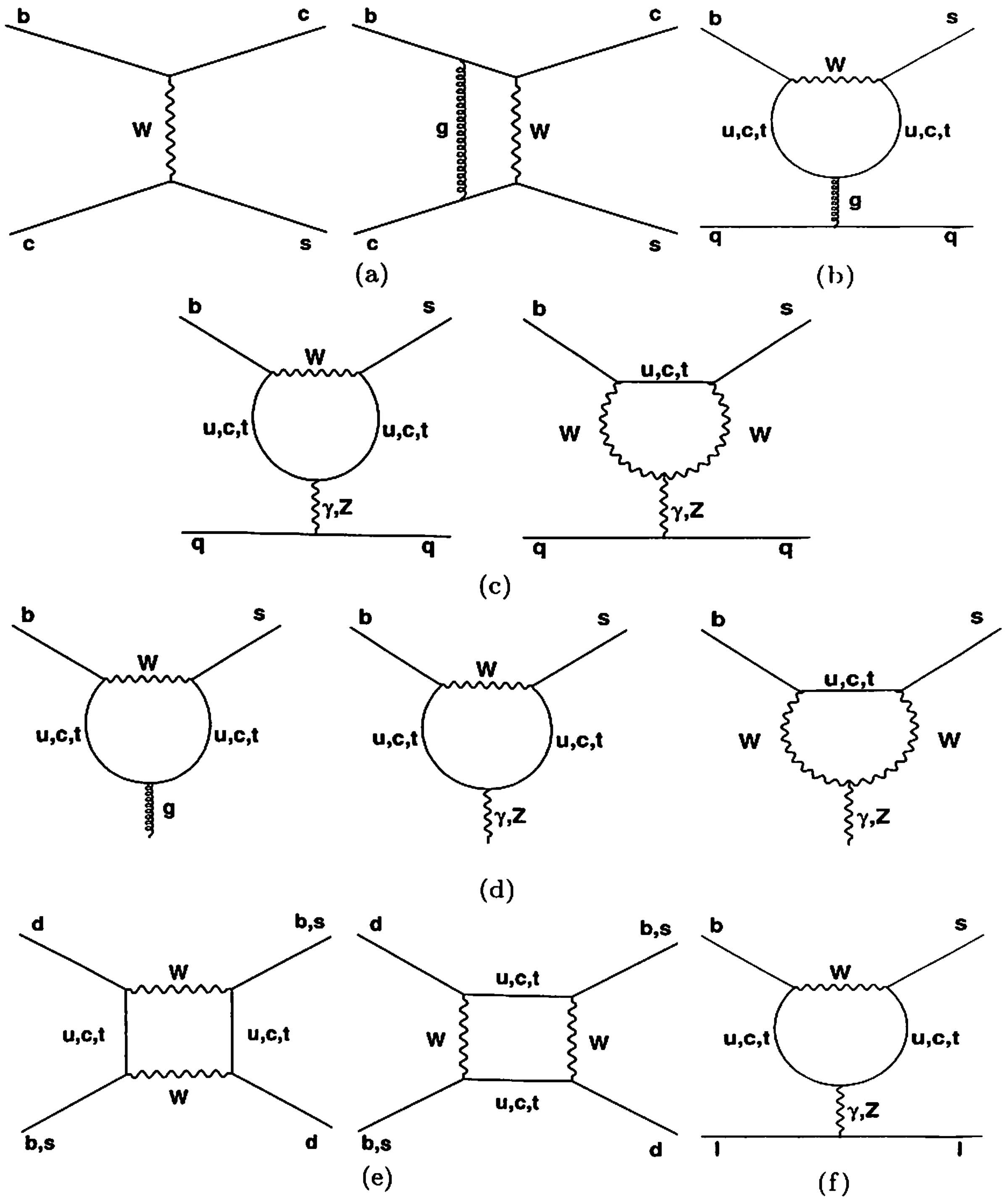

FIGURE 1.2: *Feynman diagram representations of box and penguin processes.*

QED and QCD couplings is very small, electroweak penguins are expected to play a minor role in comparison with QCD penguins.

The effective Hamiltonian arising from this set of operators is usually written as:

$$H_{eff} = \frac{G_F}{\sqrt{2}} \sum_i V^i_{\text{CKM}} C_i(R) Q_i \tag{1.38}$$

where the sum runs over all the operators and V^i_{CKM} is the suitable CKM factor (for e.g., $V^*_{ts}V_{tb}$ for the $b \to s$ transitions). The decay amplitude of a process can be written as:

$$\mathcal{A}(M \to F) = \langle F|H_{eff}|M\rangle = \frac{G_F}{\sqrt{2}} \sum_i V^i_{\text{CKM}} C_i(R) \langle F|Q_i(R)|M\rangle \tag{1.39}$$

where, $\langle F|Q_i(R)|M\rangle$ is the hadronic matrix element of Q_i between M and F evaluated at the renormalization scale R.

The Wilson coefficients can be computed by calculating the amplitude for simple processes in both full and effective theories and then comparing them. Since the Wilson coefficients are process independent, the values obtained by matching a specific process can then be used for the calculation of amplitude of other processes. At higher energies, C_i's can be computed using perturbation theory due to QCD asymptotic freedom. Thus, the Wilson coefficients (C_i's) at an energy R, can be evaluated by first computing them at a high energy scale (M_W), which can then be evolved through renormalization group (RG) [22–24] equations:

$$\mu \frac{d}{d\mu} C_k = \gamma_{ki} C_i \tag{1.40}$$

to low energy scale R. The Wilson coefficients (C_i's) at energy R, can thus be written as:

$$C_k(R) = U_{k,i}(R, M_W) C_i(M_W) \tag{1.41}$$

where,

$$U_{k,i}(R, M_W) = T_g \, exp \left[\int_{g(M_W)}^{g(R)} \frac{\gamma_{ki}(g')}{\beta(g')} \text{d}g' \right] \tag{1.42}$$

is the evolution function which allows to calculate $C(R)$'s once $C(M_W)$'s is known. $C(M_W)$'s are the Wilson coefficients at higher energy scale M_W. T_g is an ordering criterion defined in [22, 25]. $\beta(g) = R(\mathrm{d}g/\mathrm{d}R) \equiv \mathrm{d}g/\mathrm{d}(\ln R)$ is the RG function which governs the evolution of g. γ is the anomalous dimension matrix of the operator involved. Keeping the first two terms in the expansions of $\gamma(g)$ and $\beta(g)$, in powers of g, we get:

$$\gamma(g) = \gamma^{(0)}\frac{\alpha_s}{4\pi} + \gamma^{(1)}\frac{\alpha_s^2}{16\pi^2}, \quad \beta(g) = -\beta_0\frac{g^3}{16\pi^2} - \beta_1\frac{g^5}{(16\pi^2)^2}$$

Inserting these expansions in equation 1.42, we obtain:

$$U(R, M_W) = \left[1 + \frac{\alpha_s(R)}{4\pi}J\right]\left[\frac{\alpha_s(M_W)}{\alpha_s(R)}\right]^P\left[1 - \frac{\alpha_s(M_W)}{4\pi}J\right] \tag{1.43}$$

where,

$$P = \frac{\gamma^{(0)}}{2\beta_0}, \quad J = \frac{P}{\beta_0}\beta_1 - \frac{\gamma^1}{2\beta_0}.$$

The Wilson coefficients will, in general, depend on the masses of the particles, which were integrated out.

The calculation of the operators (and hence the matrix elements) on the other hand require non-perturbative calculations, since they involve long distance contributions. These calculations are mostly done using lattice QCD and some model dependent approaches such as QCD sum rules, hadronic sum rules, $1/N$ expansion (where, N is the number of colors), chiral perturbation theory, large-N_C, etc. All non-perturbative methods have some limitations and hence contribute to large uncertainties in the matrix elements and decay amplitudes. The dominant theoretical uncertainty mostly comes from QCD corrections.

Thus, the decay rate can be written as:

$$\mathcal{A}(M \to F) = \frac{G_F}{\sqrt{2}}\sum_{i,k} V^i_{\mathrm{CKM}} U_{k,i}(R, M_W) C_i(M_W) \langle F|\mathcal{Q}_k(R)|M\rangle \tag{1.44}$$

and its calculation involves three distinct steps:

- Determination of initial conditions of the Wilson coefficients at the electroweak scale.
- Evolution of Wilson coefficients ($\mathcal{C}_i$) by means of RG equations down to $R = \mathcal{O}(m_b)$.
- Evaluation of hadronic matrix elements of the effective operators at $R = \mathcal{O}(m_b)$, including both perturbative and non-perturbative QCD corrections.

New physics effects may induce [6]:

- corrections to the Wilson coefficients.
- new operators not present in the SM.
- new sources of mixing not expected in the SM.

Hence, comparison between the experimental and SM predictions can put constraints on them.

1.4 Two body Charmless hadronic B decays in EFT

The study of hadronic charmless B-meson decays can provide not only an interesting avenue to understand CP violation and the flavor mixing of quark sector in the SM but also a powerful means to probe different new physics scenarios beyond the SM. With the operation of dedicated B-factory experiments, a huge amount of experimental data on hadronic B-meson decays has been analyzed with appreciative precision [26].

To consistently predict hadronic B decays, the theory needs to deal with the short-distance contributions in a complete and systematic way, from the high-energy scale down to a proper low-energy scale at which the perturbative calculations still remain reliable, and to treat the long-distance contributions which contain the non-perturbative strong interactions involved in these decays. The main task is to reliably compute the hadronic matrix elements between the initial and final hadronic states. In recent years, much progress has been made in our understanding of hadronic charmless B-meson decays, and several novel methods based on the factorization approach, such as the perturbative QCD method (PQCD) [27], the QCD factorization approach (QCDF) [28] and the soft-collinear effective theory (SCET) [29], have been proposed.

All the above frameworks of weak decays are based on the four-fermion operator effective Hamiltonian derived via operator product expansion and renormalization theory. In hadronic weak decays, short-distance QCD contributions are characterized by the Wilson coefficient functions of four-quark operators and the long-distance ones are in principle obtained by evaluating the hadronic matrix elements of relevant four-quark operators. The Wilson coefficient functions are in general calculated by perturbative QCD which is well developed, while the evaluation of hadronic matrix elements remains a hard task as it involves non-perturbative effects of QCD.

In the effective Hamiltonian approach, the decay amplitude of a hadronic $B \to h_1 h_2$ decay becomes:

$$\mathcal{A}(B \to h_1 h_2) = \langle h_1 h_2 | H_{eff} | B \rangle \tag{1.45}$$

In the SM, the effective Hamiltonian for $b \to s$ transitions [30, 31], excluding semileptonic and radiative decays, can be written as:

$$H_{eff} = \frac{G_F}{\sqrt{2}} \sum_{q=u,c} V_{qs}^* V_{qb} [C_1(R) Q_1^{(q)}(R) + C_2(R) Q_2^{(q)}(R) + \sum_{i=3}^{10} C_i(R) Q_i(R)] + h.c. \tag{1.46}$$

The effective Hamiltonian for the $b \to d$ transition can be obtained by changing s into d in the above equation.

1.5 The decay $B_s^0 \to \eta\eta$

Charmless hadronic B_s^0 decays constitute an interesting and almost unexplored sector of charmless B decays. In the SM [32], the decay $B_s^0 \to \eta\eta$ can occur through a variety of processes such as CKM suppressed $b \to u$ [33] transition with a further

PQCD	QCDF	SCET
$8.0^{+2.6+4.7+0.0}_{-1.9-2.5-0.0}$	$15.6^{+1.6+9.9+2.2+13.5}_{-1.5-6.8-2.5-5.5}$	$7.1 \pm 6.4 \pm 0.2 \pm 0.8$

TABLE 1.1: *Predictions of the BF for the decay* $B_s^0 \to \eta\eta$ $(\times 10^{-6})$. [2]

color-suppressed with respect to the charged modes [34] or one loop diagrams with a heavy quark and virtual $W^{\pm}$ boson. Contributions can also arise from electroweak penguins. This decay mode can open a window on new physics beyond the SM. In models such as two Higgs doublet model the $W^{\pm}$ boson [35] in the loop can be replaced by a charged Higgs. Minimal Super-symmetric extensions of the SM predict superpartners that could also affect the expected decay rates [36] . Figure 1.3 shows the leading order Feynman diagrams for the decay $B_s^0 \to \eta\eta$.

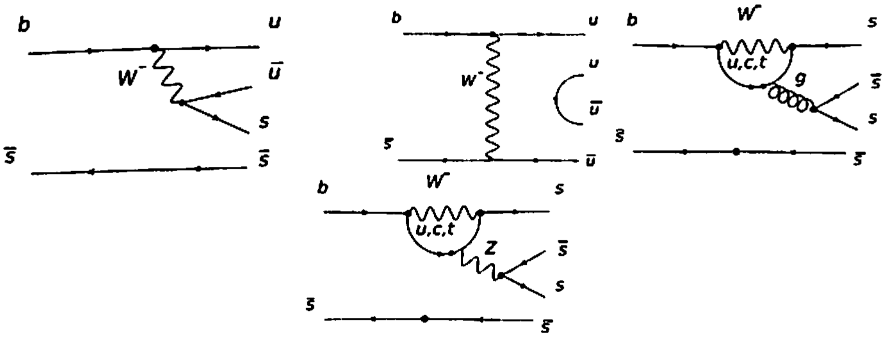

FIGURE 1.3: *Leading order Feynman diagrams for* $B_s^0 \to \eta\eta$. *[1]*

It has been studied theoretically in the framework of SCET, PQCD and QCDF [2]. The predictions of the BF of the decay are given in Table 1.1. The predictions for BF for the $B_s^0 \to \eta\eta$ has large uncertainty, which is mostly due to the QCD uncertainties.

This decay was first searched by the L3 experiment at LEP. In the absence of any significant signal yield, the L3 experiment did put an UL at 1.5×10^{-3} at 90% CL [37] on the branching ratio of $B_s^0 \to \eta\eta$.

1.6 Chapter Summary

In this chapter, we have introduced the SM of particle physics and the associated gauge transformations. The CKM matrix, the GIM mechanism and FCNC processes are then discussed. Renormalization theory, EFT and various analysis techniques are then introduced briefly. A brief summary and discussion on the current experimental and theory status of the decay $B_s^0 \to \eta\eta$ is also presented in this chapter.

Chapter 2

The Belle Experiment at KEKB

The data used to search for the decay $B_s \rightarrow \eta\eta$ at $\Upsilon(5S)$ resonance was collected by the Belle detector, located at the KEKB accelerator, Japan. The Belle experiment is a high energy e^+e^- collider experiment designed and performed by an international collaboration of more than 400 physicists and engineers from over 16 countries around the globe. The primary aim of the Belle experiment was to observe CP violation in the B meson decay [38] by tuning the collision energies at various Υ resonances. Along with CP violation study Belle also provides excellent environment to study rare decays, hadron spectroscopy, tau physics, charm physics, exotic particles and two photon physics. In 2001, Belle discovered CP violation in the B meson system. This result is in agreement with other experiments and provides a confirmation of the Kobayashi-Maskawa mechanism for CP violation in the Standard Model [39]. This chapter describes the KEKB accelerator, the Belle detector, data acquisition system and the trigger system.

2.1 KEKB Acclerator

KEK, the High Energy Accelerator Research Organization, is one of the world's leading accelerator science research laboratories, that produces high-energy particle beams and synchrotron light sources to probe the fundamental properties of matter. The KEKB accelerator and the Belle detector demonstrated the violation of CP asymmetry proposed by Dr. Makoto Kobayashi and Dr. Toshihide Maskawa, who received the 2008 Nobel Prize in Physics. The KEKB collider has been a leader in the race to provide the world's highest luminosity in the e^+e^- collision. The KEKB [40] is an asymmetric energy e^+e^- collider with e^- having energy of 8 GeV and e^+ having energy of 3.5 GeV, located at the KEK laboratory in Tsukuba, Japan. Figure 2.1 shows the schematic view of the KEKB acclerator. The accelerator is composed of two side by side rings in which the beams are sent through a linear accelerator (linac). The setup is put 11 m deep underground and the length of the tunnel is 3 km. In the first stage of the linac, electrons are accelerated to an energy of 4 GeV. Positrons are produced by hitting a thin tungsten mono crystal target with some of these electrons, which radiates photons. These photons create electron-positron pairs and the positrons are collected and accelerated to an energy of 3.5GeV. The electron beam is then accelerated further, and both beams are directly injected into the rings at full energies: the high energy ring (HER) contains electrons at 8 GeV energy and the low energy ring (LER) contains positrons at 3.5 GeV. These beams are made to collide at the interaction point, called Tsukuba, where they cross each other in the center of the Belle detector. The designed luminosity of KEKB was $1.0 \times 10^{3}4cm^{-2}sec^{-1}$.

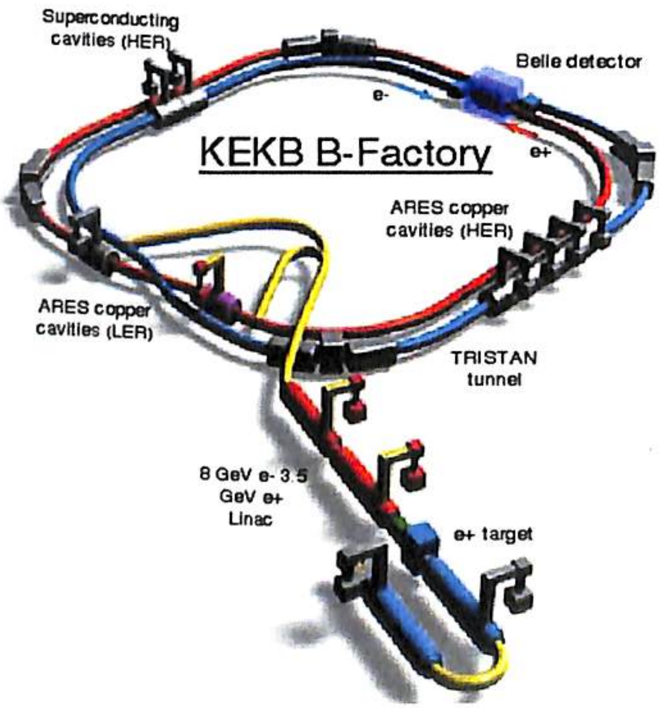

FIGURE 2.1: *Schematic view of the KEKB accelerator.*

The CM energy of the e^+e^- system is given by

$$\sqrt{s} = \sqrt{E_{HER} \times E_{LER}}$$

The energies of the beams are tuned at different Υ resonances. Since the energy of the beams are asymmetric, the resonances are produced with a Lorentz boost along the direction of the electron beam with respect to the laboratory frame. The boost is given by

$$\beta\gamma = \frac{E_{HER} - E_{LER}}{E_{CM}} = 0.425$$

The boost is necessary to observe time dependent CP violation in B meson decay.

Υ resonances are quasi bound states of $b\bar{b}$ with J^{PC} values 1^{--}. The masses of the resonances fall in the range of $(9-11)$ GeV. Figure 2.2 shows the production cross section spectrum as a function of e^+e^- CM energy.

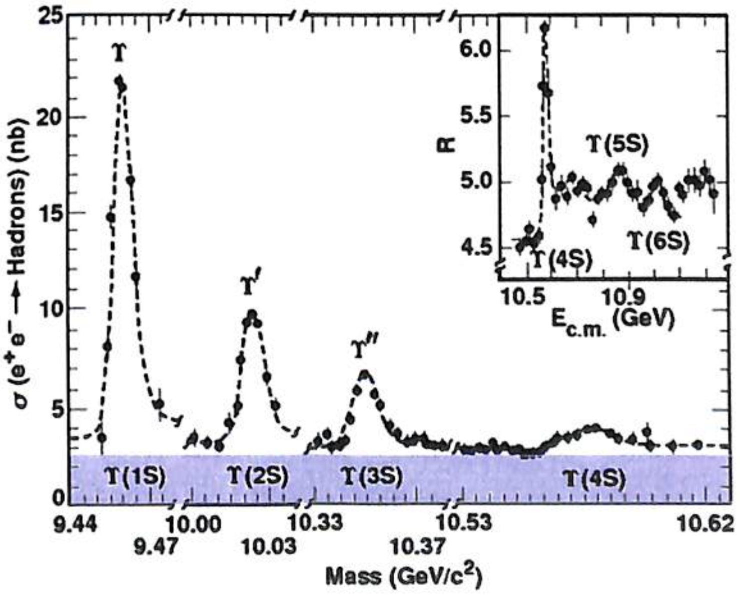

FIGURE 2.2: *The hadronic cross-section for Υ resonances as a function of e^+e^- CM energy.*

Belle detector collected data for 11 years from 1999 to 2010. It had collected more than 1 ab^{-1} of data at different Υ resonances. It had also collected 100 ab^{-1} off resonance data [38]. Table 2.1 shows the collected data sets during the entire duration of the Belle experiment.

Resonance	**Luminosity (fb^{-1})**
$\Upsilon(1S)$	6
$\Upsilon(2S)$	24
$\Upsilon(3S)$	3
$\Upsilon(4S)$	711
$\Upsilon(5S)$	121
Off resonance	100

TABLE 2.1: *Data collected by Belle detector.*

2.2 The Belle Detector

The Belle detector [41] is a general purpose 4π detector [41] which is used to detect and identify the particles produced in e^- and e^+ collision. The detector is located at the interaction point of the e^- and e^+ beam. The Belle detector consists of seven sub-detectors. Each of them collect different information such as energy loss, momentum etc from the particles interaction. These informations are used to identify and detect different particles. The details of each of the sub detectors are discussed below.

The Belle detector is consists of the following seven sub-detectors:

- silicon vertex detector (SVD)
- central drift chamber (CDC)
- aerogel Cherenkov counter (ACC)
- time of flight counter (TOF)
- electromagnetic calorimeter (ECL)
- K_L^0 and muon detector (KLM)
- extreme forward calorimeter (EFC)

Figure 2.3 shows the schematic view of the Belle detector. In the following subsections, the details of the beam pipes, the coordinate system of the detector and each of the seven sub-detectors are explained.

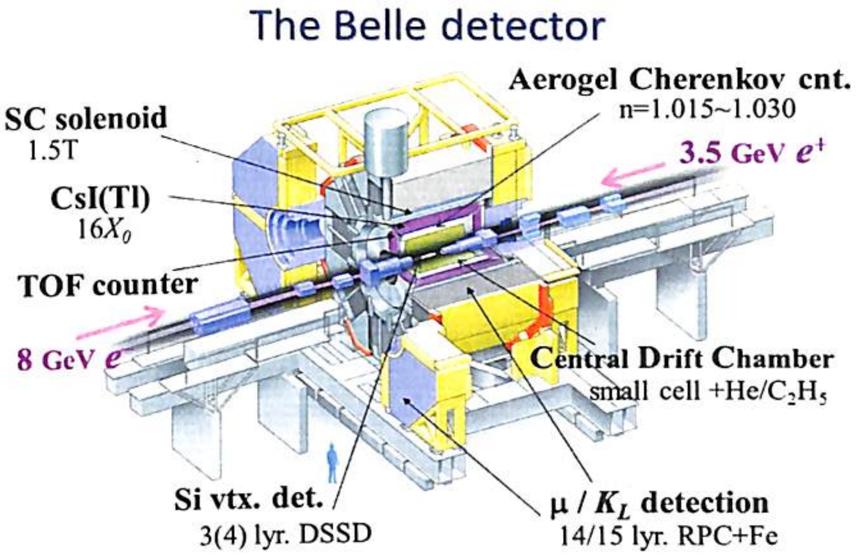

FIGURE 2.3: *Belle detector.*

2.2.1 Beam pipes and the interaction point (IP)

There are two beam pipes in the KEKB, the electron beam and the positron beam. The electron beam has energy of 8.5 GeV and the circulating ring is called high energy ring (HER). The positron beam has energy of 3 GeV and the circulating ring is called low energy ring (LER). Both the beams are made to collide at the interaction point (IP) where the Belle detector is sited. The pipes are cylindrical and made of double walls of beryllium. The walls have radii of 20 mm and 23 mm which is shown in Figure 2.4. Beryllium has low atomic number which reduces Coulomb scattering, which is the main limiting factor on the z vertex position resolution. A 2.5 mm gap separates the two walls. This gap is filled with Helium gas which absorbs the heat. The nearest sub-detector is the Silicon Vertex Detector (SVD) that measures the decay vertices. Cooling is necessary to improve the the vertex resolution. Helium gas is circulated between the walls to dissipate the heat. The beam pipes are wrapped by 20 μm thick gold foil to shield the low energy X ray background.

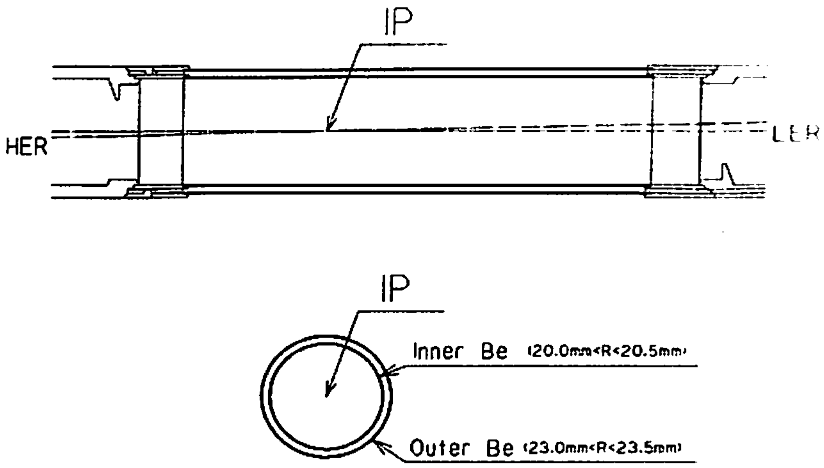

FIGURE 2.4: *Schematic view of beam pipe.*

2.2.2 Coordinate System of the Belle detector

The coordinate system that is used to describe the Belle detector is the following: the IP acts as the origin of the system; the direction of the electron beam is used as the positive z axis of the system; the x and y axis are horizontal and vertical to the z axis. The radial distance, r is defined as $r = \sqrt{x^2 + y^2}$ and the polar angle, θ and azimuthal angle, ϕ are defined with respect to the z and x axis, respectively. The Belle detector is asymmetric along the z axis and can be divided into three regions based on the polar angle coverage: barrel region, forward end cap and the backward end cap region as mentioned in Table 2.2.

Region	Polar angle coverage
Barrel	$34^\circ < \theta < 127^\circ$
Forward endcap	$17^\circ < \theta < 34^\circ$
Backward region	$150^\circ < \theta < 127^\circ$

TABLE 2.2: *Sub regions of the Belle detector.*

2.2.3 Silicon Vertex Detector(SVD)

SVD is used for the precise measurement of the decay vertices of B meson, D meson and τ particles produced in e^+e^- collisions. Precise vertex measurement is essential for time dependent CP violation study. It is the closest Belle sub-detector to the beam pipe. The vertex measurement precision of the SVD is 100 μm, which is

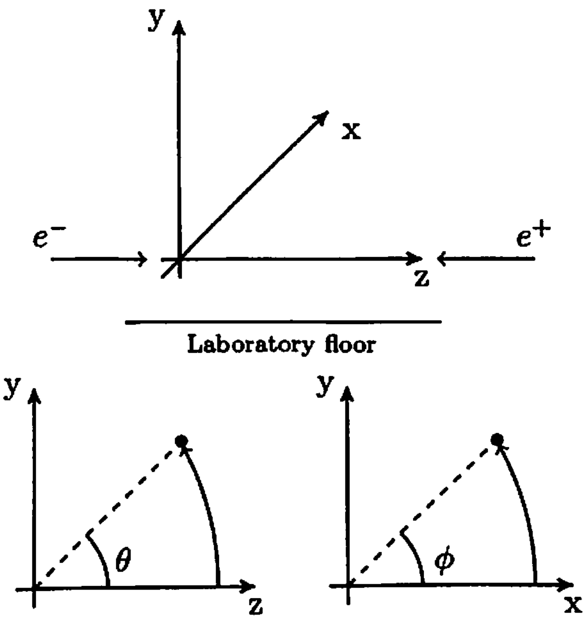

FIGURE 2.5: *Belle coordinate system.*

required for CP violation study in B meson decays. In addition to vertex measurement, it also plays important role in charged particle tracking, particularly for low momentum charged particles.

SVD is cylindrical about the z axis. The SVD that is used during the period 1999 to 2003 consists of three layers of double sided silicon strip detectors (DSSD) and called as SVD1. The polar angle coverage of SVD1 is $23° < \theta < 139°$. Figure 2.6 shows the configuration of SVD1. SVD1 was replaced by the upgraded version in 2003, called SVD2 [42], which consists of four layers equipped with DSSD. Figure 2.12 shows the configuration of SVD2. The polar angle coverage of SVD2 is $17° < \theta < 150°$. SVD2 improved the z vertex resolution of the decays with low momentum tracks by an amount of 20% with respect to the SVD1. DSSDs are made of depleted $p - n$ junctions. Charged particles passing through the junctions create electron-hole pairs along their trajectory which drift to the n^+ and p^+ strips of the DSSD. The n^+ and p^+ strips are placed perpendicular and parallel to the beam direction, respectively. Since n^+ strips are perpendicular to the beam axis, they measure the z coordinate whereas the p^+ strips which are parallel to the beam axis measure the azimuthal angle, ϕ. Each side of DSSD consists of 1280 sense strips and 640 read out pads.

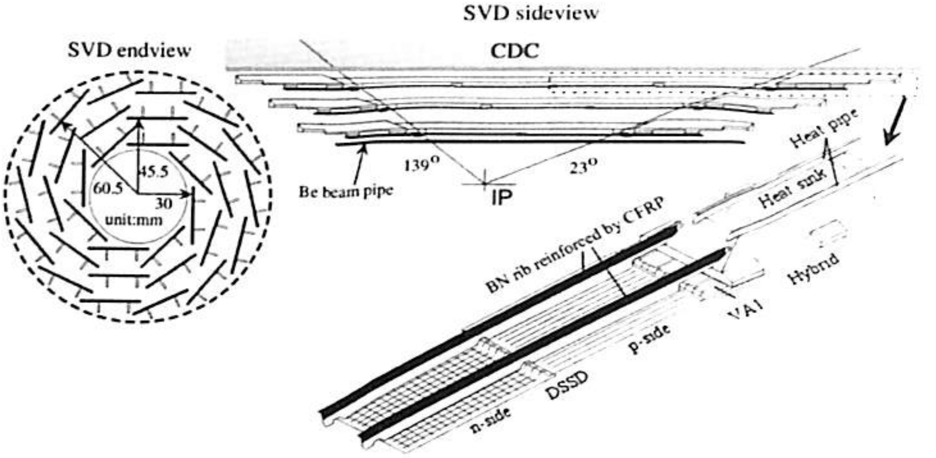

FIGURE 2.6: *Schematic view of SVD1.*

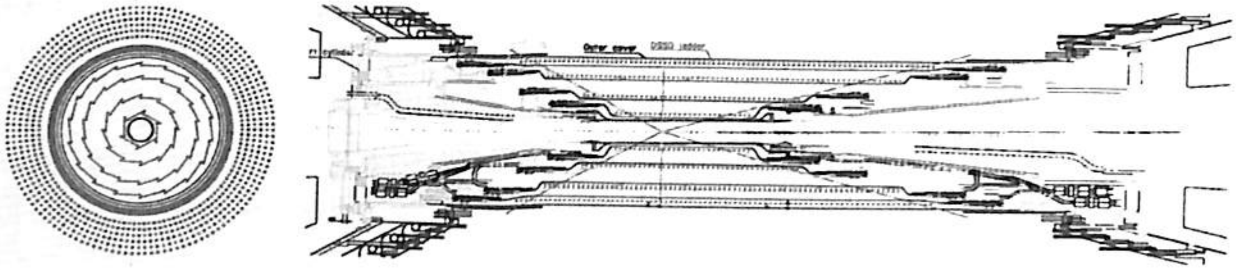

FIGURE 2.7: *Schematic view of SVD2.*

2.2.4 Central Drift Chamber(CDC)

The CDC is the second Belle sub-detector after SVD, which is a tracking detector. The purposes of CDC are the reconstruction of charged tracks and precise measurement of momentum and position of charged particles. It also distinguishes charged particles via the measurement of $\frac{dE}{dx}$. It is cylindrical about the z axis and asymmetric along the z direction. The length of CDC is 2400 mm and inner and outer radius are 83 mm and 880 mm, respectively. It covers a angular region of $17° < \theta < 150°$. Figure 2.8 shows the overview of CDC. The CDC drift chamber has 50 layers (32 axial layers and 18 small angle stereo layers) of anode wires and three cathode strip wires. The axial wires are placed parallel to the z axis while the stereo wires are slanted approximately ±50 mrd. To reduce multiple Coulomb scattering, the chamber is filled with low Z gas, mixture of 50% He and 50% C_2H_6. CDC has 5280 axial drift cells and 3120 stereo drift cells. The cathode strips are divided into eight segments in ϕ direction and 64 segments in z direction to provide

z coordinate information.

The Belle detector is placed in a 1.5T magnetic field. Due to the magnetic field charged particles follow path of different curvature according to their momenta. Another purpose of CDC is to distinguish particles by measuring $\frac{dE}{dx}$. Figure 2.9 shows the expected $\frac{dE}{dx}$ of different charged particles as a function of their momentum. CDC is described in more details in [43].

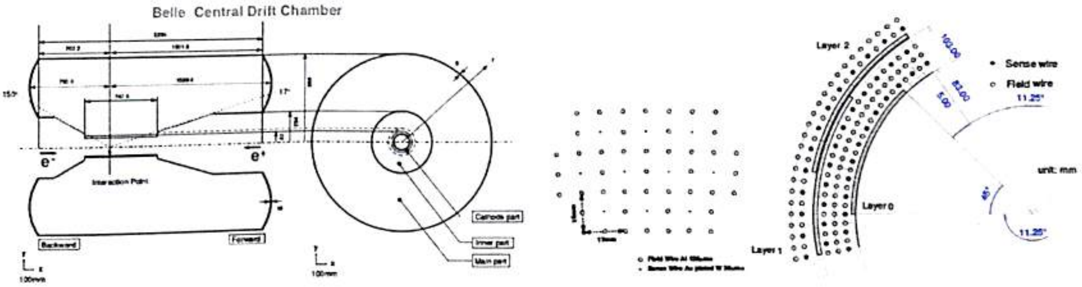

FIGURE 2.8: *Configuration of CDC.*

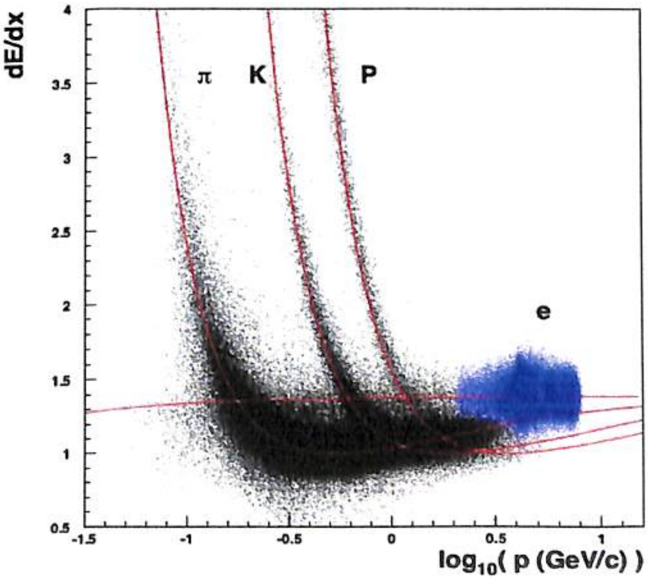

FIGURE 2.9: $\frac{dE}{dx}$ *as a function of momentum.*

2.2.5 Aerogel Cherenkov Counter(ACC)

The sub-detector next to CDC is ACC. ACC distinguishes particles of similar momenta which have different masses and hence different velocities. It distinguishes pions and kaons produced in B meson decays in the momentum range of $1.2 < p < 3.5 GeV/c$. It works on the principle of Cherenkov light emission by charged particle. A charged particle emits Cherenkov light when the velocity of the particle, β satisfies the relation

$$\beta = \frac{p}{\sqrt{p^2+m^2}} > \frac{1}{n}$$

where p and m are the momentum and mass of the particle and n is the refractive index of the medium. For a medium with fixed n there is momentum range where kaons emit Cherenkov light while pions do not.

The ACC is composed of 960 counter modules segmented into 60 cells in the ϕ direction in the barrel part and 228 modules arranged in 5 concentric layers for the forward endcap part of the detector. Figure 2.10 shows the configuration of the ACC. The total polar angle coverage range of ACC is $17° < \theta < 127°$. A typical ACC module has five tiles of silica aerogel stacked in a thin aluminum box of size 12 cm×12 cm×12 cm. To get good k to π separation in the momentum range $(1.24 < p < 3.5)$ GeV, the refractive index of the aerogel in the barrel region were chosen based on the polar angles and ranges between 1.010 to 1.028. The end cap aerogels have refractive index of 1.030. Figure 2.11 shows the ACC module. ACC correctly separates pions and kaons between 80% to 95% of the time. The ACC is described in more details in [44].

2.2.6 Time of Flight(TOF) counter

TOF sub detector system provides the time that a particle needs to travel from the interaction point to the TOF module. It is sited just outside the ACC. The TOF system is sensitive to momenta $p < 1.2$ GeV and complementary to the ACC as it provides information in distinguishing charged kaons and pions. TOF system has an angular coverage of $33° < \theta < 121°$. It has 128 TOF counters and 64 trigger

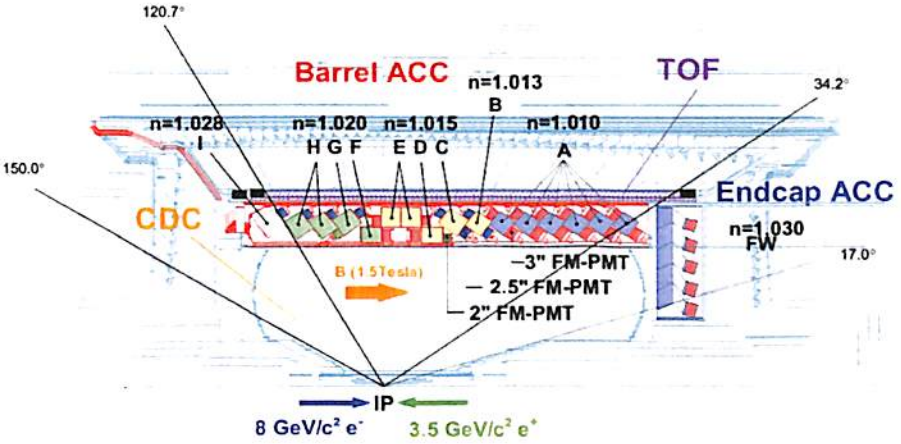

FIGURE 2.10: *Schematic diagram of ACC.*

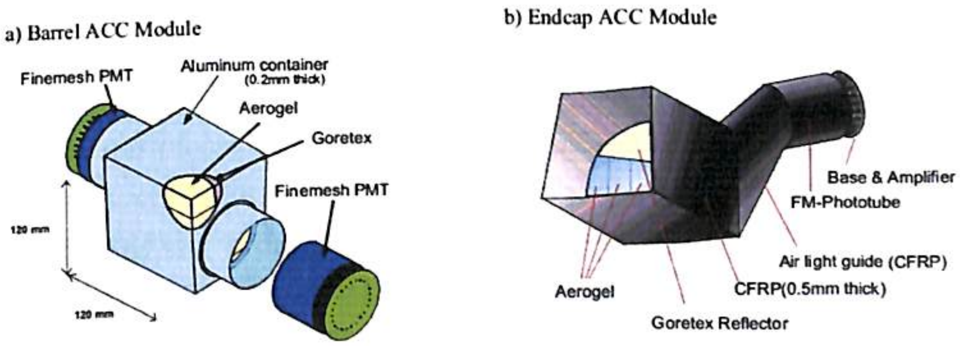

(a) (b)

FIGURE 2.11: *ACC module.*

scintillation counters. The counters measure the elapsed time between a collision at the interaction point and the time when the particle hits the counters. The measured time information (T), in addition with the momentum information (p) given by ACC, allows to compute the particle mass (m) and hence the particle identity. The mass of the particle is given by

$$m = \frac{p}{c}\sqrt{(\frac{cT}{L})^2 - 1}$$

where L is the distance traveled by the particle from the IP to the TOF module. The lay out of TOF counter is shown in Figure 2.12. TOF system is described in more details in [45].

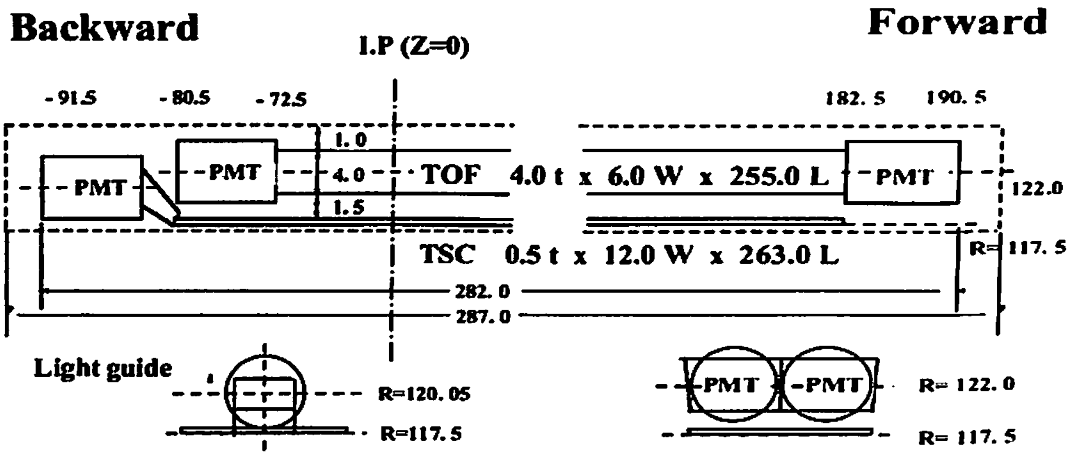

FIGURE 2.12: *Lay out of TOF module.*

2.2.7 Electromagnetic Calorimeter(ECL)

ECL sits next to the TOF counter. The purpose of the ECL is to detect electrons and photons coming from B meson decays with a good resolution in energy and position. It measures the shower energies produced by the electrons and the photons. It consists of thallium doped CsI crystal counters. It has three sections: the forward end cap section, the barell section and the backward end cap section. The forward end cap section covers $12.4° < \theta < 31.4°$ and consists of 1152 crystals. The barrel section covers $32.2° < \theta < 128.7°$ and consists of 6624 crystals. The backward endcap section covers $130.7° < \theta < 155.1°$ and consists of 960 crystals. Figure 2.13 shows the overview of the ECL. The scintillating material should have large photon yield, crystal transparency to its radiation, short decay constant and high mechanical stability. The barrel section is 3 m long and has 1.05 m and 1.64 m inner and outer radius, respectively. The length of the each crystals is 30 cm which is equivalent to 16.2 radiation length. The shape of the crystals are like tower with front face of (55 mm × 55 mm) and a rear face of (65 mm×65mm). The size of the crystal is optimized on the basis of position and energy resolution.

When high energy photons and electrons interact with the crystals, electromagnetic showers are generated through subsequent bremsstrahlung and electron-positron pair production processes followed by Coulomb scattering. The overall energy and position resolution of ECL as a function of energy E can be expressed as

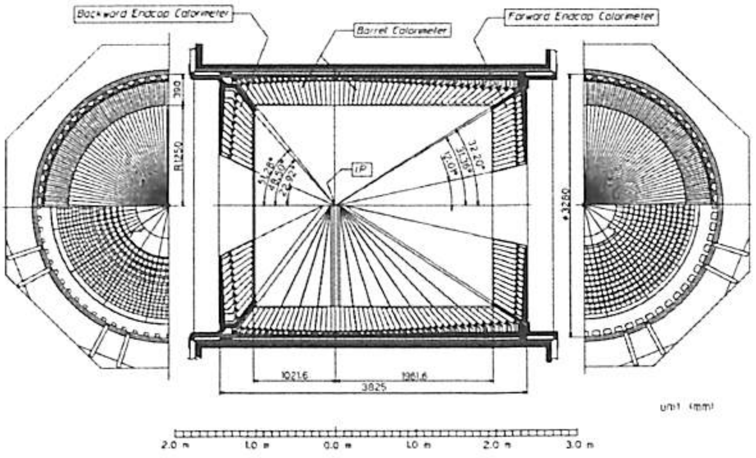

FIGURE 2.13: *Schematic diagram of ECL.*

$$\frac{\sigma_E}{E}(\%) = \frac{0.0066}{E} + \frac{1.53}{E^{1/4}} + 1.18$$

$$\sigma_{position} = 0.27 + \frac{3.4}{E^{1/2}} + \frac{1.8}{E^{1/4}}$$

where E is in GeV. In the expression, the first term is the contribution of electronic noise and the second and a part of the third term comes from the shower leakage fluctuations. The third term also includes systematic effects such as the uncertainty on the calibration of the light yield in the crystals. The ECL is described in more details in [46].

2.2.8 Extreme Forward Calorimeter

The Extreme Forward Calorimeter (EFC) is used to detect and measure the electromagnetic showers produced in the extreme forward and backward directions. The polar angle coverage of EFC, $17^\circ < \theta < 150^\circ$ is extended in the forward and backward regions. It covers angular range from $6.4^\circ < \theta < 11.5^\circ$ in the forward region and $163.3^\circ < \theta < 171.2^\circ$ in the backward region. Figure 2.14 shows the schematic view of the EFC. The region around the beam pipe near the interaction point has very high radiation level. So the EFC which is placed near the interaction point should have the property of radiation hardness. $Bi_4Ge_3O_12(BGO)$ crystal has the required property and used in the EFC. EFC works as a beam mask and reduces back grounds for CDC. It also acts as a beam monitor for the Belle experiment. EFC improves the sensitivity of the processes such as $B^+ \to \tau^+$ and provides tagging information for $\gamma\gamma$ physics. It has excellent e and γ energy resolution of $\frac{(0.3-1.0)}{\sqrt{E}}\%GeV$. The EFC is described in more details in [47].

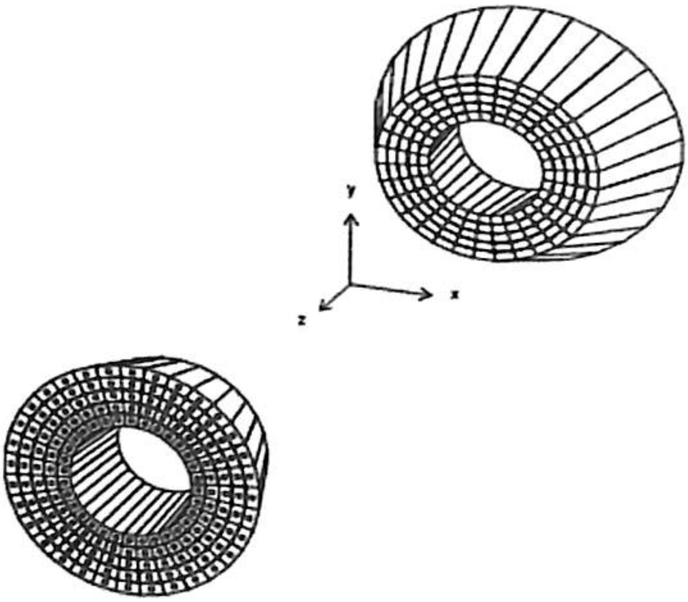

FIGURE 2.14: *Scheamatic view of EFC.*

2.2.9 K_L^0 and Muon detector(KLM)

KLM is the outermost sub-detector of the Belle detector. It sits after the ECL. KLM sub-detector is used to identify K_L^0s and muons in a wide momentum range with high efficiency. Particles which reach the KLM have transverse momentum $(p_T) > 0.6GeV$. The life time of K_L^0 and muons are comparetively large and losses very small amount of energy in the previous sub-detectors. KLM consists of alternate layers of glass resistive plate counters (RPC) [48]) and iron plates. Figure 2.15 shows the schematic diagram of KLM. KLM has 15 RPC layers and 14 iron layers. KLM covers an angular range from 20° to 155°. The ECL provides only 0.8 interaction lengths for K_L^0 mesons, the 14 layers of iron plates add 3.9 interaction lenghts. The iron plates shield most of the charged particles other than muons. Due to small interaction cross section muons travel further without much transverse scattering in the KLM which makes muon identification purest with efficiency above 90% and less than 5% mis-identification.

RPCs are made of parallel glass electrodes of a high bulk resistivity ($> 10 \times 10^{10} ohm - cm$). The gap between the electrodes are filled with gas. The gas is ionized when charged particles pass through it, which causes a discharge at the electrodes which are picked up by the readout strips to measure its location. Figure 2.15 shows the schematic diagram of KLM and RPC module. The KLM detector is described in more details in [49].

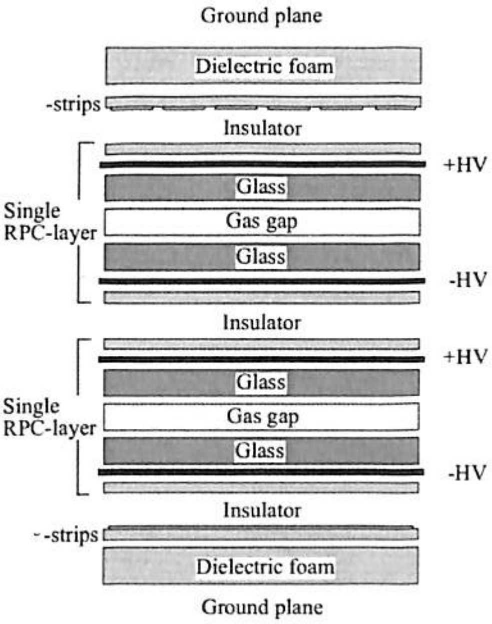

FIGURE 2.15: *Lay out of RPC.*

2.3 The Trigger System

The purpose of the trigger in the Belle detector is to record the useful events of physics interests and rejects the others produced during e^+e^- collisions. The trigger plays an important role in the experiment. Useful events contain mainly the hadronic events involving B mesons. During e^+e^- collisions, a significant number of events are produced which are not of interest for physics analysis in the Belle Experiment. For example, interactions between the particle beams and the residual gas, e^+e^- scattering, interactions with the material of the beam pipes, synchrotron radiation, cosmic ray events etc. The trigger system rejects the uninteresting events and selects the interesting ones. The Belle trigger system is described in more details in [50, 51]. The selected events are then forwarded to the data acquisition system (DAQ) with high efficiency within a very short decision time.

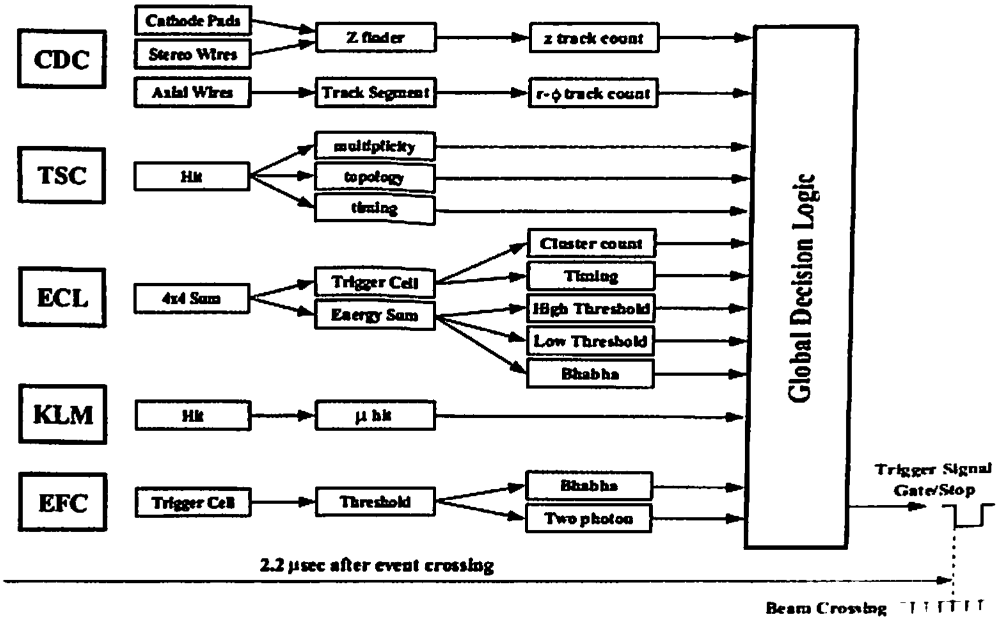

FIGURE 2.16: *Overview of L-1 trigger.*

2.3.1 Lvel-1 Trigger

The Belle Level-1 (L1) trigger system consists of sub-trigger systems and the central trigger system called the Global Decision Logic(GDL). Figure 2.16 shows the overview of the L-1 hardware trigger system. The sub-triggers are categorized into two types: track triggers and energy triggers. The track triggers use charged particles track information for triggering. CDC and TOF provide trigger signals from charged particles. CDC provides $r-\phi$ and z trigger. $r-\phi$ trigger is used to identify the tracks originating from the IP. It uses track direction, transverse momentum and number of track information for triggering. z trigger uses z position information to reject tracks from beam background due to high beam currents. Such tracks come from beam-gas events, from interactions of material around the beam pipe or from cosmic rays. TOF trigger system provides timing signals with a time jitter less than $10ns$ and information on event multiplicity and topology. On the other hand the energy triggers use total energy deposition and cluster counting of crystals hits of ECL for trigger. KLM and EFC trigger systems provide additional trigger information. KLM trigger is based on the number of muon hits. EFC triggers are used for tagging two-photon events and Bhabha events. Sub-triggers parallely process event signals and provide trigger information to the GDL. GDL combines all the information and distinguishes the signal and background events. The L1 trigger system is described in more details in [50].

2.3.2 Level-3 Trigger

The Level-3(L3) trigger is a software trigger which reduces the event rate by about 50%. L3 implements a fast track-finding algorithm. It selects events with at least one track with z impact parameter less than 5 cm and at least 3 GeV energy deposition in ECL. It selects 99% of interesting physics events and rejects 50% − 60% of L1 events.

2.4 Data Acquisition(DAQ)

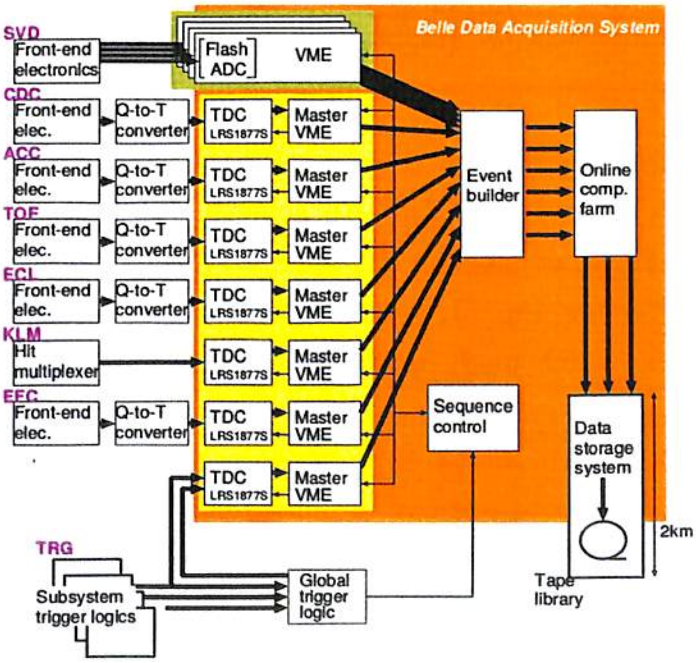

FIGURE 2.17: *Schematic view of the DAQ*

The Data Acquisition system (DAQ) collects signal information from the various sub-detectors, converts them to event by event data and store in the storage system. Figure 2.17 shows the schematic view of the DAQ. The DAQ system has seven sub-systems. The sub-systems work in parallel, each handling data from a sub-detector. The parallel system increases the overall data acquisition rate and fulfill the requirements so that it works at a speed of required 500 Hz with a dead time fraction of less than 10%. The data collected from the systems are converted to event by event data by an event builder. The output of the event builder is sent to an on line computer farm, where another level of event filtering is done after the fast event reconstruction. The data to be recorded are then sent to a mass storage system located at the computer center via optical fibers at the rate of about 15 MB/sec.

2.5 Hybrid Avalanche Photo-Detector (HAPD)

For the Belle II experiment, there is a considerable upgradation of the Belle detector including the proximity focusing Cherenkov detector that usage aerogel as a radiator. A 144 channel HAPD (Hybrid Avalanche Photo-Detector) is one of the candidate photo-detectors. As part of my hardware contribution to the Belle II experiment, I worked on testing the performance of the HAPD in a 1.5 Tesla magnetic field.

Belle II experiment has the aim to search for the so called new physics in measurements of rare B, D and τ decays. To achieve this Belle II collaboration has upgraded the KEK B collider, which will have very high luminosity to provide the needed statistics. The new Belle II spectrometer will log all interesting events and for that it should have extremely accurate vertex and tracking system, particle identification system and energy measuring system.

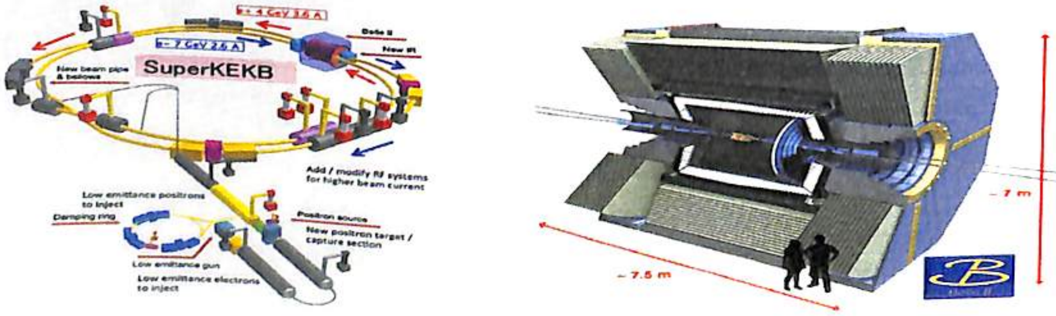

FIGURE 2.18: *Schematic view of SuperKEKB collider (left) and Belle II spectrometer (right)*

2.6 Particle Identification (PID)

Particle identification is the process by which particles are identified on the basis of the information that is left by them on the detector when they pass through it. It is one of the fundamental requirements of all experiments in high energy physics. This section will cover the basics of PID via Cherenkov radiation.

2.6.1 Cherenkov radiation

When a charged particle moves in a medium with speed greater than that of light - in that medium - Cherenkov radiation (polarized electromagnetic radiation) at a characteristics angle is emitted. Relation between that angle and a speed of particle is given as $cos\theta = 1/\beta n$, where θ is Cherenkov angle, β is speed of particle divided by speed of light and n is the refractive index of the medium.

Molecules in close proximity of particle trajectory are momentarily polarized, and after its passes those molecules return to their initial state by emitting photons, which can interfere destructively or constructively, depending on the particle speed. Constructive interference of photons caused by particles traversing the matter faster than speed of light, is called Cherenkov radiation. Graphical representation is shown in Figure 2.19.

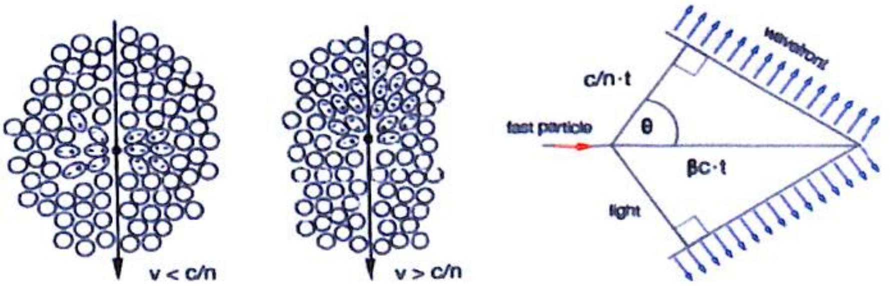

FIGURE 2.19: *Polarization of matter by charged particle traversing the matter. Left: particles slower than electromagnetic waves induce symmetrically arranged dipoles around their path - no net dipole moment and no Cherenkov radiation. Center and right: particles faster than light break symmetry causing non-vanishing dipole moment - radiation of Cherenkov photons at a characteristic angle θ.*

2.6.2 PID

Cherenkov angle depends on the momentum of the particle. Figure 2.20 shows that Cherenkov angles for kaons and pions are well separated in a range of energies up to 4 GeV/c in the same medium.

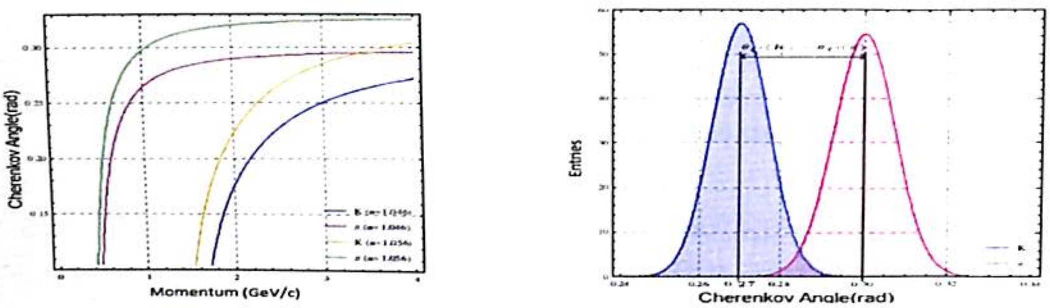

FIGURE 2.20: *Cherenkov angle as a function of particle momentum for kaons and pions in medium with* $n = 1.046$ *and* $n = 1.056$.

2.7 Proximity-focusing Aerogel Ring Imaging Cherenkov detector

PID system specifically designed for Belle II has to comply with physical and detector requirements. Physical requirements are:

- separation between kaons and pions up to 4 GeV/c
- discrimination between pions, muons and electrons below 1 GeV/c

And the detector requirements are:

- immunity to 1.5 T magnetic field
- high tolerance for neutron and gamma radiation
- system has to fit in a 28 cm wide space.

Type of system that fulfills all of the above criteria is called proximity-focusing Ring Imaging Cherenkov (RICH) detector with aerogel as a radiator (ARICH). Schematics are shown in Figure 2.21.

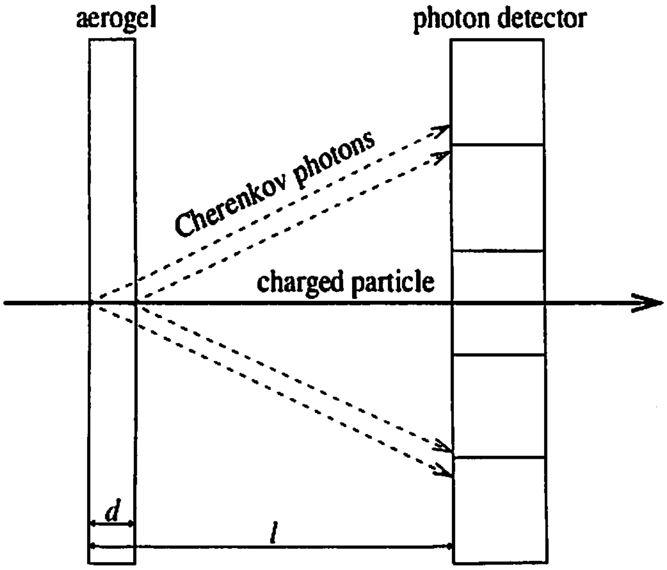

FIGURE 2.21: *Schematics of proximity-focusing ARICH detector.*

2.8 Photon Detector

At first, there were three proposed photon detectors for proximity-focusing RICH detector. These are Silicon Photo-Multipliers (SiPM) with light guides, Micro Channel Plate Photo Multiplier Tubes (MCPPMT) and Hybrid Avalanche Photo-detector (HAPD). But SiPM is found to be affected by neutron radiation and photo-cathode of MCP PMT does not have the capacity to deal successfully with aging (long exposures to photons). So, HAPD manufactured by Hamamatsu Photonics was chosen for proximity-focusing RICH photon detector.

2.8.1 Hybrid avalanche photo diode

Photodiode consists of p-n junction and it is a very simple semiconductor photon detector. At the junction of the p-n diode diffusion of charge carrier takes place and creates a depleted region with weak electric field. When a particle like electron passes through the depleted region (or near the edge) it generates electron-hole pair in that region and the electric field of that region pushes electrons to the n-doped layer, and holes to the p-doped layer. The movement of the charge generates a electric current but it is too small to be measured. The lack of internal amplification (gain) makes photo diode applicable only when one expects more than 1000 photons, each producing an electron-hole pair.

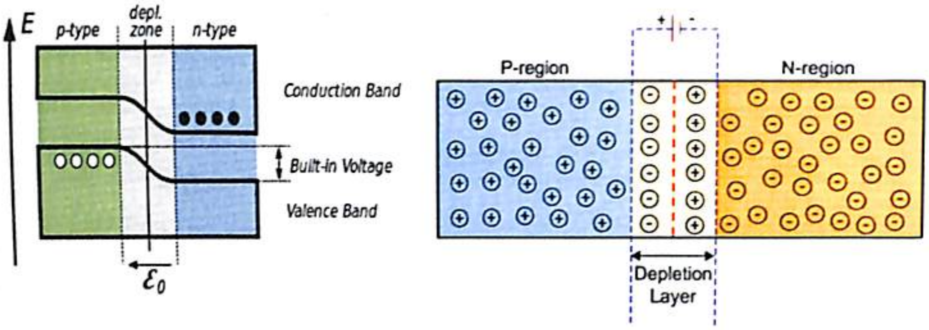

FIGURE 2.22: *Silicon photodiode.*

In our case the photon intensity is small, so to measure this kind of small signal one can use reverse bias on photo diode. The reverse bias increase the internal electric field which helps the electrons to receive enough kinetic energy for further ionization. Photo diode with reverse bias is called an avalanche photo diode (APD). Internal gain is limited by the breakdown voltage, which is defined as the voltage at which multiplication by holes becomes considerable, and the multiplication is no longer controlled, up to around factor 1000. This is still not enough for single photon detection.

To achieve higher gain one can combine vacuum technology with semi conducting photo detectors. Here the dynode and the anode structure of classical photomultiplier tubes are replaced by high electric field and avalanche photo diode, respectively and we get HybridAPD. When a photon hits the photo diode it generates photo electron via photoelectric effect. Electron is then accelerated by high electric field, so when it hits avalanche photodiode at the bottom of HybridAPD, it has enough energy to generates several 1000 primary pairs via ionization. Average number of generated pairs defines the so called bombardment gain. Next step in multiplication is the same as with APD. So the total gain of HybridAPD is convolution of bombardment gain and avalanche gain, which is enough for single photon detection capabilities.

2.8.2 Hamamatsu Hybrid Avalanche PhotoDetector (HAPD)

Hamamatsu HAPD that has become a part of proximity-focusing RICH detector with aerogel radiator, is a square shaped HybridAPD. It consists of super bialkali photo cathode, vacuum region with high electric field (typical bias is around 7 kV), and four APD chips, that are further pixelated in 6 × 6 pixels. Flawless production of big APD chips is very difficult and expensive. Therefore, it is easier and cheaper to make HAPD from four smaller APD chips, than form one 12 × 12 pixels big APD. Major specifications are mentioned in Table 2.3

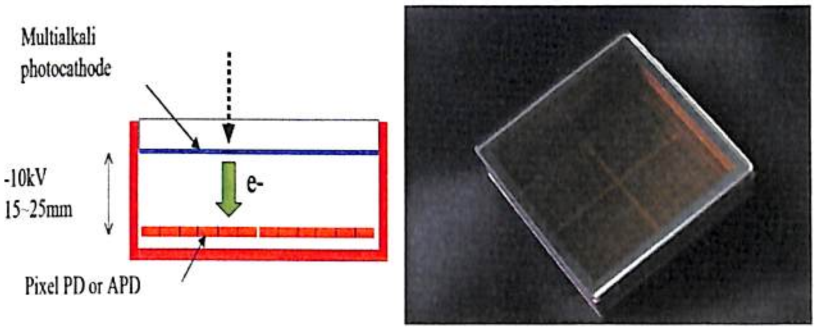

FIGURE 2.23: *Schematic view (left) and picture (right) of HAPD.*

package size (mm^2)	$73X73$
sensitive area (%)	64
number of pixels	144 (36X4 chips)
pixel size (mm^2)	$4.9X4.9$
capacitance (pF)	80
single photon detection efficiency	0.80
weight (g)	220
peak quantum efficiency (%)	30
bombardment gain	1500
avalanche gain	30
total gain	$45X10^3$

TABLE 2.3: *HAPD specifications.*

2.9 Properties of HAPD

2.9.1 Gain

Mean energy required to produce an electron-hole pair in silicon is approximately $W = 3.66$ eV. Theoretically, primary photo electron with energy E could ionize E/W secondary electron-hole pairs. From this, we can get linear connection between bombardment gain and photo cathode voltage. Exponential growth of an avalanche of secondary electron-hole pairs is a bit harder to get, but electrons that gain at least 3.66 eV of energy on their mean free path can generate another pair and so on. Therefore, avalanche gain has exponential dependence on reverse voltage.

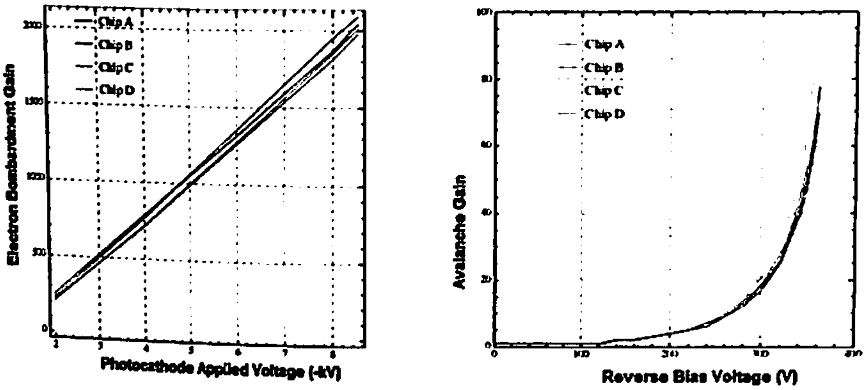

FIGURE 2.24: *Linear dependence of bombardment gain on photocathode voltage for typical HAPD (left). And exponential dependence of avalanche gain on reverse bias voltage for typical HAPD (right).*

2.9.2 Pulse height spectrum

Response of HAPD to short light pulses with wavelength of 470 nm can be seen from Figure 2.25. Excellent photon counting ability is evident as peaks corresponding to different number of detected photons are finely separated.

2.9.3 Background contribution

From the position of incident Cherenkov light on photon detector we can determine cherenkov angle and fill histogram it. On the right side of Figure 2.26, we see that we do not get only one Gaussian peak per incident charged particle of

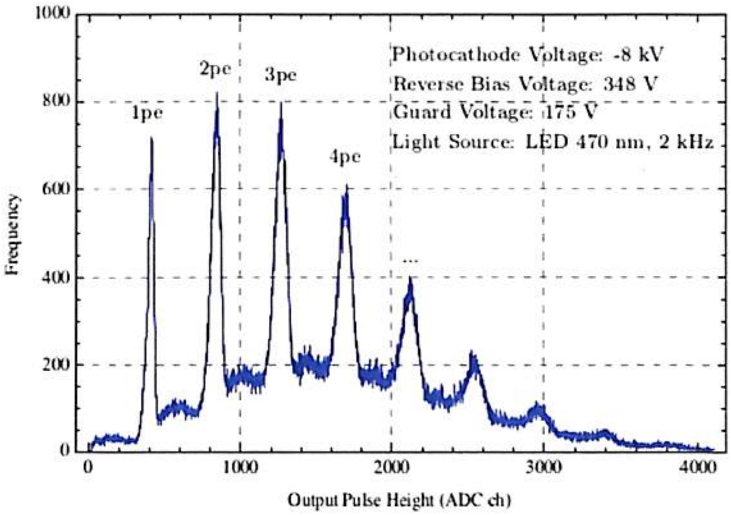

FIGURE 2.25: *Pulse height spectrum where peaks corresponds to different number of detected photons.*

selected momentum, but also additional background. Background can be explained by Cherenkov light that is reflected from APD surface and then produces photo electron, by photo electron back scattering, Cherenkov light from window, and internally reflected Cherenkov light.

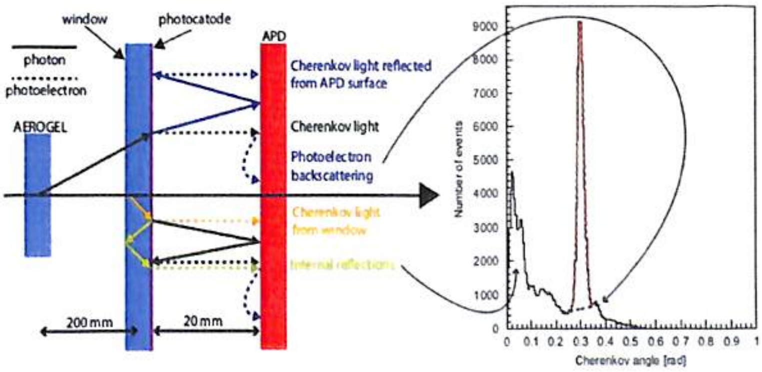

FIGURE 2.26: *Sources of additional background peaks.*

2.9.4 Quantum Efficiency (QE)

Quantum efficiency is the number of photoelectrons emitted from the photocathode divided by the number of incident photons. Therefore, photocathodes with higher QE will emit more photons and as a result, achieve better Cherekov angle resolution. QE peak of 30% at 360 nm has been achieved for typical HAPD with

"Super Bialkali" photocathode - it is important to note. that QE peak coincides with wavelengths of Cherenkov radiation. In comparison. photocathodes of classical photomultiplier have highest QE with "Ultra Biakali" photocathodes up to 43%

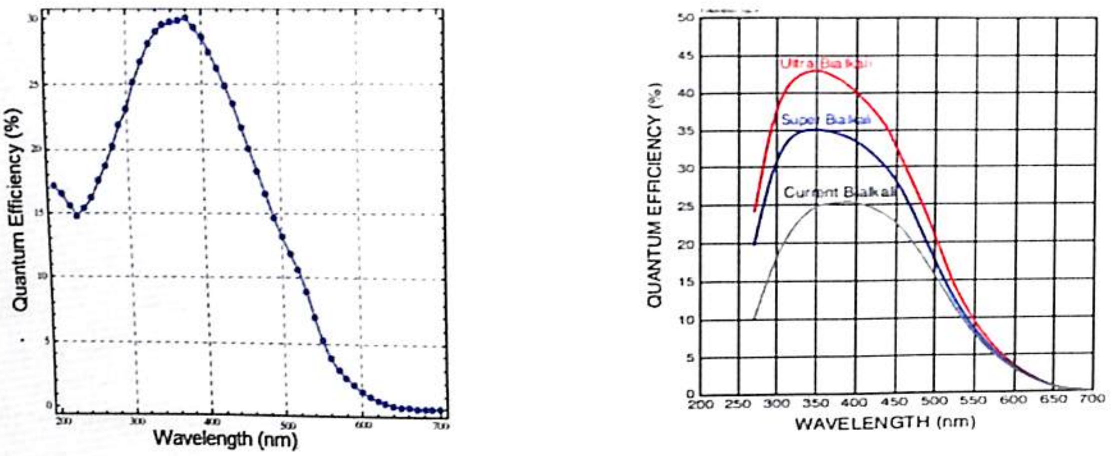

FIGURE 2.27: *QE for typical HAPD (left). QE of photocathodes from classical photomultiplier tubes for 'Bialkali','Super Bialkali' and 'Ultra Bialkali' technology.*

2.9.5 Magnetic field immunity

Unlike classical photomultiplier tubes that can not operate in high magnetic fields due to bending of electron trajectories, HAPD performance is improved by it. Magnetic field that is perpendicular to the entrance window of HAPD causes electrons to circulate along the magnetic field lines and consequently they fall where they should. Therefore, magnetic field decreases distortion due to a non-uniform electric field at the edge and eliminates photoelectron backscattering cross-talk.

2.9.6 Measurements of the leakage current of the HAPD chips

We measured the leakage current for each of the chips (A-D) by changing the bias voltage. Figure 2.32 shows the variation of leakage currents. As we expected it suddenly grows up after a certain voltage.

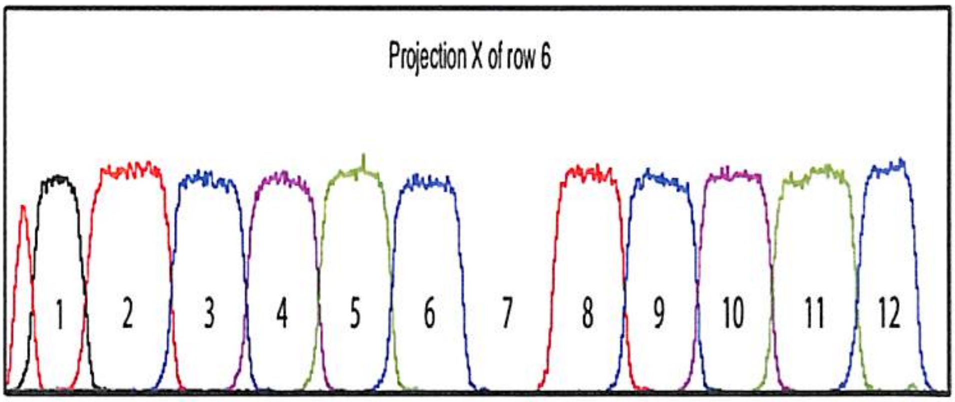

FIGURE 2.28: *One dimensional scan of a row done on a testing HAPD.*

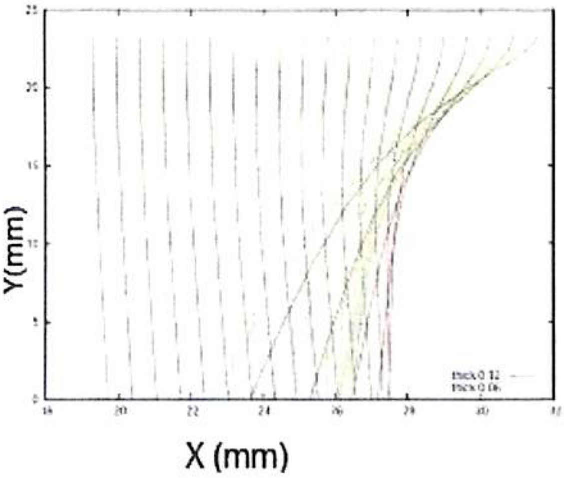

FIGURE 2.29: *Electron trajectories in B=0 Tesla.*

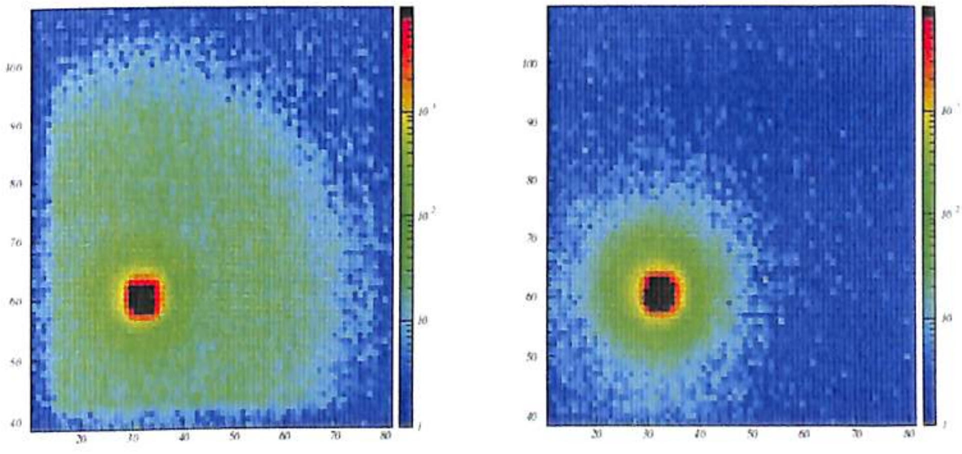

FIGURE 2.30: *Electron backscattering with B=0 Tesla (left) and B=1.5 Tesla (right).*

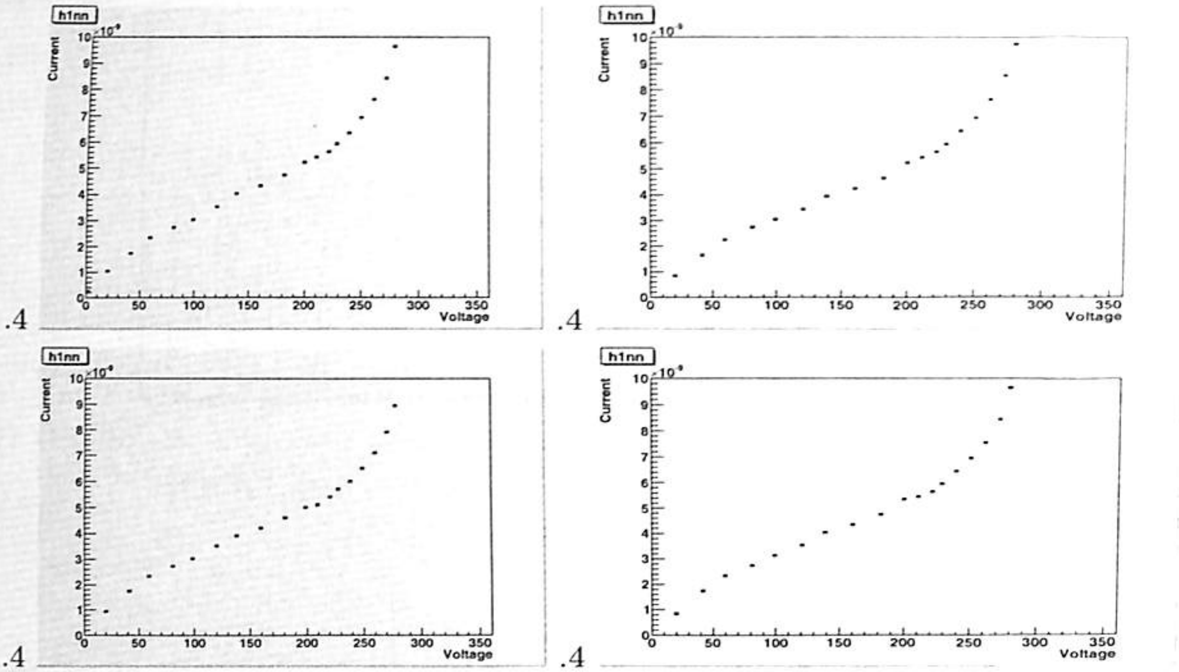

FIGURE 2.31: *Leakage current of HAPD chips.*

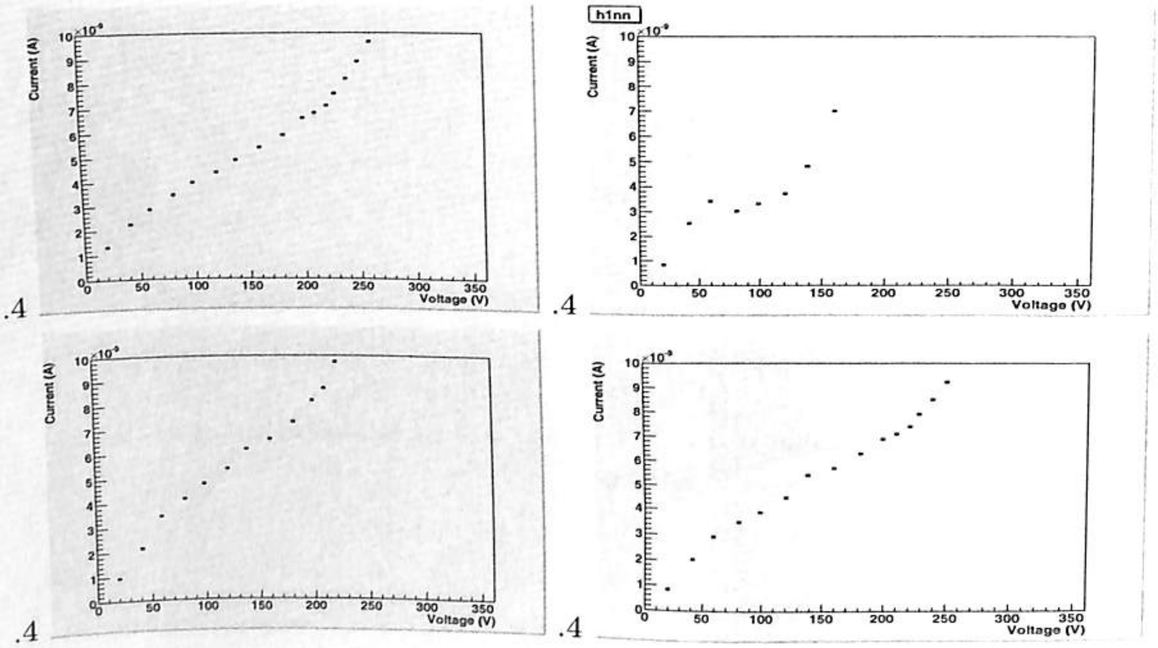

FIGURE 2.32: *Leakage current of HAPD chips showing one of the chips is not working properly.*

2.9.7 Performance of the HAPD in the Magnetic Field

We see the performance of the HAPD in the 1.5 Tesla magnetic field. Before putting the HAPD in the magnetic field we aligned all the 144 channels at a certain threshold value. Figure 2.33 shows the threshold scan before and after the alignment.

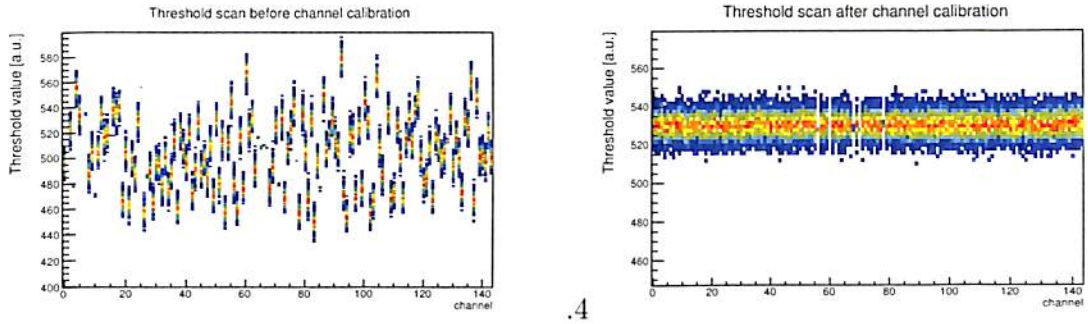

.4 .4

FIGURE 2.33: *Threshold scan before and after channel calibration.*

After the alignment of the channels we put HAPD in the 1.5 Tesla magnetic field. Figure 2.34 shows the response of the HAPD channels to the trigger. The right plot has a very large dead time and the left one is without dead time.

Right plot of Figure 2.35 shows the number of HAPD with fraction of dead time and the left one shows the fraction of dead time with HAPD serial number.

Figure 2.36 shows the statistics of the HAPD measured.

2.9.8 Conclusion

From the study of the performance of the HAPD in 1.5 Tesla magnetic field we can conclude that some of the HAPD have very large dead time. We do not find any

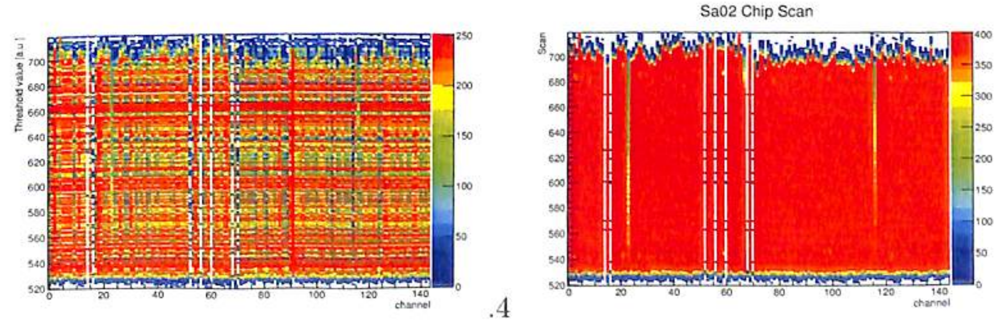

.4 .4

FIGURE 2.34: *Threshold scan plot for HAPD having small and large dead time.*

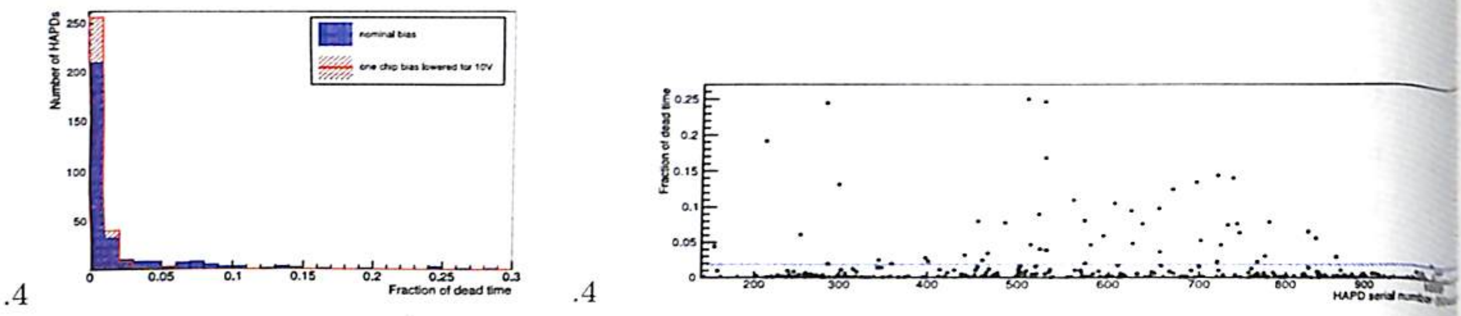

.4 .4

FIGURE 2.35: *Number of HAPD with fraction of dead time (right) and fraction of dead time with HAPD serial number (left).*

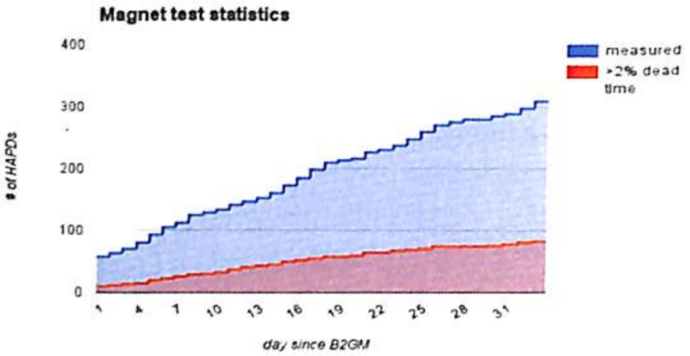

FIGURE 2.36: *Statistics of the HAPD measured.*

meaningful behavior of the measured quantities.

2.10 Chapter summary

This chapter gives a brief introduction of the KEKB accelerator, the Belle detector, trigger system used for signal selection and the DAQ used for data acquisition. It also includes a section on my hardware contribution, namely to the construction of the HAPD detector for Belle II experiment.

Chapter 3

Signal selection and Event reconstruction

This chapter provides the analysis procedure applied in searching for the decay $B_s^0 \to \eta\eta$ at $\Upsilon(5S)$ resonance. It describes the different steps of the analysis: datasets used, event reconstruction, the blind analysis technique applied in the analysis and the separation of signal from background events. We use different kinematic, likelihood based selection for different particles and event shape variables to discriminate the signal from the background like events. First we use loose selection criteria on the variables to reconstruct the events that ensures higher reconstruction efficiency. The selection criteria are further optimized using signal significance as the figure of merit (FOM) in the final stage of the analysis. Neural Network, a multivariate analysis tool is used to suppress the dominating backgrounds. A best candidate selection (BCS) criteria is also applied for the events having multiplicity greater than one. Signal selection efficiency is computed based on the number of events surviving all the selection criteria.

3.1 Analysis Strategy

We are using $\eta \to \gamma\gamma$ and $\eta \to \pi^+\pi^-\pi^0$ decay modes to reconstruct our $B_s^0 \to \eta\eta$ decay. The $B_s^0 \to \eta\eta$ candidate events are reconstructed by first reconstructing (a) both the η's from $\eta \to \gamma\gamma$ decay, followed by reconstruction of $B_s^0 \to \eta_{\gamma\gamma}\eta_{\gamma\gamma}$ (b) both the η's from $\eta \to \pi^+\pi^-\pi^0$ decay, followed by reconstruction of $B_s^0 \to \eta_{3\pi}\eta_{3\pi}$ and (c) one η from $\eta \to \gamma\gamma$ decay while the other η from $\eta \to \pi^+\pi^-\pi^0$ decay, followed by reconstruction of $B_s \to \eta_{\gamma\gamma}\eta_{3\pi}$. These two modes cover 62.33% (39.41 % for $\eta \to \gamma\gamma$ and 22.92 % $\eta \to \pi^+\pi^-\pi^0$ (PDG)) of the total decay width of η.

We perform a blind analysis to avoid bias in selecting the criteria that separates the signal from background. Signal and background Monte Carlo (MC) events are generated using the EvtGen event generator [52]. The generated MC events are passed through a GEANT based detector simulator, followed by event reconstruction to generate a MC data sample that is equivalent to the real data sample from the e^+e^- collision. The salient points of the adopted analysis strategy are the followings:

- Perform a blind analysis, since the decay mode is rare, with an expectation of very few signal events in the entire Belle dataset. Blind analysis is a technique in which signal and background MC samples are used to identify the event selection criteria which are further optimized using signal significance as the FOM. Once the entire analysis is performed using the MC samples including the signal extraction technique based on maximum likelihood fit, the same methodology is applied to the real data sample to extract the final signal and background yields. This is done to avoid experimenter's bias in selecting the selection criteria to select the signal over the background. This requires:
  - Pre-identification of all the possible backgrounds.
  - Generate MC samples for both signal and background to optimize the selection criteria and to study the variables that discriminate the signal from the backgrounds.
  - Reconstruct $B_s^0 \to \eta\eta$ signal candidates with loose pre-selection criteria. Run the same event reconstruction algorithm on the background MC samples to understand the backgrounds.
  - Use event shape variables as inputs to a Neural Network (NN) to reject the background originating from light quark (u, d, s, c) production in e^+e^- collision since such backgrounds are the dominating source of background in this analysis.

- Parameterize the signal and background probability density function (PDF) using signal and background MC samples.
- Perform an unbinned maximum likelihood fit to extract the signal and background yields from the remaining events.
- Estimate the statistical and systematic uncertainties.
- Calculate the BR if a significant signal yield is observed, otherwise estimate 90% Confidence Level (CL) upper limit.

3.1.1 Data Samples

The search for the decay, $B_s^0 \to \eta\eta$ is based on 121.4 $fb^{-1}\Upsilon(5S)$ data sample collected by the Belle detector, which corresponds to 14.2×10^6 B_s^0 events. The data used in this analysis was collected using SVD2. Data collected using SVD2 has been reprocessed using improved track finding and photon reconstruction algorithm [42].

3.1.2 Monte Carlo (MC) Samples

Both signal and background MC simulated events are generated to optimize the signal selection criteria, estimate the signal reconstruction and selection efficiency, study background sources and to parameterize the signal and background shapes. Thus they play a vital role in optimizing and characterizing the physics processes. MC production process involves two steps: event generation and modeling of detector response. Events are generated according to various physics processes using a decay table, which specifies the decay models, modes, branching fractions, etc for all possible particles involved in the decay chain. The event generation is done using the EvtGen [52] event generator package, designed for B meson decays based on particle properties (mass, width, lifetime, charge, etc). The generated particles are then passed through GEANT [53–55] to simulate the detector response, after adding the background and data files are generated for analysis that match the real data formats.

3.1.2.1 Signal MC

We have generated 100,000 $B_s \to \eta\eta$ signal MC events for each of these three B_s decay modes: $B_s \to \eta_{\gamma\gamma}\eta_{\gamma\gamma}$, $B_s \to \eta_{\gamma\gamma}\eta_{3\pi}$ and $B_s \to \eta_{3\pi}\eta_{3\pi}$. The decay models used to generate the signal MC events are summarized as follows:

Models used for $\eta \to \gamma\gamma$

- N-Body Phase Space (PHSP) to generate $\Upsilon(5S) \to B_s^{0*}\bar{B}_s^{0*}$ and $\Upsilon(5S) \to B_s^{0*}\bar{B}_s^{0}$ events.
- Vector to Scalar Scalar (VSS) to generate $\Upsilon(5S) \to B_s^0\bar{B}_s^0$ events.
- Vector to Scalar Photon (VSPPWAVE) to generate $B_s^{0*} \to B_s^0\gamma$ events.
- Photos Phase Space (PHOTOS PHSP) to generate $B_s^0 \to \eta\eta$ events.
- Phase Space (PHSP) to generate $\eta \to \gamma\gamma$ events.

Models used for $\eta \to \pi^+\pi^-\pi^0$

- N-Body Phase Space (PHSP) to generate $\Upsilon(5S) \to B_s^{0*}\bar{B}_s^{0*}$ and $\Upsilon(5S) \to B_s^{0*}\bar{B}_s^{0}$ events.
- Vector to Scalar Scalar (VSS) to generate $\Upsilon(5S) \to B_s^0\bar{B}_s^0$ events.
- Vector to Scalar Photon (VSPPWAVE) to generate $B_s^{0*} \to B_s^0\gamma$ events.
- Photos Phase Space (PHOTOS PHSP) to generate $B_s^0 \to \eta\eta$ events.
- PHOTOS ETA-DALITZ to generate $\eta \to \pi^+\pi^-\pi^0$ events.
- PHSP to generate $\pi^0 \to \gamma\gamma$ events.

3.1.2.2 Background MC

The dominant source of background for the decay is the production of light quark-antiquark pairs ($q = u, d, s, c$) in the e^+e^- annihilation, identified as continuum background. Generic $B_s(B_s^{(*)}\bar{B}_s^{(*)})$ $(bsbs)$ and non- $B_s(B^*\bar{B}^*\pi, \Upsilon(4S)\gamma)$ $(nonbsbs)$

decays of $\Upsilon(5S)$, and two photon process resulting from π^0 decays also contribute to the backgrounds. Dedicated MC samples for these processes are generated to study the background. Six streams of the following background MC samples are used in this analysis:

- uds ($e^+e^- \to u\bar{u}, d\bar{d}, s\bar{s}$)
- charm ($e^+e^- \to c\bar{c}$)
- bsbs ($e^+e^- \to \Upsilon(5S) \to B_s^{(*)}\bar{B}_s^{(*)}$)
- nonbsbs ($e^+e^- \to \Upsilon(5S) \to B^*\bar{B}^*\pi, \Upsilon(4S)\gamma$)

Each stream corresponds to $121.4 fb^{-1}$ of data, i.e., the luminosity of the $\Upsilon(5S)$ real data sample used in this analysis.

3.1.3 Signal Selection and Event Reconstruction

3.1.3.1 Photon Selection

Photons are identified as energy deposition in the ECL that are not matched to a charged track. Candidate photons are required to have a minimum energy (E_γ) of 100 MeV. The other selection criteria are described below:

- Daughter photons from π^0 decays contribute to backgrounds. They are rejected on the basis of likelihood information ($\mathrm{P}^0_\pi(\gamma)$) obtained using energy and polar angle of the photons and the diphoton invariant mass. $\mathrm{P}^0_\pi(\gamma)$ denotes the maximum probability that a candidate photon can be combined with another photon in the event to form a π^0 particle. We select photons only if $\mathrm{P}^0_\pi(\gamma) < 0.5$.
- Due to the long decay time of the CsI crystals, QED processes like Bhaba scattering or $e^+e^- \to \gamma\gamma$ events can leave two perfectly back-to-back clusters in the ECL and can very well mimic the $\eta \to \gamma\gamma$ events. This off-time QED background can be removed by requiring that the photons hit the ECL cluster

within 9 to 11 micro-seconds of the collision. As the timing information is not simulated, a selection based on MC truth information is used to remove such background from the simulated samples with an equal efficiency.

- To reject neutral hadrons like K_L^0 mesons, neutrons, π^0 etc. we use information about the shower shapes since electromagnetic and hadronic showers have different shapes in both the transverse and longitudinal directions. Shower shapes in the transverse direction can be evaluated by using the variable $E9/E25$, which is the ratio of the energies summed in 3×3 array of crystals to that of 5×5 crystals in the transverse plane around the crystal with the largest energy deposit. Shower caused by hadrons grow wider than the electromagnetic showers due to multiple showers caused by hadrons. For each ECL cluster, we require the ratio to be greater than 0.95 [56].

3.1.3.2 Selection of charged tracks

To select charged tracks we use three variables δr, δz and p_T, where δr and δz are the distance between the IP and the point of closest approach in the plane perpendicular to the beam axis ($r - \phi$ plane) and along the beam direction (z axis), respectively. We impose requirements on these variables to be $|\delta r| < 0.3$cm, $|\delta z| < 3$cm and $p_T > 0.1 GeV c^{-1}$. In addition to these variables we have also applied kaon identification (KID), muon identification (μID) and electron identification (eID) likelihoods. For π^+ and π^- selection we require $KID < 0.4$, $\mu ID < 0.95$ and $eID < 0.95$. Here, KID, μID and eID are the likelihood of the track to be coming from a kaon, muon and electron respectively. The likelihoods are calculated on the basis of dE/dx measurement by CDC, the Cherenkov light yield in ACC and the time of flight information from TOF by taking the product of the likelihood functions for three discriminants i.e.,

$$\mathcal{L}_i = \mathcal{L}_i^{\mathrm{dE/dx}}.\mathcal{L}_i^{\mathrm{ACC}}.\mathcal{L}_i^{\mathrm{TOF}}(i = K, \mu, e^-)$$

3.1.3.3 Selection of π^0

π^0s are reconstructed from two gammas. To select π^0, we require $117 MeV < m_{\pi^0} < 149 MeV$ and we also perform a mass constrained fit and require the $\chi^2_{\pi^0} < 50$.

Figure 3.1 shows the π^0 mass distributions and its parameterization. From the parameterization, we have seen that the reconstructed π^0 mass peaks at around 135 MeV with a width of about 5 MeV which agrees with the PDG value of π^0 mass.

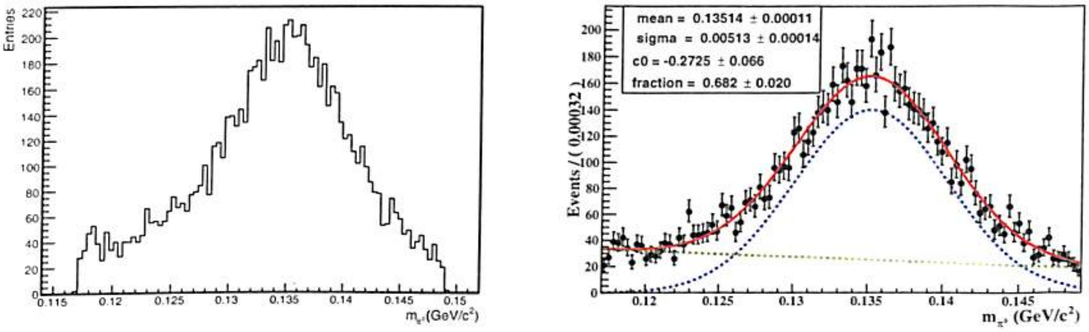

FIGURE 3.1: π^0 *mass distributions(left) and its parameterization(right).*

3.1.3.4 Selection of η

The η candidates are reconstructed by combining a pair of selected gammas having an invariant mass, $M_{\gamma\gamma}$ within $0.5 < m_{\eta_{\gamma\gamma}} < 0.6$ GeV/c^2 of the nominal η mass for $\eta \to \gamma\gamma$ mode. For $\eta \to \pi^+\pi^-\pi^0$ mode, the reconstruction is done by combing the selected pions. To select the η candidate for this mode we require 527 MeV $< m_{\eta_{3\pi}} <$568 MeV and we also perform a mass constrained fit and we keep only those η candidates which have $\chi^2_{\eta\to\pi\pi\pi^0} < 200$. Figure 3.2 and 3.3 shows the $\eta_{\gamma\gamma}$ and $\eta_{3\pi}$ mass distributions and their parameterizations. From these parameterizations, we have seen that for both $\eta_{\gamma\gamma}$ and $\eta_{3\pi}$, the reconstructed masses peak around the nominal η mass with widths which agree with the PDG value of η mass.

3.1.3.5 Reconstruction of B_s^0 Meson

B_s^0 meson candidates are formed by combining a pair of η mesons for $B_s^0 \to \eta\eta$ decay. B_s^0 mesons are selected on the basis of the beam constrained mass (M_{bc}) and energy difference (ΔE), defined as:

$$M_{bc} = \sqrt{(E_{beam})^2 - (P_{recon})^2}$$
$$\Delta E = E^{B_s^0}_{recon} - E_{beam}$$

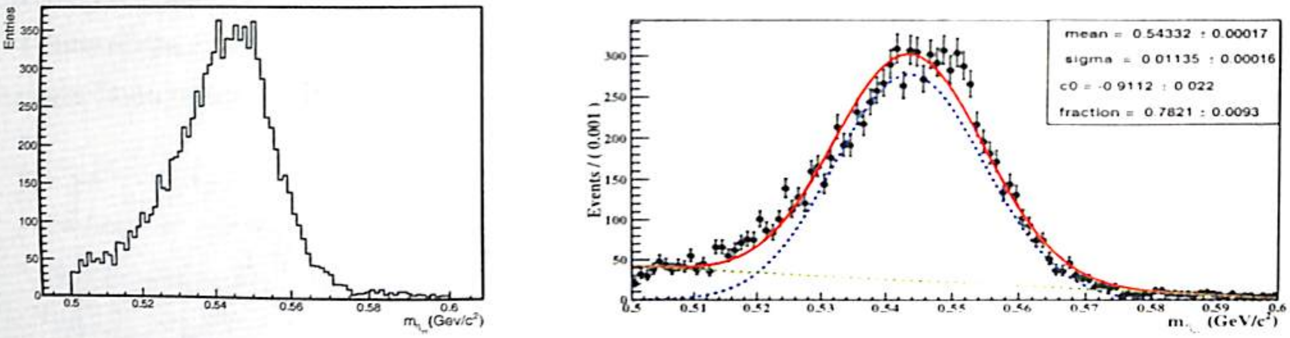

FIGURE 3.2: $\eta_{\gamma\gamma}$ *mass distributions(left) and its parameterization(right).*

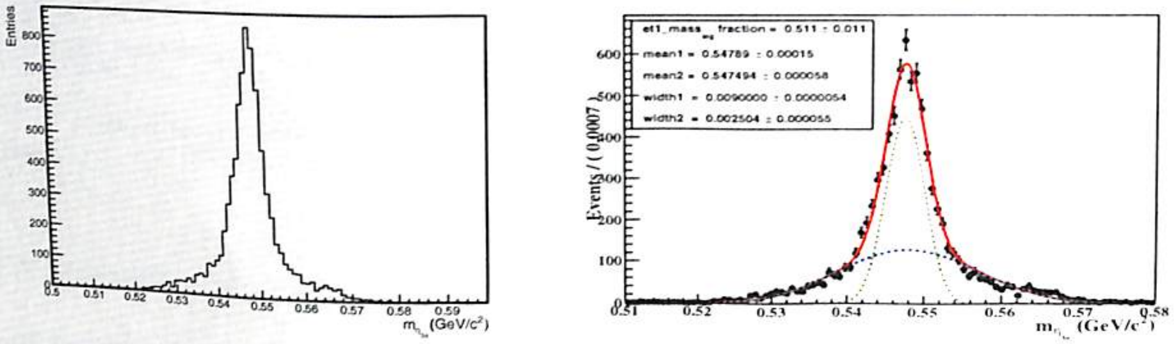

FIGURE 3.3: $\eta_{3\pi}$ *mass distributions(left) and its parameterization(right).*

where E_{beam} is the beam energy, and P_{recon} is the reconstructed momentum of B^0_s and $E^{B^0_s}_{recon}$ is energy of the reconstructed B^0_s, all evaluated in the e^+e^- CM frame. Signal candidates are required to satisfy $5.3 < M_{bc} < 5.435$ GeV/c^2 and $-0.6 < \Delta E < 0.2$ GeV.

The selection criteria to select signal events are given in Table 3.1, 3.2.

Variable	**Selection Criteria**
E_γ	> 50 MeV
π_0 veto	< 0.5
Photon ID	!= 911
$E9/E25$	> 0.95
M_η	0.5$< M_\eta <$ 0.6 GeV
$\chi^2_{\eta\to\gamma\gamma}$	< 50
M_{bc}	$5.3 < M_{bc} < 5.435$ GeV/c^2
ΔE	$-0.6 < \Delta E < 0.2$ GeV

TABLE 3.1: *Signal selection criteria for* $\eta \to \gamma\gamma$ *mode.*

charged tracks	$\lvert dr\rvert < 0.3$ cm, $\lvert dz\rvert < 3.0$ cm, $KID < 0.4, \mu ID < 0.95, eID < 0.95$
$\pi 0$	$117MeV < m_{\pi^0} < 149MeV$ $\chi^2_{\pi^0} < 50$
η	$527MeV < m_{\pi\pi\pi^0} < 568MeV$ $\chi^2_{\eta\to\pi\pi\pi^0} < 200$
B_s^0	$5.3 < M_{bc} < 5.435GeV$ $-0.6 < \Delta E < 0.2GeV$

TABLE 3.2: *Signal selection criteria for $\eta \to \pi^+\pi^-\pi^0$ mode.*

3.2 Signal and Background MC Study

3.2.1 Signal Monte Carlo Analysis

We have processed 100,000 signal MC events for $B_s \to \eta_{\gamma\gamma}\eta_{\gamma\gamma}$, $B_s \to \eta_{3\pi}\eta_{3\pi}$ and $B_s \to \eta_{\gamma\gamma}\eta_{3\pi}$ modes, respectively. The M_{bc} and ΔE distributions for the signal MC samples after the application of the cuts are shown in Figure 3.4, 3.5 and 3.6. As expected, for signal like events, the M_{bc} distribution peaks at around mean value of 5.4 GeV/c^2, whereas ΔE peaks closer to zero for all the three cases.

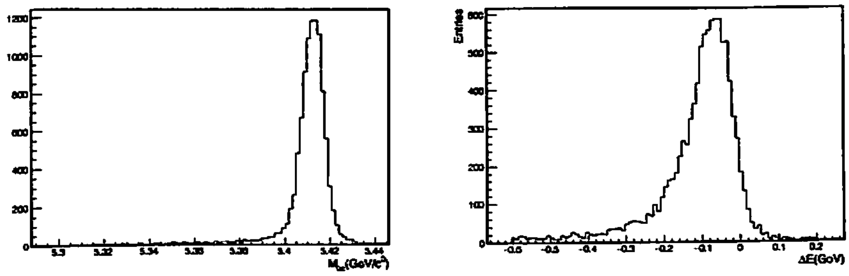

FIGURE 3.4: *M_{bc} (left) and ΔE (right) distributions for signal MC for $B_s^0 \to \eta_{\gamma\gamma}\eta_{\gamma\gamma}$ mode.*

3.2.2 Optimization of selection cuts

We optimize the selection cuts by using signal significance as the figure of merit (FOM). The signal significance is defined as, $\frac{S}{\sqrt{S+B}}$, where S and B are the number of expected signal and background events in this analysis. To find the best value of the selection cut, we vary the value of the variable and find out the

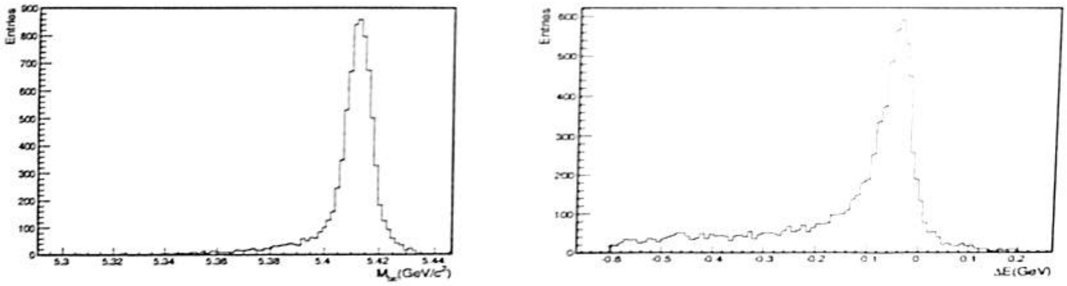

FIGURE 3.5: *M_{bc} (left) and ΔE (right) distributions for signal MC for $B_s^0 \to \eta_{3\pi}\eta_{3\pi}$ mode.*

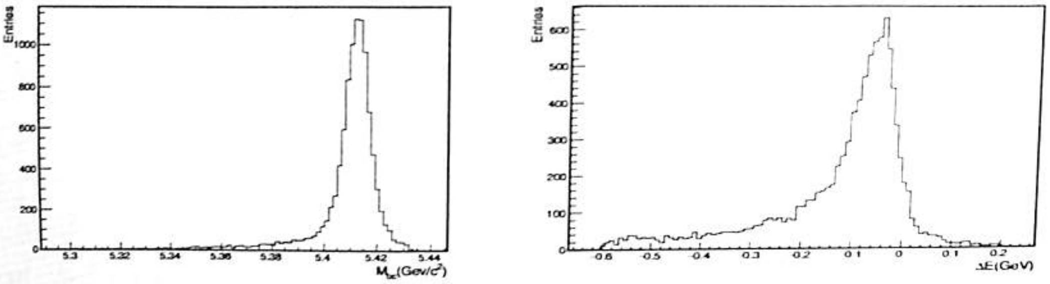

FIGURE 3.6: *M_{bc} (left) and ΔE (right) distributions for signal MC for $B_s^0 \to \eta_{\gamma\gamma}\eta_{3\pi}$ mode.*

value that maximizes the FOM. The distributions of FOM are shown in Figure 3.7, 3.83.9. We use the optimized cut values in this analysis for these variables. The candidates for $\eta_{\gamma\gamma}$, $\eta_{3\pi}$ and π^0 are selected by requiring their fitted mass to be around $\pm 3\sigma$ of their nominal mass. The fitted mass distributions for $\eta_{\gamma\gamma}$, $\eta_{3\pi}$ and π^0 are shown in Figure 3.1, 3.2, 3.3.

3.2.3 True and mis-reconstructed candidates

Since the reconstruction algorithm is not 100% perfect, it is important to estimate the true efficiency for the selection of signal events and also the fraction of mis-reconstructed signal events. The true signal efficiency ϵ_{true} is calculated as the number of truely reconstructed signal events based on the truth ID of the events and the fraction of mis-reconstructed signal events is calculated as the number of mis-reconstructed events divided by the total number of signal events that have passed all the selection cuts. These efficiencies and fractions are summarized in Table 3.3. Figure 3.10, 3.11 and 3.12 show the M_{bc} and ΔE distributions for true and mis-reconstructed event, respectively.

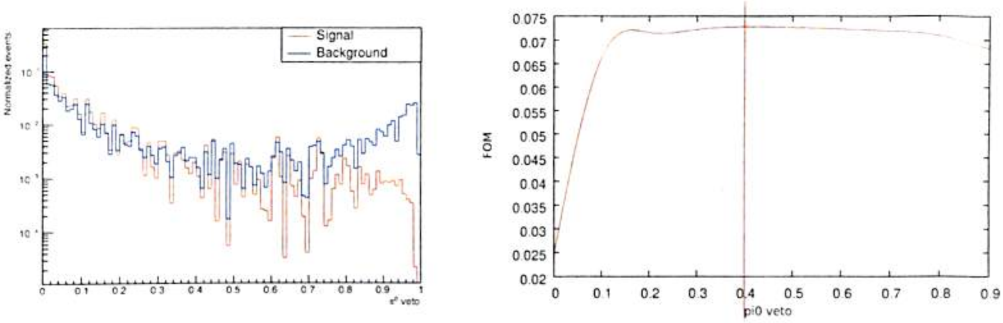

FIGURE 3.7: π^0 *veto for signal and background (left) and the FOM (right) distributions for* $B_s^0 \to \eta_{\gamma\gamma}\eta_{\gamma\gamma}$ *mode. The straight line shows the value of the optimized cut.*

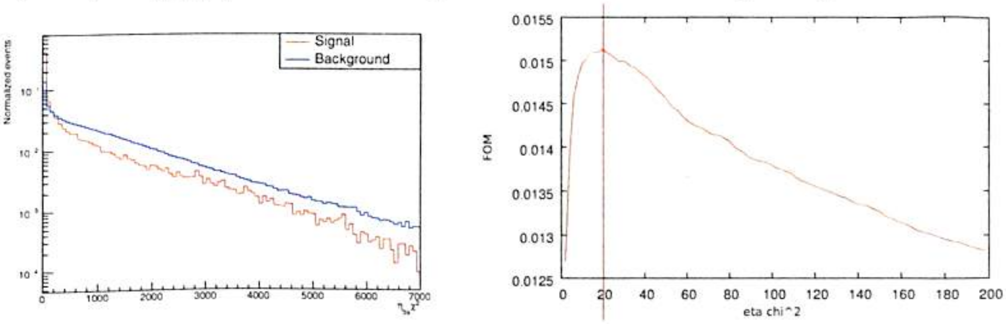

FIGURE 3.8: χ^2_η *for signal and background (left) and the FOM (right) distributions. The straight line shows the value of the optimized cut.*

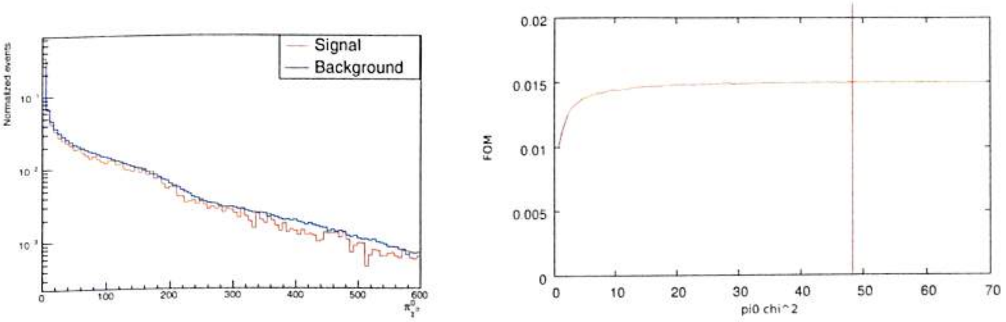

FIGURE 3.9: $\chi^2_{\pi^0}$ *for signal and background (left) and the FOM (right) distributions. The straight line shows the value of the optimized cut.*

3.2.4 Understanding the Peak

To understand the peaking characteristics of the mis-reconstructed events we have simultaneously applied the M_{bc} and ΔE signal region cuts. For $B_s^0 \to \eta_{\gamma\gamma}\eta_{\gamma\gamma}$ mode and $B_s^0 \to \eta_{3\pi}\eta_{3\pi}$ mode, the peak disappears once we apply the signal region cuts which signifies that they are purely reconstructed. For the $B_s^0 \to \eta_{\gamma\gamma}\eta_{3\pi}$ mode the peak decreases significantly once we apply the signal region cut as well. Signal region cuts are applied in Figure 3.13, 3.14 and 3.15.

Decay mode	ϵ_{sig} (%)	ϵ_{true} (%)	f_{mrc} (%)
$B_s^0 \rightarrow \eta_{\gamma\gamma}\eta_{\gamma\gamma}$	10.2	8.8	5.5
$B_s^0 \rightarrow \eta_{\gamma\gamma}\eta_{3\pi}$	9.9	9.03	8.9
$B_s^0 \rightarrow \eta_{3\pi}\eta_{3\pi}$	8.3	7.8	12.9

TABLE 3.3: ***Total signal efficiency*** ϵ_{sig}, ***true signal efficiency*** ϵ_{true}, *mis-reconstructed fraction* f_{mrc}.

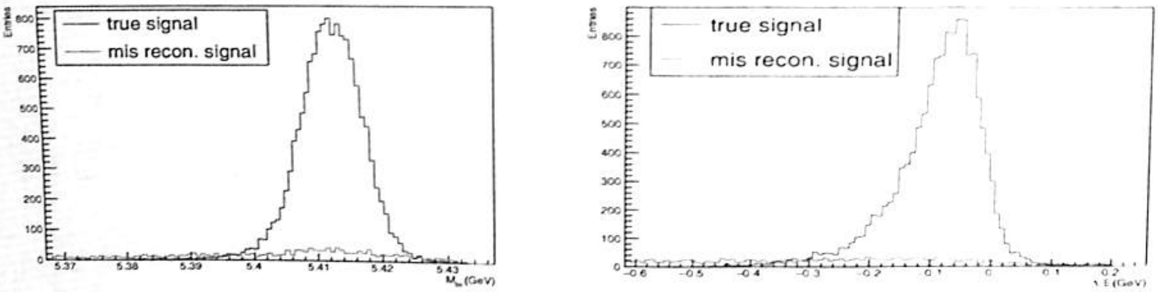

FIGURE 3.10: *M_{bc} (left) and ΔE (right) distributions for true and misreconstructed events for signal MC for $B_s^0 \rightarrow \eta_{\gamma\gamma}\eta_{\gamma\gamma}$ mode.*

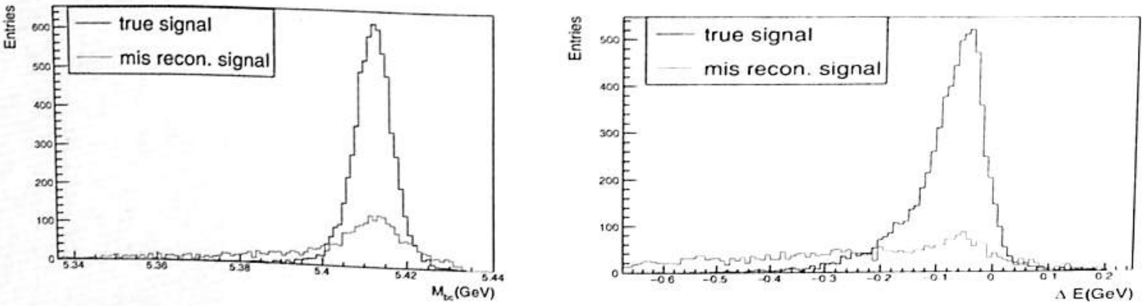

FIGURE 3.11: *M_{bc} (left) and ΔE (right) distributions for true and misreconstructed events for signal MC for $B_s^0 \rightarrow \eta_{\gamma\gamma}\eta_{3\pi}$ mode.*

3.3 Background MC Study

To understand and identify the possible backgrounds in this analysis, we have also processed various background MC samples using our reconstruction code. Belle has collected data at $\Upsilon(5S)$ resonance with five different experiment numbers. Dedicated background MC samples are generated by MC production team in Belle. Each experiment has six streams (0 to 5) of background MC data for different type of backgrounds. Each stream of data corresponds to $121.4 fb^{-1}$ of data, i.e.,the luminosity of the $\Upsilon(5S)$ real data sample.

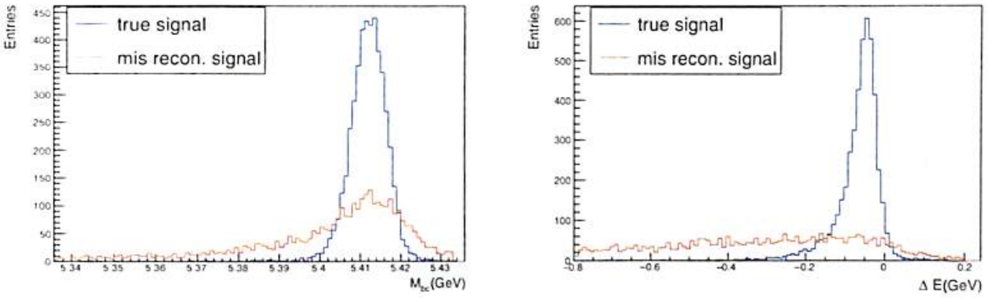

FIGURE 3.12: M_{bc} *(left) and* ΔE *(right) distributions for true and misreconstruced events for signal MC for* $B_s^0 \to \eta_{3\pi}\eta_{3\pi}$ *mode.*

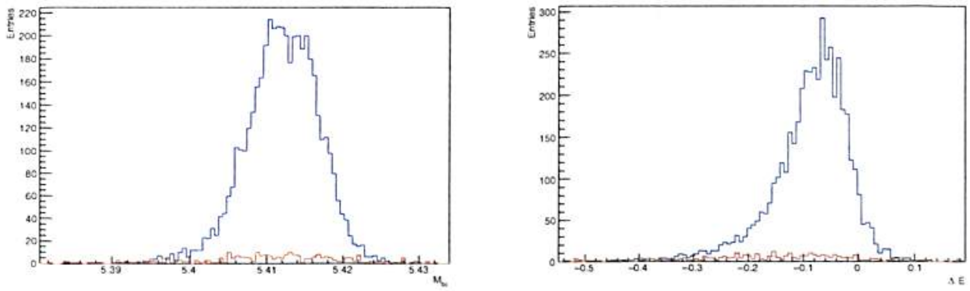

FIGURE 3.13: M_{bc} *(left) and* ΔE *(right) distributions for true and mis-reconstructed events for signal MC for* $B_s^0 \to \eta_{\gamma\gamma}\eta_{\gamma\gamma}$ *mode.*

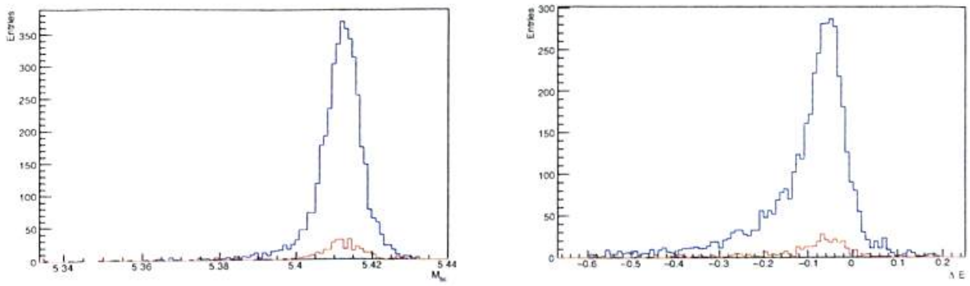

FIGURE 3.14: M_{bc} *(left) and* ΔE *(right) distributions for true and mis-reconstructed events for signal MC for* $B_s^0 \to \eta_{\gamma\gamma}\eta_{3\pi}$ *mode.*

3.3.1 Continuum Background MC Study

Backgrounds arising from light quark continuum events, $e^+e^- \to q\bar{q}, q = u, d, s, c$ are studied. We refer these type of backgrounds as continuum or *udsc*. We have used data of stream 0 of all the five experiments to study continuum backgrounds. We run the same event reconstruction algorithm and selection criteria as the signal on the background MC samples to understand the backgrounds. The M_{bc} and ΔE distributions for these types of backgrounds are shown in Figure 3.16, 3.17 and 3.18.

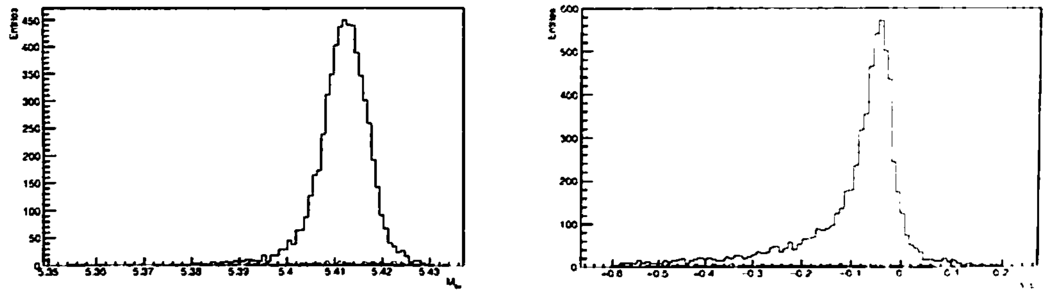

FIGURE 3.15: *M_{bc} (left) and ΔE (right) distributions for true and mis-reconstructed events for signal MC for $B_s^0 \to \eta_{3\pi}\eta_{3\pi}$ mode.*

From these studies we have seen that a significant amount of continuum background events passed the selection criteria.

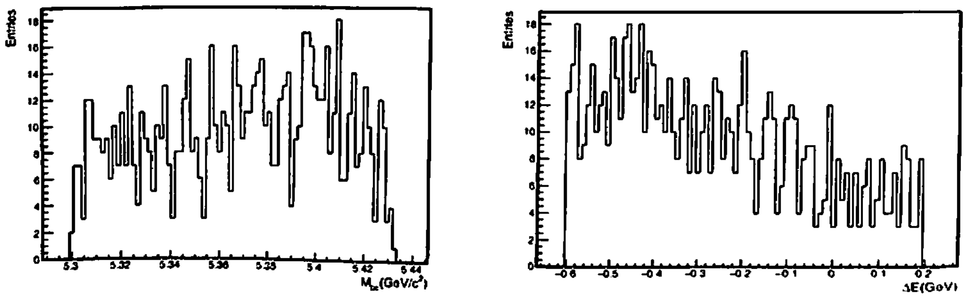

FIGURE 3.16: *M_{bc} (left) and ΔE (right) distributions for continuum udsc background MC for $B_s^0 \to \eta_{\gamma\gamma}\eta_{\gamma\gamma}$ mode.*

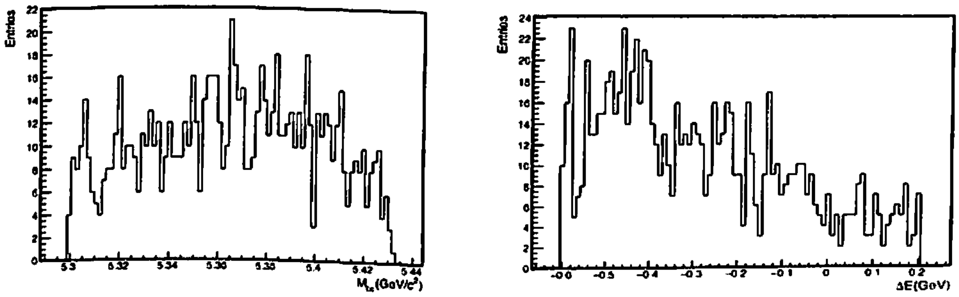

FIGURE 3.17: *M_{bc} (left)and ΔE (right) distributions for udsc background for $B_s^0 \to \eta_{\gamma\gamma}\eta_{3\pi}$ mode.*

3.3.1.1 *bsbs* and *nonbsbs* Background MC Study

Generic B_s ($B_s^{(*)}\bar{B}_s^{(*)}$) and non-B_s ($B^*\bar{B}^*\pi, \Upsilon(4S)\gamma$) decays of $\Upsilon(5S)$ also contribute to the backgrounds. We refer these type of backgrounds as ***bsbs*** and ***nonbsbs*** background respectively. We have also studied the ***bsbs*** and ***nonbsbs*** background MC for

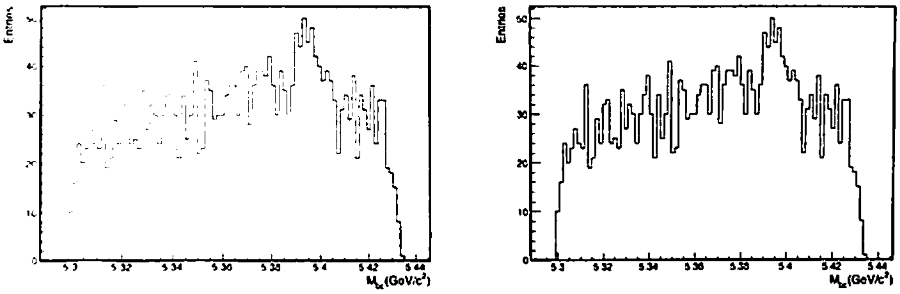

FIGURE 3.18: *M_{bc} (left) and ΔE (right) distributions for udsc background for $B_s^0 \rightarrow \eta_{3\pi}\eta_{3\pi}$ mode.*

all the three decay modes: $B_s^0 \rightarrow \eta_{\gamma\gamma}\eta_{\gamma\gamma}$, $B_s^0 \rightarrow \eta_{3\pi}\eta_{3\pi}$ and $B_s^0 \rightarrow \eta_{\gamma\gamma}\eta_{3\pi}$. We have used data of stream 0 of all the five experiments to study these type of backgrounds. The M_{bc} and ΔE distributions for these types of backgrounds are shown in Figure 3.19, 3.20, 3.21, 3.22, 3.23 and 3.24. From these studies we see that the dominant background for our analysis comes from light quark continuum events. Contribution from *bsbs* and *nonbsbs* background is very small. The expected number of *bsbs* and *nonbsbs* backgrounds after applying the signal region cuts are given in Table 3.4.

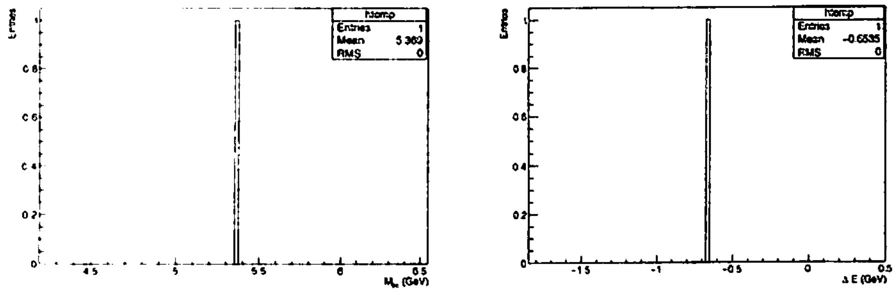

FIGURE 3.19: *M_{bc} (left) and ΔE (right) distributions for bsbs background for $B_s^0 \rightarrow \eta_{\gamma\gamma}\eta_{\gamma\gamma}$ mode.*

Sub decay mode	*bsbs* background	*nonbsbs* background
$B_s^0 \rightarrow \eta_{\gamma\gamma}\eta_{\gamma\gamma}$	0	0
$B_s^0 \rightarrow \eta_{\gamma\gamma}\eta_{3\pi}$	1	0
$B_s^0 \rightarrow \eta_{3\pi}\eta_{3\pi}$	1	0

TABLE 3.4: *Expected number of bsbs and nonbsbs background events in the signal region.*

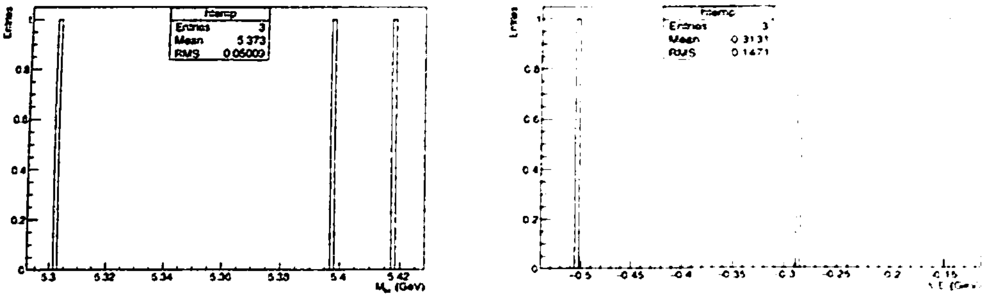

FIGURE 3.20: *M_{bc} (left) and ΔE (right) distributions for nonbsbs background for $B_s^0 \to \eta_{\gamma\gamma}\eta_{\gamma\gamma}$ mode.*

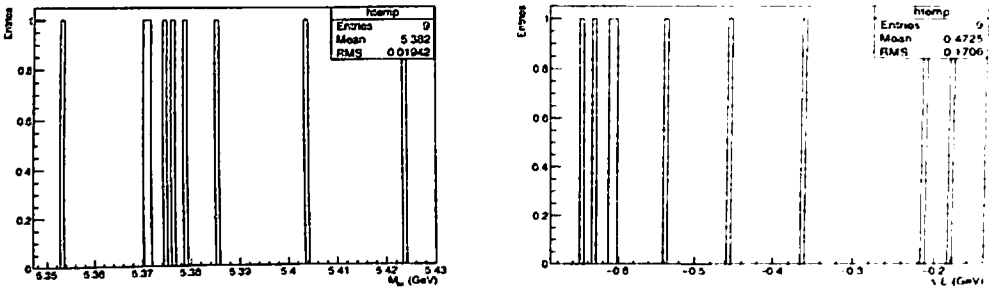

FIGURE 3.21: *M_{bc} (left) and ΔE (right) distributions for bsbs background for $B_s^0 \to \eta_{\gamma\gamma}\eta_{3\pi}$ mode.*

3.3.2 Continuum Background Suppression Using Multivariate Analysis

The dominating background for the decay $B_s^0 \to \eta\eta$ is $e^+e^- \to q\bar{q}$ continuum events where $q = u, d, s, c$. The combined mass of $B_s^* \bar{B}_s^*$ pair is less than that of the $\Upsilon(5S)$ resonance by only a few MeVs. So, the B_s^0 produced at $\Upsilon(5S)$ resonance have very low momentum and their decay products have a random direction, i.e., they have a spherical topology. Since for continuum events, a smaller proportion of e^+e^- energy goes towards particle production, these events have higher momentum and hence are topologically quite distinct from $\Upsilon(5S) \to B_s^* \bar{B}_s^*$ events. Their decay products are distributed mostly along the beam direction, i.e., they have jet like topologies. So, we have used the event shape variables in an event classifier to discriminate this type of background. We have used NeuroBayes in the Neural Network (NN) framework for suppressing the continuum background. We have used modified Fox-Wolfram moments and the absolute value of the cosine of the angle between the thrust axis of the B_s candidate and the rest of the event ($cos\theta$), where the thrust axis is defined as the direction which maximizes the sum of the longitudinal momenta of the particles in the decay as NN input variables.

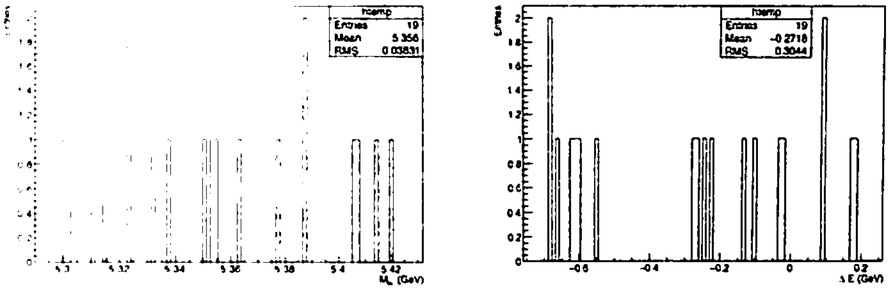

FIGURE 3.22: M_{bc} (left) and ΔE (right) distributions for nonbsbs background for $B_s^0 \to \eta_{\gamma\gamma}\eta_{3\pi}$ mode.

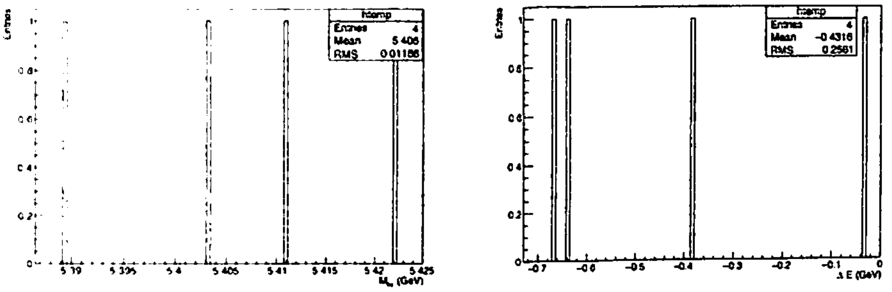

FIGURE 3.23: M_{bc} (left) and ΔE (right) distributions for bsbs background for $B_s^0 \to \eta_{3\pi}\eta_{3\pi}$ mode.

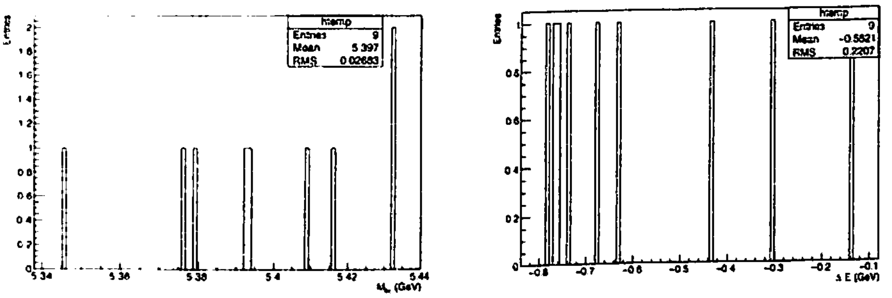

FIGURE 3.24: M_{bc} (left) and ΔE (right) distributions for nonbsbs background for $B_s^0 \to \eta_{3\pi}\eta_{3\pi}$ mode.

3.3.2.1 NeuroBayes(NN) input variables

- **KSFW moments:** To improve the discriminating performance the Fox-Wolfram moments are modified to Kakuno Super Fox-Wolfram (KSFW) [57] moments. KSFW moments are used to characterize the shape of the events from e^+e^- collisions. The KSFW moments are defined as:

$$KSFW = \sum_{l=0}^{4} R_l^{so} + \sum_{l=0}^{4} R_l^{oo} + \gamma \sum_{n=1}^{N_t} |(p_t)_n| \tag{3.1}$$

where R_l^{so} and R_l^{oo} are the modified Fox-Wolfram moments and the third term is the sum of the tranverse momenta in an event, γ is the coefficient and N_t is the number of particles.

In the computation of R_l^{so}, particles are divided into three types: charged particle(c), neutral particle(n) and missing particle(m). The missing particles are constructed because the missing four vector is treated as a particle. R_l^{so} is computed as:

$$R_l^{so} = \frac{\alpha_l^c H_l^{so,c} + \alpha_l^n H_l^{so,n} + \alpha_l^m H_l^{so,m}}{E_{beam} - \Delta E} \tag{3.2}$$

where the $\alpha's$ are the Fisher coefficients and E_{beam} is the beam energy.

For odd value of l, Fox-Wolfram moments are defined as:

$$H_l^{so,n} = H_l^{so,n} = 0 \tag{3.3}$$

$$H_l^{so,c} = \sum_i \sum_{jx} Q_i Q_{jx} |p_{jx}| P_l(cos\theta_{i,jx}) \tag{3.4}$$

where i means the daughter particle of sigal side B, j means that of other side one, x gives the type of particles ($x = c, n, m$), Q_i and Q_{jx} are the charge of the ith and jxth particles, $\theta_{i,jx}$ means the angle between i and jx.

For even value of l Fox-Wolfram moments are defined as:

$$H_l^{so,x} = \sum_i \sum_{jx} |p_{jx}| P_l(cos\theta_{i,jx}) \tag{3.5}$$

R_l^{oo} is defined as:

$$R_l^{oo} = \sum_j \sum_k \beta_l Q_j Q_k |p_j||p_k| P_l(cos\theta_{j,k}) \tag{3.6}$$

for odd value of l.

$$R_l^{oo} = \sum_j \sum_k \beta_l |p_j||p_k| P_l(cos\theta_{j,k}) \tag{3.7}$$

for even value of l.

Where β is free parameter corresponding to Fisher coefficient.

To improve the the signal-to-background separation, Fisher coefficients are optimized in each bin of missing mass square mm^2 as:

$$mm^2 = (E_{\Upsilon} - \sum_{n=1}^{N_t} E_n)^2 - \sum_{n=1}^{N_t} |p_n|^2 \tag{3.8}$$

- $cos\theta_{thrust}$: It is defined as the absolute value of the cosine of the angle between the thrust axis of the decay products of the B candidate and the rest of the event. The thrust axis is defined as the direction which maximizes the sum of the longitudinal momenta of the particles in the decay.

We have used NeuroBayes as Neural Network (NN) to suppress the continuum backgrounds. We used 17 different event shape variables as NN input.Figure 3.25, 3.26 and 3.27 show two of them and as expected they have discriminating power to separate signal and background like events. Rest of the variables are shown in Appendix B.

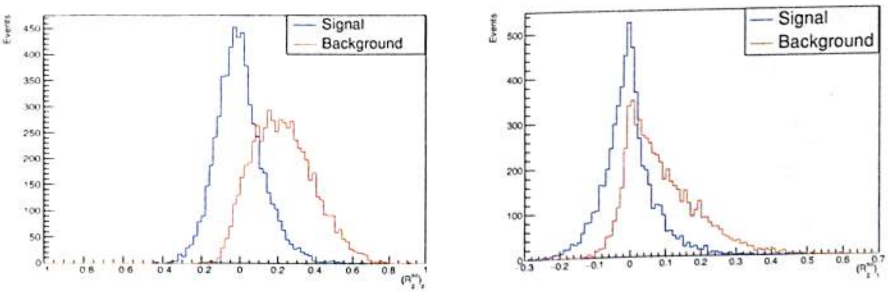

FIGURE 3.25: *Two of the 17 Neural Network (NN) input variables for* $B_s^0 \to \eta_{\gamma\gamma}\eta_{\gamma\gamma}$ *mode .*

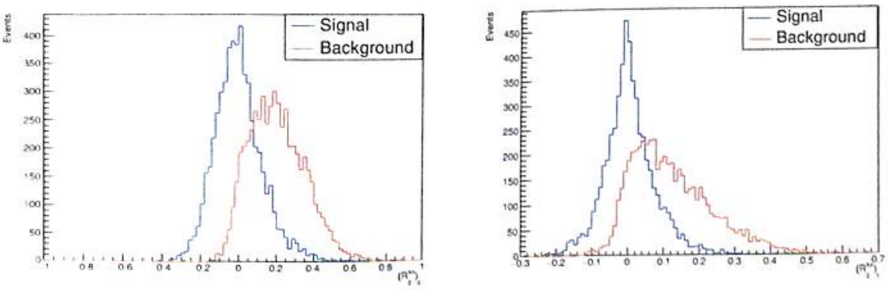

FIGURE 3.26: Two of the 17 Neural Network (NN) input variables, for $B_s^0 \to \eta_{\gamma\gamma}\eta_{3\pi}$ mode.

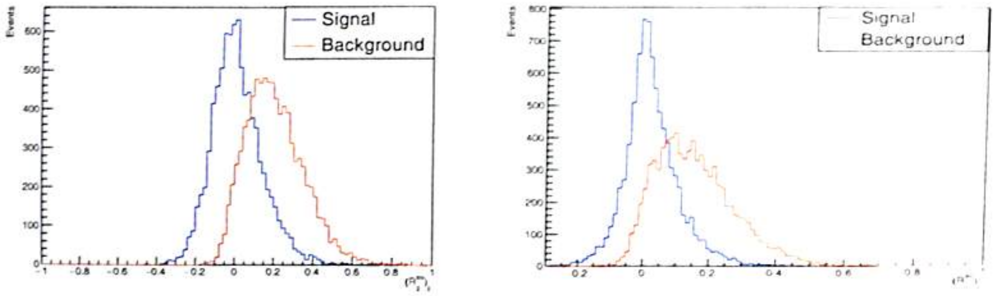

FIGURE 3.27: *Two of the 17 Neural Network (NN) input variables, for $B_s^0 \to \eta_{3\pi}\eta_{3\pi}$ mode.*

3.3.2.2 NeuroBayes Training, Validation and Over training check

The basic aim of any classification problem is to distinguish between various types of events based on a number of discriminating variables. In HEP experiments, generally one wants to distinguish between signal and background. In general, the task of a multivariate method is to map an n-dimensional input variable space into a single scalar which contains all information including the correlations amongst the input variables. The single variable then can be used as a discriminant instead of using all input variables separately. To use a multivariate classifier, it has to be trained first. For such training, one needs a large set of data for which the truth is known. Using a dataset of signal and continuum background events where the truth for every entry is known, the parameters of the classifier are determined in such a way that the classifier output is as close to the known truth as possible. The performance of a classifier is characterized by its efficiency E and purity P, defined as:

$$E = N_{Selected/N_S}$$
$$P = N_{Selected}/N_{Total}$$

where, $N_{Selected}$ is the number of selected signal events, N_S is the total number of signal events and N_{Total} is the number of selected signal and background events. Any classifier should ideally have high efficiency as well as high purity. We have used NeuroBayes, a Belle standard neural network package. Figure 3.28, 3.29 and 3.30 show the purity vs. efficiency plot and the purity vs. network output. For a well trained network, the purity as a function of NeuroBayes output should be on the diagonal.

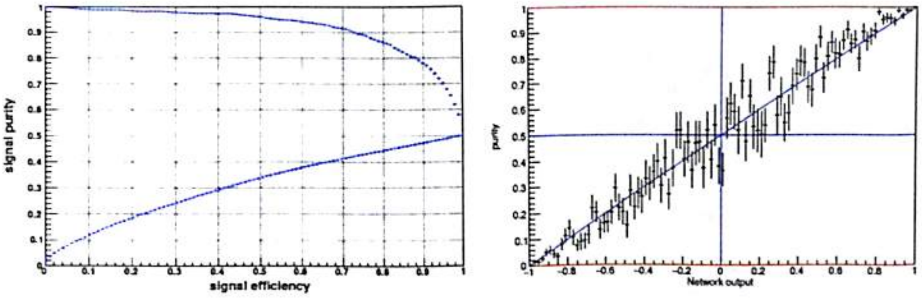

FIGURE 3.28: *Performance plots of NeuroBayes training for* $B_s^0 \to \eta\eta$ *analysis. Purity vs. efficiency (left) and Purity vs. network output (right) for* $B_s^0 \to \eta_{\gamma\gamma}\eta_{\gamma\gamma}$ *mode.*

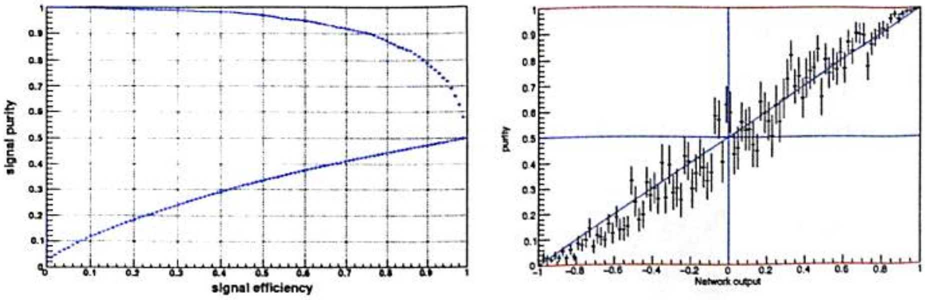

FIGURE 3.29: *Performance plots of NeuroBayes training for* $B_s^0 \to \eta\eta$ *analysis. Purity vs. efficiency (left) and Purity vs. network output (right) for* $B_s^0 \to \eta_{\gamma\gamma}\eta_{3\pi}$ *mode.*

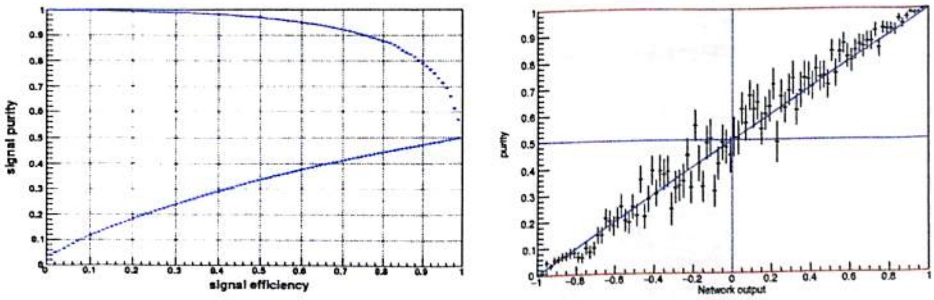

FIGURE 3.30: *Performance plots of NeuroBayes training for* $B_s^0 \to \eta\eta$ *analysis. Purity vs. efficiency (left) and Purity vs. network output (right) for* $B_s^0 \to \eta_{3\pi}\eta_{3\pi}$ *mode.*

We have divided the entire MC sample into 2 parts for both signal and background MC analysis. We have used $2/3^{rd}$ in training and $1/3^{rd}$ for validation. The neural network is trained by calling the NeuroBayes teacher which sets up the network topology and performs the actual training. At the end of the training, the trained network (called the expertise) is written to a file. The file contains all information needed to run an analysis e.g., the network parameters and all weights. After the training, the NeuroBayes expert is used for analyzing the unknown events.

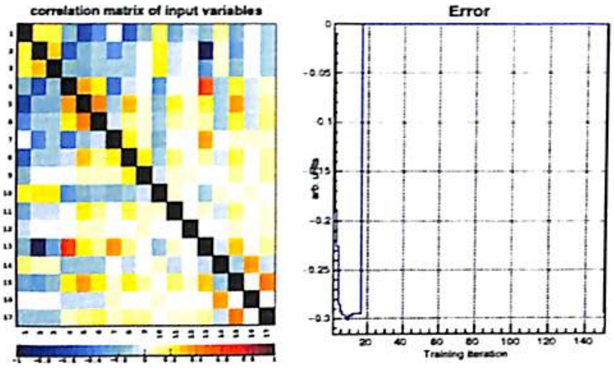

FIGURE 3.31: *Correlation matrix (left) and error vs. iteration plot (right) for* $B_s^0 \rightarrow \eta_{\gamma\gamma}\eta_{\gamma\gamma}$ *mode.*

The training job prints out analysis information such as linear correlation matrix between the input variables and with the target, purity vs. efficiency plot, network architecture, errors vs. iteration for training sample.

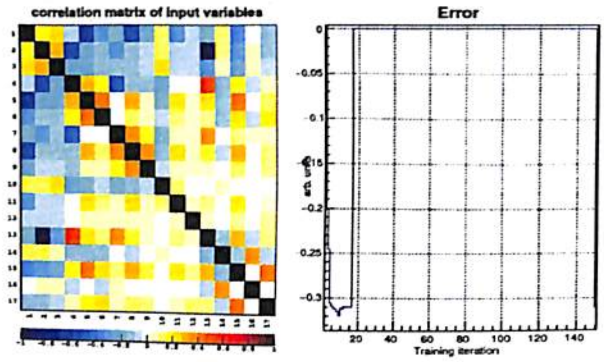

FIGURE 3.32: *Correlation matrix (left) and error vs. iteration plot (right) for* $B_s^0 \rightarrow \eta_{\gamma\gamma}\eta_{3\pi}$ *mode.*

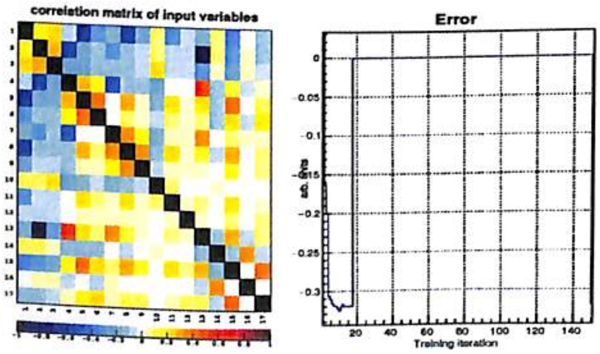

FIGURE 3.33: *Correlation matrix (left) and error vs. iteration plot (right) for* $B_s^0 \rightarrow \eta_{3\pi}\eta_{3\pi}$ *mode.*

We have used signal and continuum background MC sample in the NeuroBayes classifier for the training and validation. For training, we have used $2/3^{rd}$ of the available MC sample remaining after applying all the selection criteria. After training, we provide the remaining $1/3^{rd}$ sample (called test or validation) to the network and it separates out the signal and background events on the basis of training. To check whether over training has occurred or not, we have superimposed the results for training and validation as shown in Figure 3.34 and 3.35. It shows the NeuroBayes outputs in the linear scale. We find acceptable consistency between the training and validation samples which signifies that there is no over training.

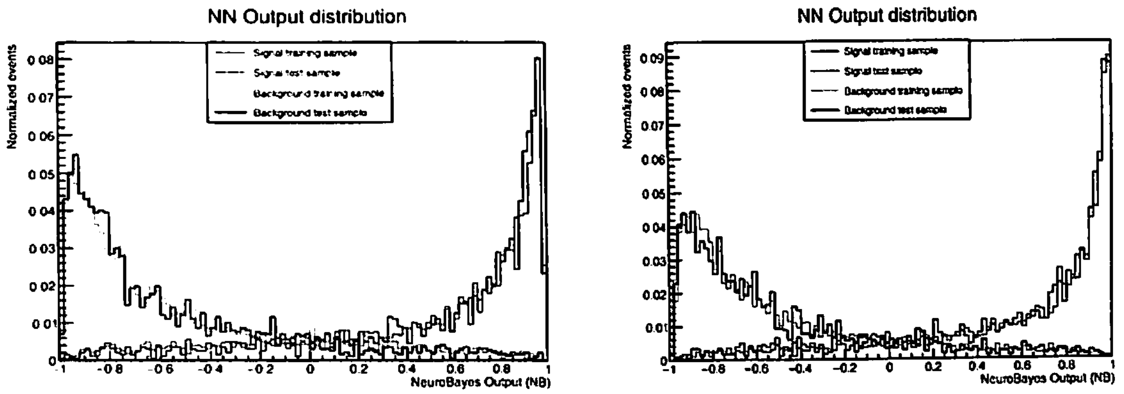

FIGURE 3.34: *Neural Network (NN) output NB for training and validation samples for $B_S^0 \to \eta_{\gamma\gamma}\eta_{\gamma\gamma}$ (left) and $B_S^0 \to \eta_{\gamma\gamma}\eta_{3\pi}$ (right) mode.*

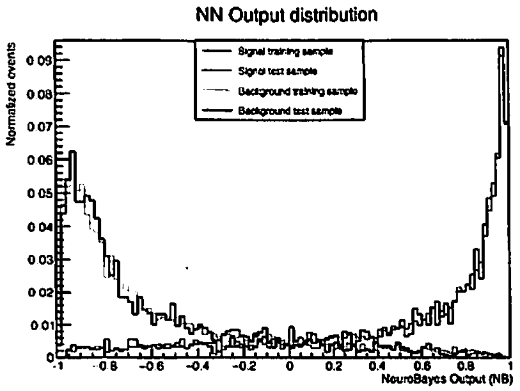

FIGURE 3.35: *Neural Network (NN) output NB for training and validation samples for $B_S^0 \to \eta_{3\pi}\eta_{3\pi}$ mode.*

3.3.2.3 Modified NeuroBayes Output (NB')

It is very difficult to model the NeuroBayes output (NB) distribution with a simple analytic function. Thus to improve the modeling, the modified NeuroBayes output is calculated as:

$$NB' = log[\frac{NB - NB_{cut}}{NB_{max} - NB}]$$

where, $NB_{cut} = -0.6$ and $NB_{max} = 1$. NB max is not really at 1. It is 0.991708 for $B_s^0 \rightarrow \eta_{\gamma\gamma}\eta_{\gamma\gamma}$ mode, 0.982752 for $B_s^0 \rightarrow \eta_{\gamma\gamma}\eta_{3\pi}$ mode and 0.997368 for $B_s^0 \rightarrow \eta_{3\pi}\eta_{3\pi}$ mode. So, when $NB_{max} = NB$ it becomes undefined. So we put $NB_{max} = 1$. Figure 3.36 and 3.37 show the NB' distributions for signal and background MC with an NB_{cut} at -0.6.

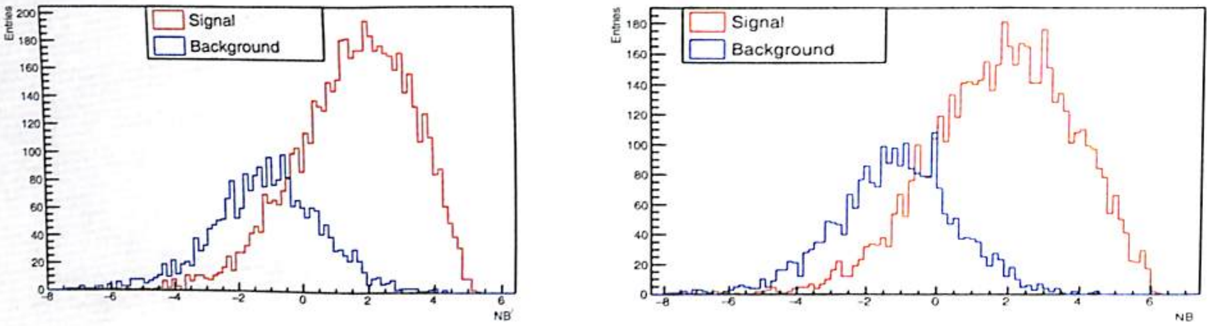

FIGURE 3.36: *Distributions of* NB' *for* $B_s^0 \rightarrow \eta_{\gamma\gamma}\eta_{\gamma\gamma}$*(left) and* $B_s^0 \rightarrow \eta_{\gamma\gamma}\eta_{3\pi}$*(right) mode.*

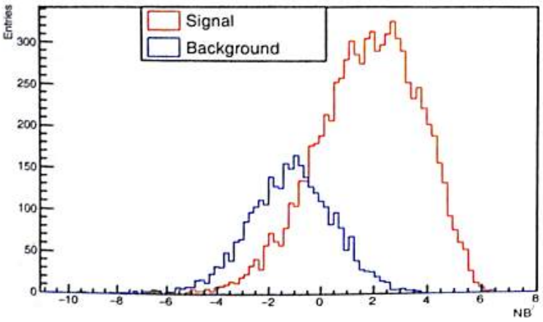

FIGURE 3.37: *Distributions of* NB' *for* $B_s^0 \rightarrow \eta_{3\pi}\eta_{3\pi}$ *mode.*

3.4 Multiplicity of B_s^0 candidate per event

After we apply $NB_{cut} > -0.6$, the average multiplicity of B_s^0 candidates are 1.06,1.196 and 1.381 in $B_s^0 \rightarrow \eta_{\gamma\gamma}\eta_{\gamma\gamma}$, $B_s^0 \rightarrow \eta_{\gamma\gamma}\eta_{3\pi}$ and $B_s^0 \rightarrow \eta_{3\pi}\eta_{3\pi}$ modes, respectively which are shown in Figure 3.38, 3.39.

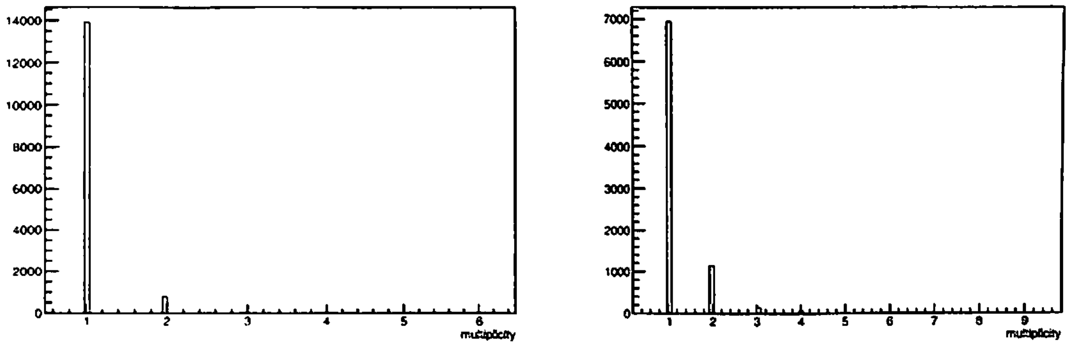

FIGURE 3.38: *Multiplicity for* $B_s^0 \to \eta_{\gamma\gamma}\eta_{\gamma\gamma}$ *(left) and* $B_s^0 \to \eta_{\gamma\gamma}\eta_{3\pi}$ *(right).*

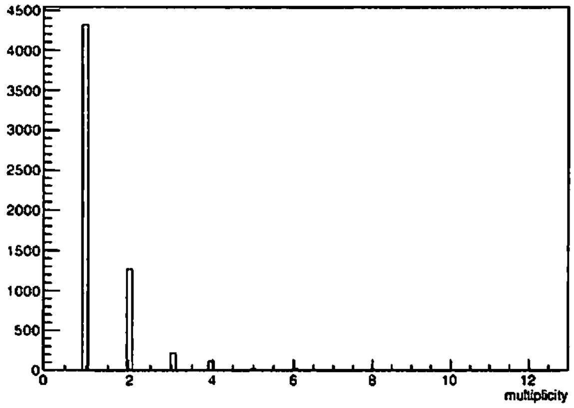

FIGURE 3.39: *Multiplicity for* $B_s^0 \to \eta_{3\pi}\eta_{3\pi}$.

3.5 Best Candidate Selection(BCS)

We require only one B_s^0 candidate per event. We select the best candidate by minimizing the sum of the two chi-squares from two η mass constraint fits. The multiplicity of the three modes are shown in Figure 3.40, 3.41 after performing the best candidate selection.

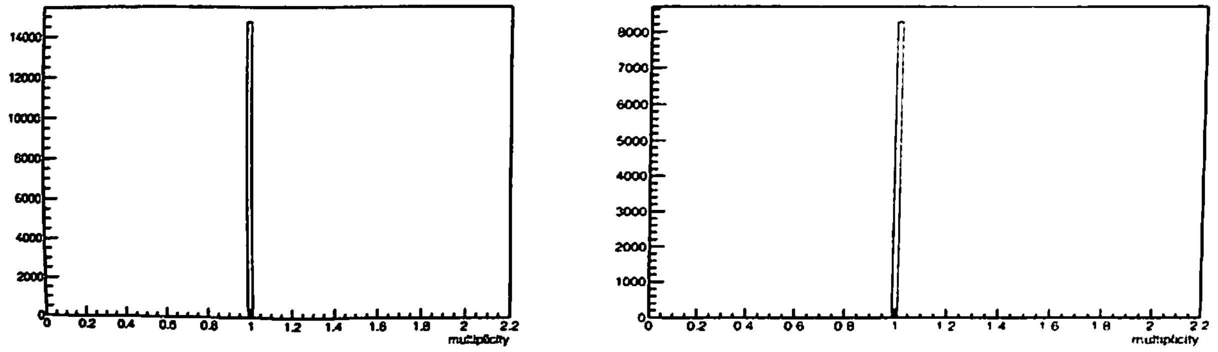

FIGURE 3.40: *Multiplicity for* $B_s^0 \to \eta_{\gamma\gamma}\eta_{\gamma\gamma}$ *(left) and* $B_s^0 \to \eta_{\gamma\gamma}\eta_{3\pi}$ *(right).*

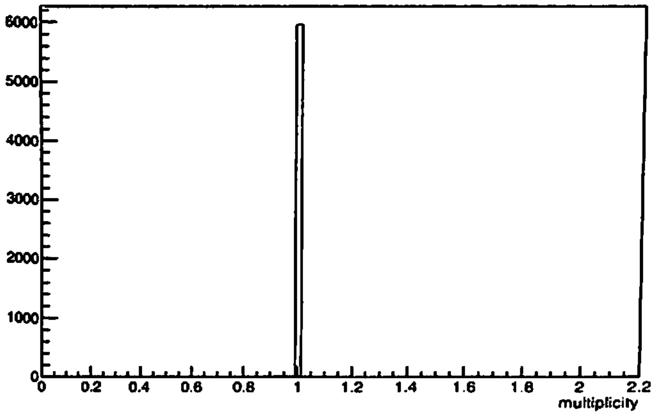

FIGURE 3.41: *Multiplicity for* $B_s^0 \to \eta_{3\pi}\eta_{3\pi}$.

3.6 Signal Selection Efficiency

The signal selection efficiency ϵ and its statistical uncertainty $\Delta\epsilon$ are calculated as:

$$\epsilon = \frac{N_R}{N} \text{ and } \Delta\epsilon = \sqrt{\frac{\epsilon\times(1-\epsilon)}{N}}$$

where N is the total number of signal MC events processed and N_R is the number of signal events left after applying all the selection criteria. We have generated 100,000 signal events for each of the three modes: $B_s^0 \to \eta_{\gamma\gamma}\eta_{\gamma\gamma}$, $B_s^0 \to \eta_{\gamma\gamma}\eta_{3\pi}$ and $B_s^0 \to \eta_{3\pi}\eta_{3\pi}$. After applying the selection criteria, the number of events left are 9621 ,9488 and 8141 for $B_s^0 \to \eta_{\gamma\gamma}\eta_{\gamma\gamma}$, $B_s^0 \to \eta_{\gamma\gamma}\eta_{3\pi}$ and $B_s^0 \to \eta_{3\pi}\eta_{3\pi}$ mode, respectively. Thus the signal selection efficiecny computed to be $(9.62 \pm 0.09)\%$, $(9.48 \pm 0.09)\%$ and $(8.14 \pm 0.08)\%$ for the three modes, respectively.

3.7 Chapter Summary

This chapter describes the analysis strategy, data sets used in the analysis, signal selection and event reconstruction, background MC study, optimization of selection criteria, event multiplicity and best candidate selection criteria. Background MC study shows that the dominating background for the decay $B_s^0 \to \eta\eta$ is $e^+e^- \to q\bar{q}$ continuum events where $q = u, d, s, c$. Contributions from *bsbs* and *nonbsbs* backgrounds are very small. NeuroBayes is used as a NN to suppress the continuum backgrounds. Signal selection efficiency is calculated based on the number of signal events survived all the selection criteria.

Chapter 4

Maximum Likelihood Fit Analysis

This chapter presents a brief introduction to the Maximum Likelihood (ML) fit procedure and the construction of the ML fit PDFs which are used to extract the signal and the background yields in the real data sample. We have performed a 3 dimensional unbinned extended ML fit involving M_{bc}, ΔE and NB' to extract the signal yield.

4.1 Maximum Likelihood (ML) Fit

To estimate the values of various parameters of a distribution, maximum likelihood fit [58–62] method is used. Estimation means a precise and accurate procedure where the result (for e.g., the values of the parameters of a distribution) that may be imprecise, but the extent of imprecision is known [58]. For a data sample $x_1, x_2, x_3, \ldots\ldots, x_n$ of n independent and identically distributed observations, the likelihood $L(\xi|x_1, x_2, x_3, \ldots\ldots, x_n)$ is defined as:

$$L(\xi|x_1, x_2, x_3, \ldots\ldots, x_n) = f(x_1, x_2, x_3, \ldots\ldots, x_n|\xi) = \prod_{i=1}^{n} f(x_i|\xi) \tag{4.1}$$

where ξ denotes the vector of parameters of the unknown distribution. The likelihood function represents the probability of observing the sequence of values $x_1, x_2, x_3, \ldots\ldots, x_n$.

The ML estimator $\hat{\xi_j}$ for a parameter ξ_j, is that value of ξ_j for which the likelihood is maximum which can be found by solving the equation:

$$\frac{dL}{d\xi_j} = 0 \tag{4.2}$$

In practice, it is easier to maximize the logarithm of the likelihood function i.e., to solve the equation:

$$\frac{d(lnL)}{d\xi_j} = 0 \tag{4.3}$$

where

$$lnL(\xi_j|x_1, x_2, x_3, ..., x_n) = \sum_{i=1}^{n} lnf(x_i|\xi_j) \tag{4.4}$$

The solution $\hat{\xi_j}$ is known as the ML estimator for the parameter ξ_j. The value of the estimator $\hat{\xi_j}$ will be different for different samples and will be described by a probability distribution. The error $(\sigma(\hat{\xi_j}))$ on the estimator distribution is given by

$$\sigma^2(\hat{\xi_j}) = \int (\xi_j - \hat{\xi_j})^2 L(\xi_j|x) dx_1 dx_2 .... dx_n \tag{4.5}$$

When more than 1 parameter is involved, the error on the parameters can be expressed as

$$\sigma^2(\hat{\xi_{jk}}) = \int (\xi_j - \hat{\xi_j})(\xi_k - \hat{\xi_k}) L(\xi|x) dx_1 dx_2 .... dx_n \tag{4.6}$$

Here, j and k run over the set of parameters.

In general, the ML estimators are consistent, unbiased and efficient for large samples.

4.2 Extended Maximum Likelihood Fit

In the standard method of ML, the probability or probability density of x , $f(x|\xi)$ is normalized to 1 i.e.,

$$\int f(x|\xi) dx = 1 \tag{4.7}$$

In extendd ML case, this requirement is relaxed. Instead of the function $f(x|\xi)$, a function $g(x|\xi)$ is used for which the normalization is not fixed. Increasing or decreasing $g(x|\xi)$ in some region of x increases or decreases the probability of events occuring in that region and thus increases or decreases the total expected number of events, N, which is given by the total integral of $g(x|\xi)$ i.e.,

$$\int g(x|\xi)dx = N \tag{4.8}$$

This is appropriate in experiments where the number of events is indeed unknown a priori, and in such cases extended ML is an improvement over ML.

The extended ML function L is formed by multiplying the classical likelihood with a Poisson distribution [58]. Thus

$$L(N,\xi) = \frac{e^{-N}N^n}{n!}\prod_{i=1}^{n} f(x_i|\xi) \tag{4.9}$$

When the data sample consists of events of many categories, the extended ML fit can be used to extract the number of events in each category. The likelihood function then can be written as

$$L(N,\xi) = \frac{e^{-\sum_{l=1}^{m} N_l}}{n!}\prod_{i=1}^{n}(\sum_{l=1}^{m} N_l f(x_i|\xi)l) = \frac{e^{-\sum_{l=1}^{m} N_l}}{n!}\prod_{i=1}^{n}(\sum_{l=1}^{m} g(x_i|\xi)l) \tag{4.10}$$

where

$$N = \sum_{i=1}^{n} N_l \tag{4.11}$$

with l running over all possible event categories $(1, 2, ..., m)$, N_l's are the expected number of events of each category and $f(x|\xi)_l$'s are the PDFs for each category evaluated at the l^{th} event. In HEP, the data mostly consists of signal and background events and an extended ML function is used to determine the number of signal and background events through the extended ML fit.

Dropping the constant $n!$ term, the log likelihood of an extended ML function can be written as:

$$lnL = \sum_{i=1}^{n} ln(\sum_{l=1}^{m} g(x_i|\xi)l) - \sum_{l=1}^{m} N_l \tag{4.12}$$

For large statistics cases (i.e., when n is large) the likelihood function is Gaussian and the log likelihood function is a parabola. The parameter uncertainties are symmetric in such cases.

In our analysis, the estimation of the parameters of the PDFs are done in the ROOT framework using RooFit package which minimizes the equivalent function, the negative log likelihood(NLL). The NLL has the form

$$NLL(or - lnL) = \sum_{l=1}^{m} N_l - \sum_{i=1}^{n} ln(\sum_{l=1}^{m} g(x_i|\xi)l) \tag{4.13}$$

There are several algorthims to find the minimum of a function [63 65]. In HEP community, minimization is mostly done through the MIGRAD algorithm [63] of the MINUIT package. The analysis presented in the thesis is done with limited statistics. For such cases the log likelihood function is not a perfect parabola and hence, the parameter uncertainties are asymmetric. The MIGRAD algorithm fails to provide accurate values of such uncertainties. To estimate these asymmetric uncertainties, the MINOS algorithm [63, 66] is used. The MINOS algorithm is usually called after MIGRAD minimization.

Extended ML estimators have a bias for finite n, which vanishes in the large n limit. Unbinned extended ML fit is mostly done when the width of the peak is unknown and when the number of data points n is very large.

4.3 Fit Procdure

We have performed a 3D unbinned extended ML fit with M_{bc}, ΔE and NB' to extract the $B_s^0 \to \eta\eta$ signal yield. The variables used in the fit should not have high correlation among themselves. Before performing the fit, we have checked the correlation among them for all the three decay modes: $B_s^0 \to \eta_{\gamma\gamma}\eta_{\gamma\gamma}$, $B_s^0 \to \eta_{\gamma\gamma}\eta_{3\pi}$ and $B_s^0 \to \eta_{3\pi}\eta_{3\pi}$, the details of which are described below. The background contribution from generic B_s and non$-B_s$ decays are almost zero (Table 3.4) in the signal region for all the three decay modes. Since, these events are very few and they don't have a peaking structure, so they behave like continuum backgrounds. So, they are included in the continuum background PDF.

4.3.1 Results of correlation study

We have studied the correlation among the fit variables M_{bc}, ΔE and NB' for all the three decay modes: $B_s^0 \to \eta_{\gamma\gamma}\eta_{\gamma\gamma}$, $B_s^0 \to \eta_{\gamma\gamma}\eta_{3\pi}$ and $B_s^0 \to \eta_{3\pi}\eta_{3\pi}$. Figure 4.1, 4.2, 4.3, 4.4, 4.5 and 4.6 show the results of correlation studies and Table 4.1, 4.2 and 4.3 show the values of correlation factors among the fit variables, for all the three decay modes, respectively. From these studies we have not seen any strong correlation among the fit variables.

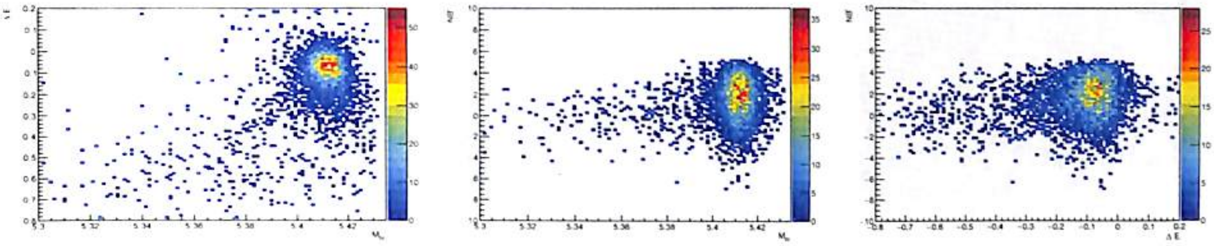

FIGURE 4.1: *Correlation between M_{bc} and ΔE and NB' for signal for $B_s^0 \to \eta_{\gamma\gamma}\eta_{\gamma\gamma}$.*

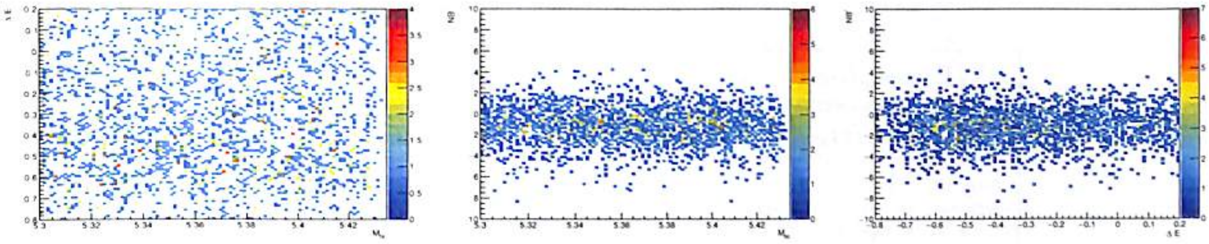

FIGURE 4.2: *Correlation between M_{bc} and ΔE and NB' for background for $B_s^0 \to \eta_{\gamma\gamma}\eta_{\gamma\gamma}$.*

Fit variables	$M_{bc} vs \Delta E$	$M_{bc} vs NB'$	$\Delta E vs NB'$
Signal MC(true)	-0.0185148	0.0302077	0.059723
Signal MC(SCF)	0.0888034	0.256729	0.108512
Continuum	0.0481498	-0.0523439	0.0469857

TABLE 4.1: *Linear correlation factors between the fit variables in $B_s^0 \to \eta_{\gamma\gamma}\eta_{\gamma\gamma}$ mode.*

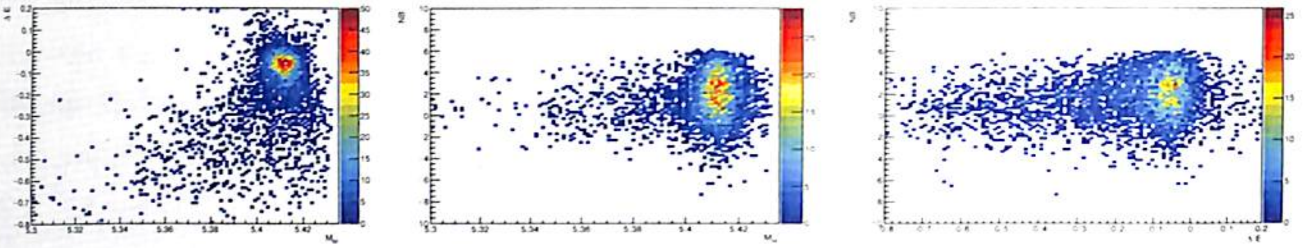

FIGURE 4.3: *Correlation between M_{bc} and ΔE and NB' for signal for $B_s^0 \to \eta_{\gamma\gamma}\eta_{3\pi}$.*

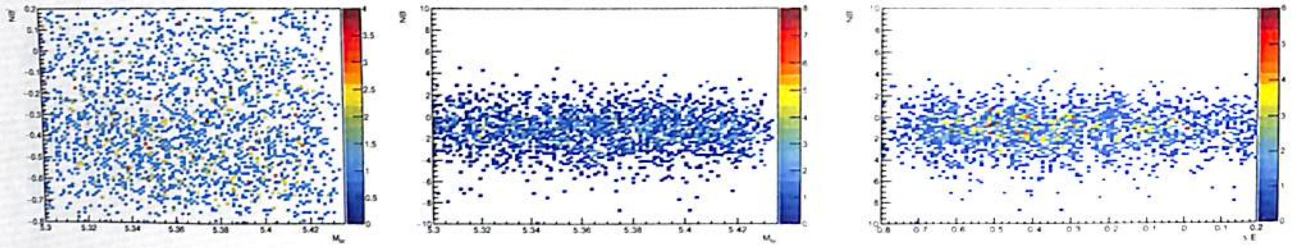

FIGURE 4.4: *Correlation between M_{bc} and ΔE and NB' for background for $B_s^0 \to \eta_{\gamma\gamma}\eta_{3\pi}$*

Fit variables	$M_{bc} vs \Delta E$	$M_{bc} vs NB'$	$\Delta E vs NB'$
Signal MC(true)	0.190619	0.133216	0.079158
Signal MC(SCF)	0.210762	0.213054	0.099781
Continuum	0.0492919	-0.0330407	0.0154495

TABLE 4.2: ***Linear correlation factors between the fit variables in** $B_s^0 \to \eta_{\gamma\gamma}\eta_{3\pi}$ mode.*

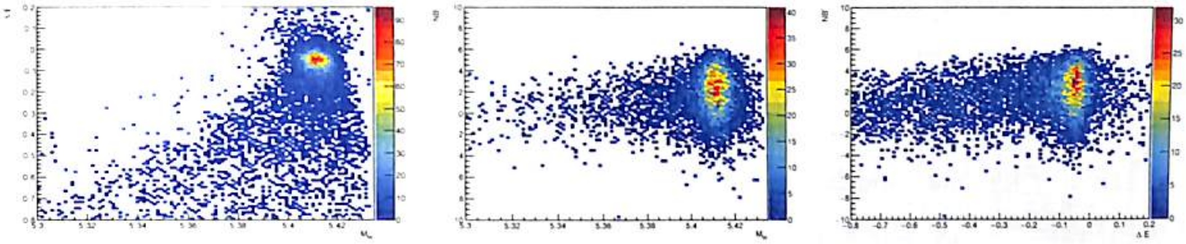

FIGURE 4.5: *Correlation between M_{bc} and ΔE and NB' for signal for $B_s^0 \to \eta_{3\pi}\eta_{3\pi}$.*

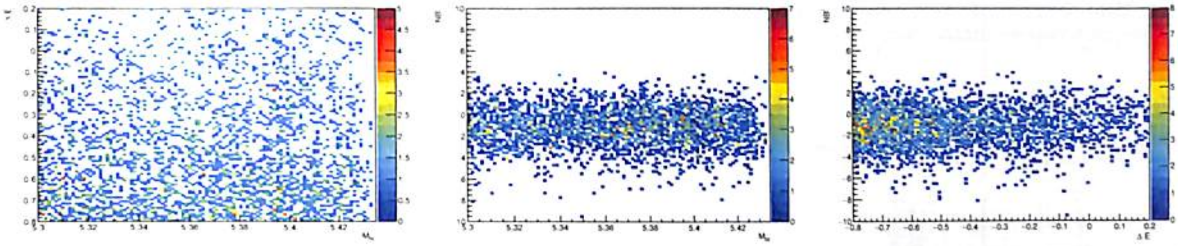

FIGURE 4.6: *Correlation between M_{bc} and ΔE and NB' for background for $B_s^0 \to \eta_{3\pi}\eta_{3\pi}$*

Fit variables	$M_{bc} vs \Delta E$	$M_{bc} vs NB'$	$\Delta E vs NB'$
Signal MC(true)	0.268571	0.175594	0.0841608
Signal MC(SCF)	0.141682	0.0835296	0.13553
Continuum	0.0436491	-0.0185844	0.0821277

TABLE 4.3: ***Linear correlation factors between the fit variables in** $B_s^0 \to \eta_{3\pi}\eta_{3\pi}$ **mode.***

4.4 Signal and Background PDFs

4.4.1 Signal PDF

Signal MC samples are used to parameterize the signal PDFs. The M_{bc} distribution for true signal is parameterized with Crystal Ball (CBall) function, the ΔE distribution for true signal is parameterized with (Crystal Ball + Gaussian) function and the NB' distribution for true signal is parameterized with double Gaussian function for all the three decay modes: $B_s^0 \to \eta_{\gamma\gamma}\eta_{\gamma\gamma}$, $B_s^0 \to \eta_{\gamma\gamma}\eta_{3\pi}$ and $B_s^0 \to \eta_{3\pi}\eta_{3\pi}$. The M_{bc} distribution for mis reconstructed signal is parameterized with Crystal Ball (CBall) function and the NB' distribution for mis-reconstructed signal is parameterized with double Gaussian function for all the three decay modes. The ΔE distributions for mis-reconstructed signal of $B_s^0 \to \eta_{\gamma\gamma}\eta_{\gamma\gamma}$ and $B_s^0 \to \eta_{\gamma\gamma}\eta_{3\pi}$

are parameterized with (Gaussian + Chebychev Polynomial). The ΔE distributions for mis-reconstructed signal of $B_s^0 \to \eta_{3\pi}\eta_{3\pi}$ is parameterized with Chebychev Polynomial. (Details of the PDFs are described in Appendix A).

The fit functions and fit parameters for signal MC are summarized in Table 4.4, 4.5, 4.6 and the plots are shown in Figure 4.7, 4.8, 4.9, 4.10,4.11, 4.12, 4.13, 4.14, 4.15

Variable	Function	Paramter	Value	Comment
M_{bc}(true)	Crystal Ball	mean (μ)	$5.412385 \pm 0.000077 GeV/c^2$	floated
		sigma (σ)	$0.004535 \pm 0.000061 GeV/c^2$	floated
		n	7.4 ± 2.0	floated
		alpha (α)	1.558 ± 0.098	floated
M_{bc}(mis recon.)	Crystal Ball	mean (μ)	$5.4129 \pm 0.0010 GeV/c^2$	floated
		sigma (σ)	$0.00975 \pm 0.00085 GeV/c^2$	floated
		n	9.4 ± 8.1	floated
		alpha (α)	0.453 ± 0.084	floated
ΔE (true)	(Crystal Ball + Gaussian)	mean (μ_1)	-0.1019 ± 0.014	floated
		sigma1 (σ_1)	0.0662 ± 0.0074	floated
		n	5.00 ± 0.21	floated
		alpha (α)	1.30 ± 0.10	floated
		mean (μ_2)	-0.05639 ± 0.0053	floated
		sigma2 (σ_2)	0.0360 ± 0.0048	floated
		fraction (f)	0.58 ± 0.15	floated
ΔE (mis recon.)	(Gaussian + Chebychev)	mean (μ)	-0.1358 ± 0.014	floated
		sigma (σ)	0.108 ± 0.014	floated
		Coefficient (c_0)	-0.601 ± 0.10	floated
		fraction (f)	0.334 ± 0.052	floated
NB' (true)	Double Gaussian	mean (μ_1)	0.62 ± 0.12	floated
		sigma1 (σ_1)	1.733 ± 0.039	floated
		mean (μ_2)	2.629 ± 0.073	floated
		sigma2 (σ_2)	1.086 ± 0.042	floated
		fraction (f)	0.486 ± 0.043	floated
NB' (mis recon.)	Double Gaussian	mean (μ_1)	0.25 ± 0.31	floated
		sigma1 (σ_1)	1.60 ± 0.11	floated
		mean (μ_2)	2.34 ± 0.27	floated
		sigma2 (σ_2)	1.02 ± 0.15	floated
		fraction (f)	0.67 ± 0.13	floated

TABLE 4.4: *signal MC parameterizations for* $B_s^0 \to \eta_{\gamma\gamma}\eta_{\gamma\gamma}$ *mode.*

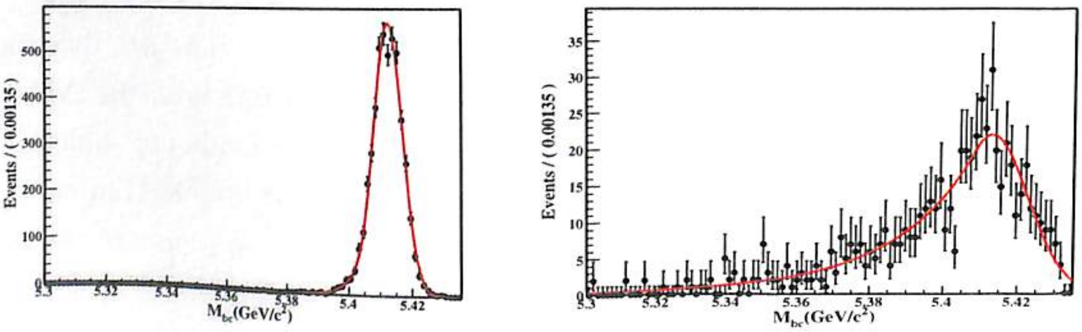

FIGURE 4.7: $B_s^0 \to \eta_{\gamma\gamma}\eta_{\gamma\gamma}$ *signal MC* M_{bc} *parameterizations for true(left) and mis-reconstructed(right) events.*

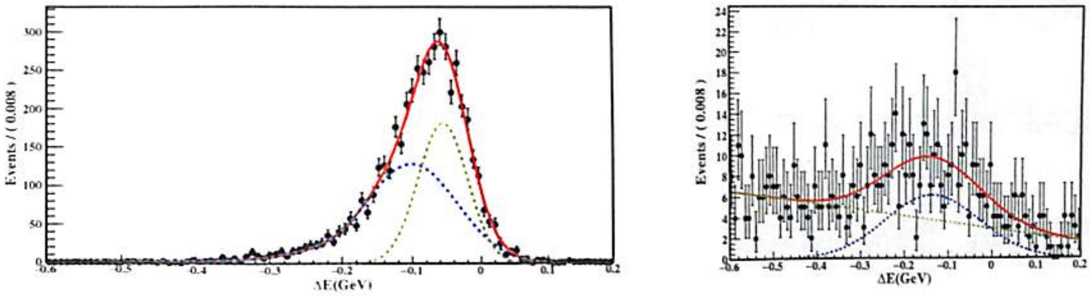

FIGURE 4.8: $B_s^0 \to \eta_{\gamma\gamma}\eta_{\gamma\gamma}$ *signal MC* ΔE *parameterizations for true(left) and mis-reconstructed(right) events.*

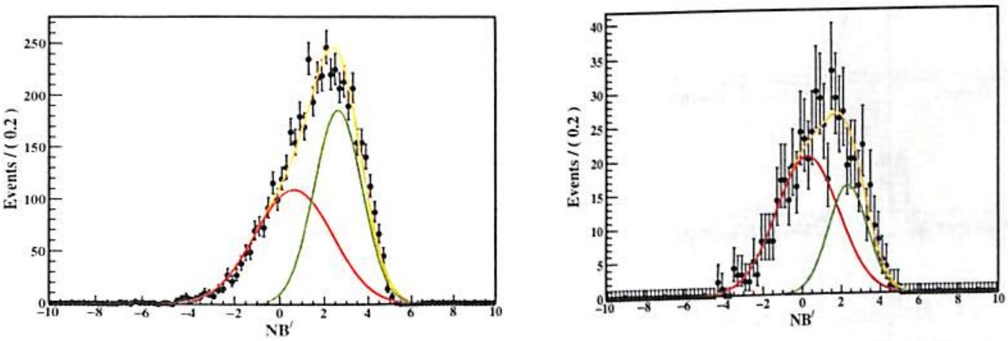

FIGURE 4.9: $B_s^0 \to \eta_{\gamma\gamma}\eta_{\gamma\gamma}$ *signal MC* NB' *parameterizations for true(left) and mis-reconstructed(right) events.*

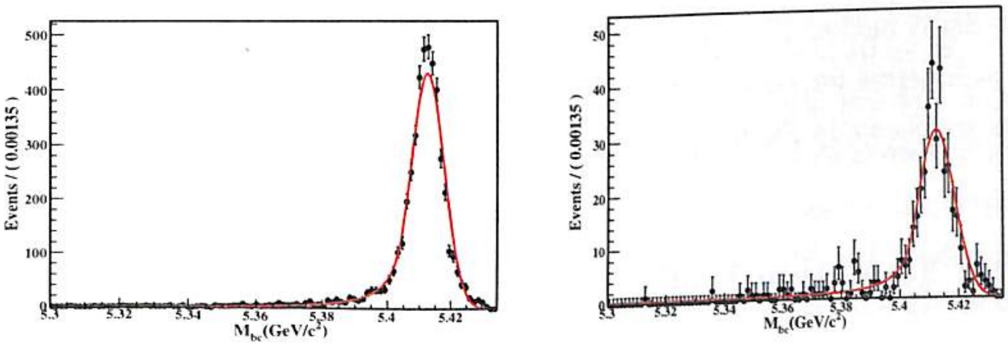

FIGURE 4.10: $B_s^0 \to \eta_{\gamma\gamma}\eta_{3\pi}$ *signal MC* M_{bc} *parameterizations for true(left) and mis-reconstructed(right) events.*

4.4.2 Background PDFs

For background MC, the M_{bc} distribution is parameterized with an Argus function with fixed endpoint, the ΔE distribution is parameterized with a second order Chebychev Polynomial and NB' is parameterized with a Gaussian function for all

Variable	Function	Paramter	Value	Comment
M_{bc}(true)	Crystal Ball	mean (μ)	$5.412472 \pm 0.000095 GeV/c^2$	floated
		sigma (σ)	$0.005314 \pm 0.000075 GeV/c^2$	floated
		n	2.04 ± 0.15	floated
		alpha (α)	1.446 ± 0.055	floated
M_{bc}(mis recon.)	Crystal Ball	mean (μ)	$5.41259 \pm 0.00038 GeV/c^2$	floated
		sigma (σ)	$0.00614 \pm 0.00030 GeV/c^2$	floated
		n	1.31 ± 0.32	floated
		alpha (α)	1.42 ± 0.18	floated
ΔE (true)	(Crystal Ball + Gaussian)	mean (μ_1)	-0.11994 ± 0.0072	floated
		sigma1 (σ_1)	0.1046 ± 0.0052	floated
		n	1.22 ± 0.38	floated
		alpha (α)	0.95 ± 0.11	floated
		mean (μ_2)	-0.05696 ± 0.0012	floated
		sigma2 (σ_2)	0.0327 ± 0.0014	floated
		fraction (f)	0.552 ± 0.025	floated
ΔE (mis recon.)	(Gaussian + Chebychev)	mean (μ_1)	0.4000 ± 0.012	floated
		sigma (σ_1)	0.319 ± 0.036	floated
		mean (μ_2)	-0.06141 ± 0.0034	floated
		sigma (σ_2)	0.0408 ± 0.0032	floated
		fraction (f)	0.442 ± 0.033	floated
NB' (true)	Double Gaussian	mean (μ_1)	1.08 ± 0.13	floated
		sigma1 (σ_1)	1.885 ± 0.039	floated
		mean (μ_2)	3.29 ± 0.15	floated
		sigma2 (σ_2)	1.224 ± 0.080	floated
		fraction (f)	0.679 ± 0.058	floated
NB' (mis recon.)	Double Gaussian	mean (μ_1)	1.01 ± 0.30	floated
		sigma1 (σ_1)	1.78 ± 0.14	floated
		mean (μ_2)	3.00 ± 0.61	floated
		sigma2 (σ_2)	1.21 ± 0.17	floated
		fraction (f)	0.68 ± 0.11	floated

TABLE 4.5: *signal MC parameterizations for $B_s^0 \to \eta_{\gamma\gamma}\eta_{3\pi}$ mode.*

the three decay modes: $B_s^0 \to \eta_{\gamma\gamma}\eta_{\gamma\gamma}$, $B_s^0 \to \eta_{\gamma\gamma}\eta_{3\pi}$ and $B_s^0 \to \eta_{3\pi}\eta_{3\pi}$. The functions and fit parameters for background MC are summarized in Table 4.7, 4.8, 4.9 and the plots are shown in Figure 4.16, 4.18, 4.20, 4.19, 4.21.

4.5 Fit Validation Using Toy MC

To validate the fit procedure, we have performed Toy MC study. Pure toy events are generated according to our fit PDFs by fixing all signal and background parameters. We generate 3000 such events for all the three cases: $B_s^0 \to \eta_{\gamma\gamma}\eta_{\gamma\gamma}$, $B_s^0 \to \eta_{\gamma\gamma}\eta_{3\pi}$ and $B_s^0 \to \eta_{3\pi}\eta_{3\pi}$. For different values of signal yield, we obtain the return pull and fit yield distributions. The pull is defined as: Pull = (Fit Yield - Actual Yield). We then fit the signal pull mean with a linear polynomial to check the stability of the fitter. The results of Toy MC study for all the three cases are described bellow.

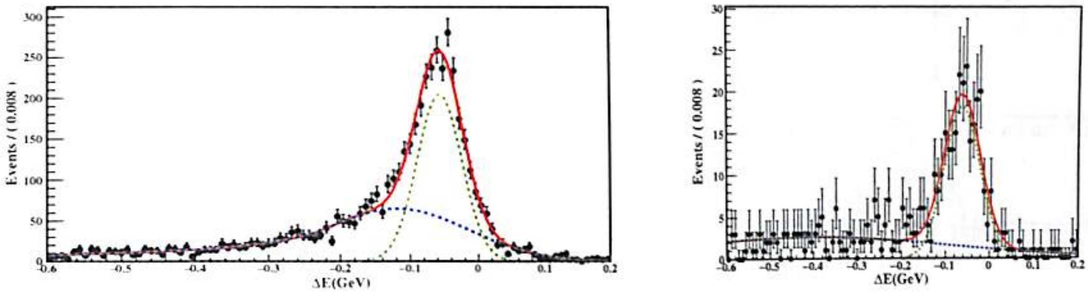

FIGURE 4.11: $B_s^0 \rightarrow \eta_{\gamma\gamma}\eta_{3\pi}$ *signal MC* ΔE *parameterizations for true(left) and mis-reconstructed(right) events.*

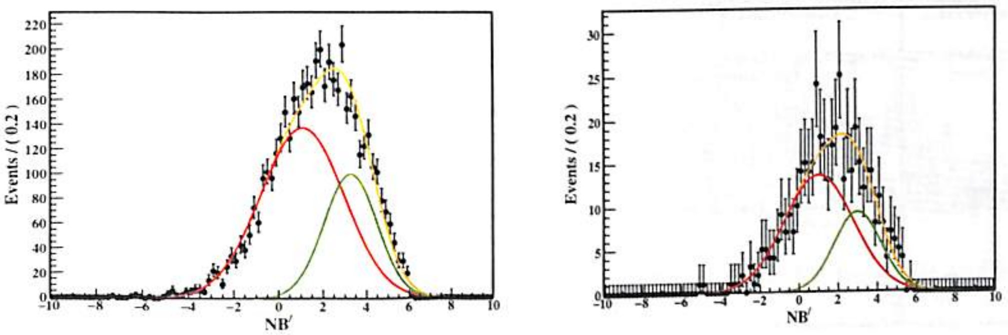

FIGURE 4.12: $B_s^0 \rightarrow \eta_{\gamma\gamma}\eta_{3\pi}$ *signal MC* NB' *parameterizations for true(left) and mis-reconstructed(right) events.*

4.5.1 Toy results

Figure 4.22, 4.23 and 4.24 show Toy MC results for signal yield 10 for $B_s^0 \rightarrow \eta_{\gamma\gamma}\eta_{\gamma\gamma}$, $B_s^0 \rightarrow \eta_{\gamma\gamma}\eta_{3\pi}$ and $B_s^0 \rightarrow \eta_{3\pi}\eta_{3\pi}$ modes, respectively. Such Toy MC studies are performed for different signal yields and Figure 4.25 and 4.26 show the results of linearity test for $B_s^0 \rightarrow \eta_{\gamma\gamma}\eta_{\gamma\gamma}$, $B_s^0 \rightarrow \eta_{\gamma\gamma}\eta_{3\pi}$ and $B_s^0 \rightarrow \eta_{3\pi}\eta_{3\pi}$ modes, respectively. From this studies we find that fit is biased by about 4%, 10% and 6% for the three modes, respectively, which may be considered as a source of systematic uncertainty.

Variable	Function	Paramter	Value	Comment
M_{bc}(true)	Crystal Ball	mean (μ)	$5.412426 \pm 0.000060 GeV/c^2$	floated
		sigma (σ)	$0.005383 \pm 0.000063 GeV/c^2$	floated
		n	1.97 ± 0.11	floated
		alpha (α)	1.370 ± 0.043	floated
M_{bc}(mis recon.)	Crystal Ball	mean (μ)	$5.4153 \pm 0.0022 GeV/c^2$	floated
		sigma (σ)	$0.0080 \pm 0.0016 GeV/c^2$	floated
		n	5.4 ± 3.6	floated
		alpha (α)	0.50 ± 0.19	floated
ΔE (true)	(Crystal Ball + Gaussian)	mean (μ_1)	-0.10925 ± 0.0057	floated
		sigma1 (σ_1)	0.1036 ± 0.0043	floated
		n	0.59 ± 0.15	floated
		alpha (α)	0.834 ± 0.094	floated
		mean (μ_2)	-0.049697 ± 0.00070	floated
		sigma2 (σ_2)	0.02643 ± 0.00081	floated
		fraction (f)	0.834 ± 0.094	floated
ΔE (mis recon.)	Chebychev Poly.	**Coefficient** (c_0)	-0.8098 ± 0.070	floated
		Coefficient (c_1)	-0.1624 ± 0.076	floated
NB' (true)	Double Gaussian	mean (μ_1)	0.84 ± 0.13	floated
		sigma1 (σ_1)	1.903 ± 0.039	floated
		mean (μ_2)	2.905 ± 0.097	floated
		sigma2 (σ_2)	1.283 ± 0.052	floated
		fraction (f)	0.497 ± 0.051	floated
NB' (mis recon.)	Double Gaussian	mean (μ_1)	0.45 ± 0.30	floated
		sigma1 (σ_1)	1.72 ± 0.12	floated
		mean (μ_2)	2.83 ± 0.48	floated
		sigma2 (σ_2)	1.01 ± 0.27	floated
		fraction (f)	0.84 ± 0.13	floated

TABLE 4.6: *signal MC parameterizations for $B_s^0 \to \eta_{3\pi}\eta_{3\pi}$ mode.*

Variable	Function	Paramter	Value	Comment
M_{bc}	Argus	Curvature (a_1)	-22.10 ± 1.6	floated
		Endpoint a_0	5.435	fixed
ΔE	Chebychev Poly.	**Coefficint** (c_0)	-0.4090 ± 0.037	floated
		Coefficint (c_1)	0.084 ± 0.035	floated
NB'	Gaussian	Mean (μ)	-1.1294 ± 0.039	floated
		Sigma (σ)	1.729 ± 0.027	floated

TABLE 4.7: *Background MC parameterizations for $B_s^0 \to \eta_{\gamma\gamma}\eta_{\gamma\gamma}$ mode.*

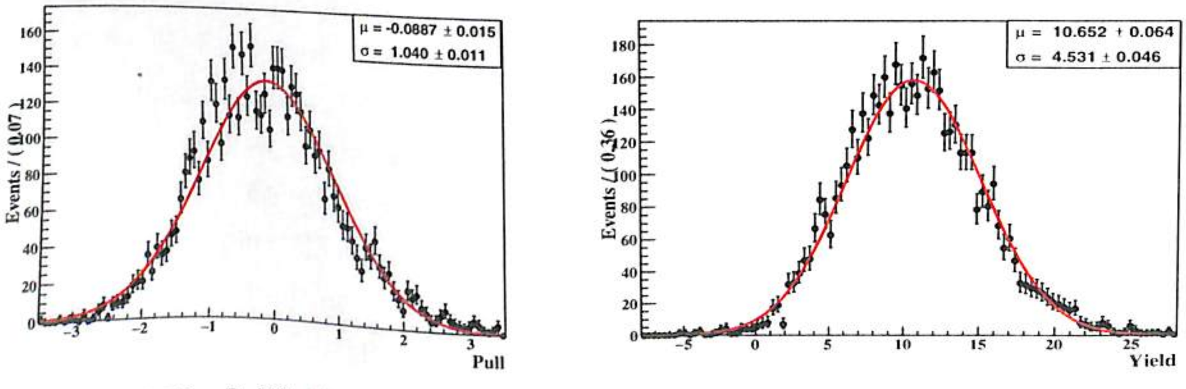

FIGURE 4.22: *Pull(left) and signal yield(right) parameterizations for nsig=10, for$B_s^0 \to \eta_{\gamma\gamma}\eta_{\gamma\gamma}$ mode.*

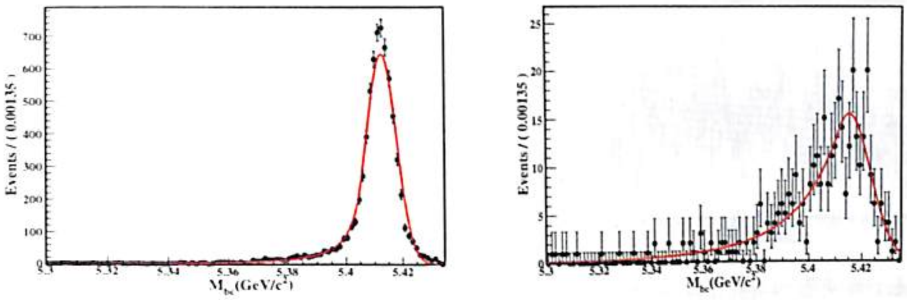

FIGURE 4.13: $B_s^0 \to \eta_{3\pi}\eta_{3\pi}$ *signal MC* M_{bc} *parameterizations for true(left) and mis-reconstructed(right) events.*

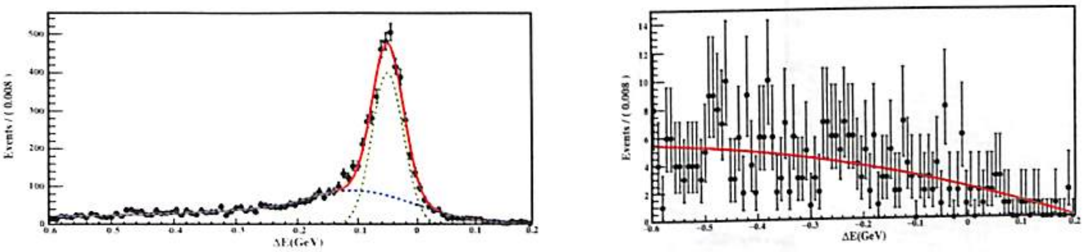

FIGURE 4.14: $B_s^0 \to \eta_{3\pi}\eta_{3\pi}$ *signal MC* ΔE *parameterizations for true(left) and mis-reconstructed(right) events.*

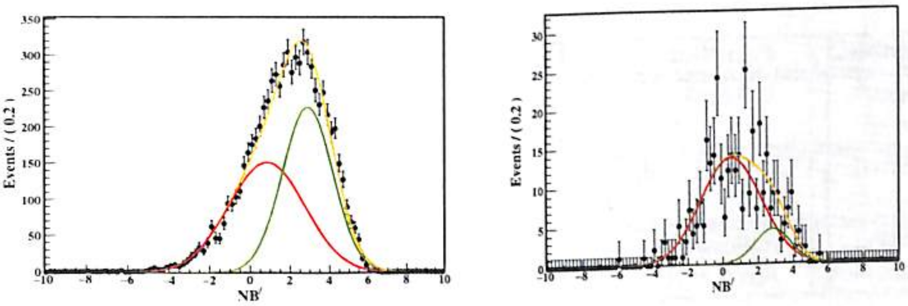

FIGURE 4.15: $B_s^0 \to \eta_{3\pi}\eta_{3\pi}$ *signal MC* NB' *parameterizations for true(left) and mis-reconstructed(right) events.*

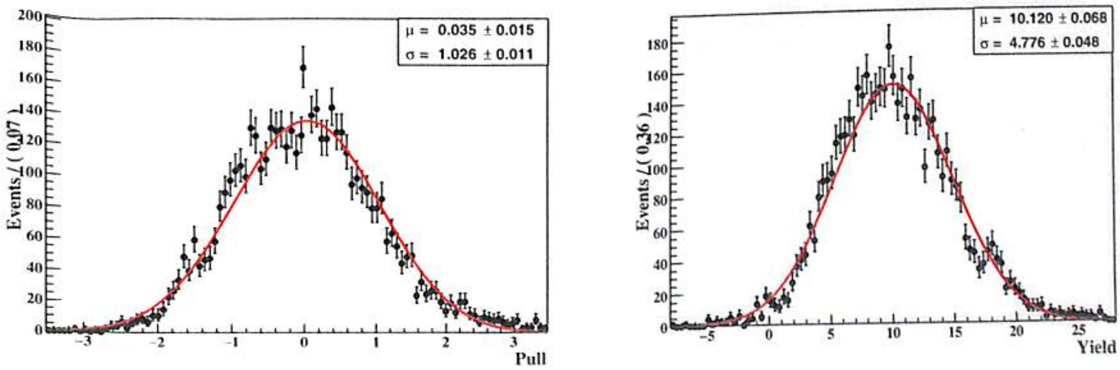

FIGURE 4.23: *Pull(left) and signal yield(right) parameterizations for nsig=10, for*$B_s^0 \to \eta_{\gamma\gamma}\eta_{3\pi}$ *mode.*

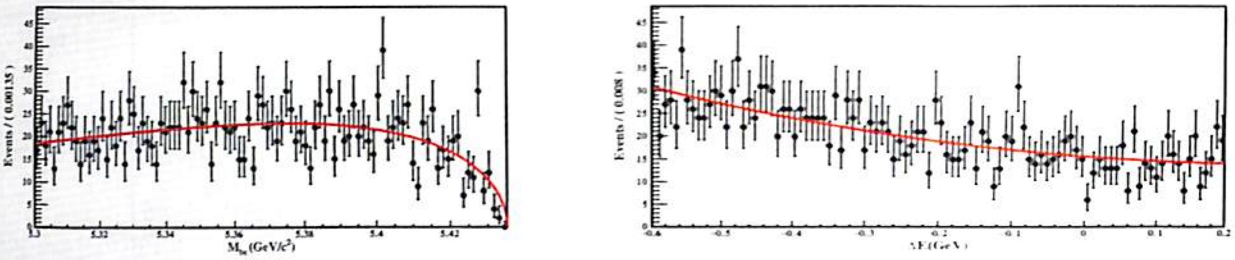

FIGURE 4.16: $B_s^0 \to \eta_{\gamma\gamma}\eta_{\gamma\gamma}$ *background MC* M_{bc} *(left) and* ΔE *(right) parameterizations.*

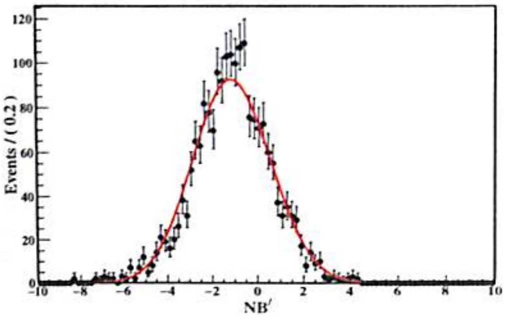

FIGURE 4.17: *Background MC* NB' *parameterizations for* $B_s^0 \to \eta_{\gamma\gamma}\eta_{\gamma\gamma}$ *(left) and* $B_s^0 \to \eta_{\gamma\gamma}\eta_{3\pi}$ *(right).*

Variable	Function	Paramter	Value	Comment
M_{bc}	Argus	Curvature (a_1) Endpoint a_0	-24.95 ± 1.6 5.435	floated fixed
ΔE	Chebychev Poly.	Coefficint (c_0) Coefficint (c_1)	-0.5055 ± 0.036 -0.0703 ± 0.038	floated floated
NB'	Gaussian	Mean (μ) Sigma (σ)	-1.2170 ± 0.036 1.751 ± 0.026	floated floated

TABLE 4.8: Background MC parameterizations for $B_s^0 \to \eta_{\gamma\gamma}\eta_{3\pi}$ mode.

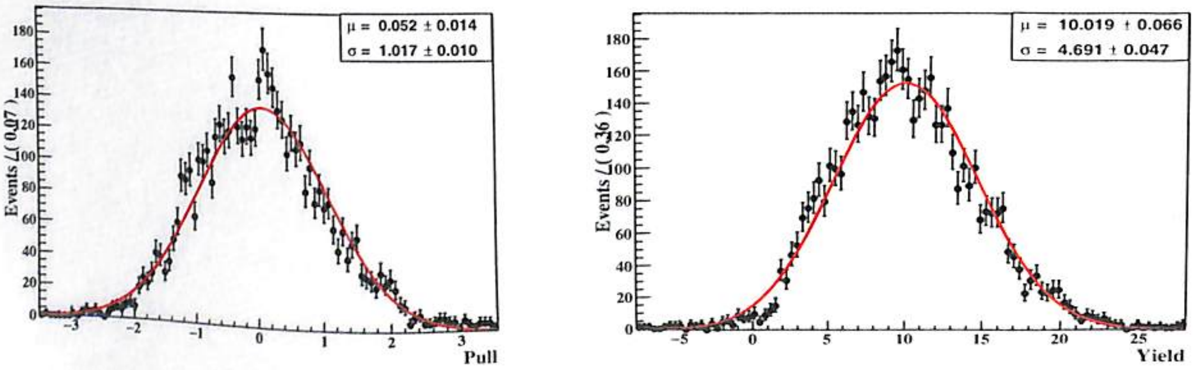

FIGURE 4.24: *Pull(left) and signal yield(right) parameterizations for nsig=10, for*$B_s^0 \to \eta_{3\pi}\eta_{3\pi}$ *mode.*

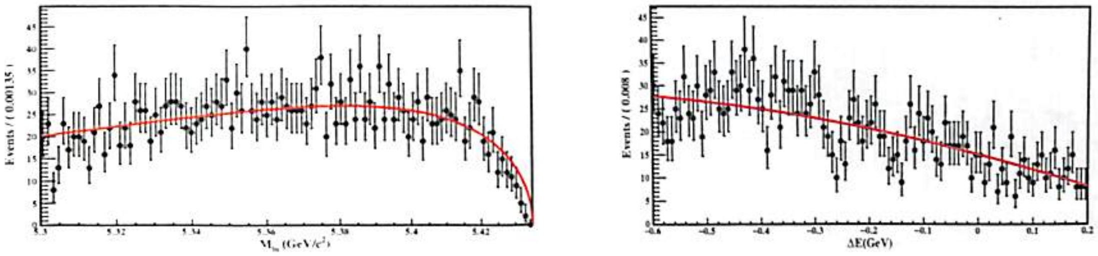

FIGURE 4.18: *$B_s^0 \to \eta_{\gamma\gamma}\eta_{3\pi}$ background MC M_{bc} (left) and ΔE(right) parameterizations.*

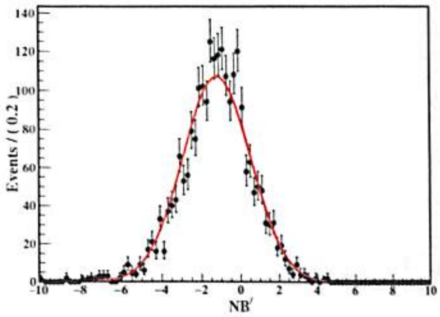

FIGURE 4.19: *Background MC NB' parameterizations for $B_s^0 \to \eta_{\gamma\gamma}\eta_{\gamma\gamma}$(left) and $B_s^0 \to \eta_{\gamma\gamma}\eta_{3\pi}$(right).*

Variable	Function	Paramter	Value	Comment
M_{bc}	Argus	Curvature (a_1) Endpoint a_0	-26.66 ± 1.3 5.435	floated fixed
ΔE	Chebychev Poly.	Coefficint (c_0) Coefficint (c_1)	-0.7793 ± 0.032 0.110 ± 0.033	floated floated
NB'	Gaussian	Mean (μ) Sigma (σ)	-1.1490 ± 0.039 1.727 ± 0.028	floated floated

TABLE 4.9: *Background MC parameterizations for $B_s^0 \to \eta_{3\pi}\eta_{3\pi}$ mode.*

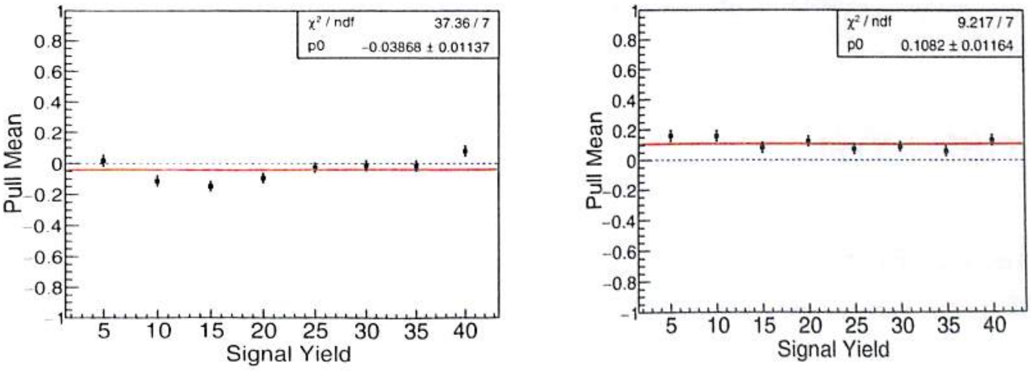

FIGURE 4.25: *Result of linearity test for $B_s^0 \to \eta_{\gamma\gamma}\eta_{\gamma\gamma}$ (left) and $B_s^0 \to \eta_{\gamma\gamma}\eta_{3\pi}$ (right).*

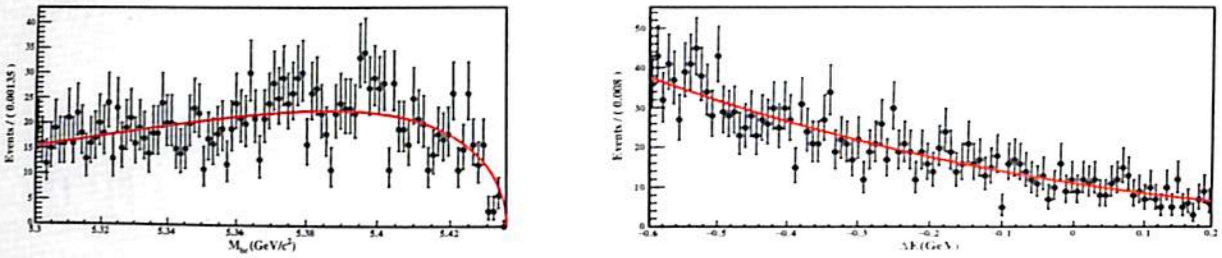

FIGURE 4.20: *$B_s^0 \to \eta_{3\pi}\eta_{3\pi}$ background MC M_{bc} (left) and ΔE (right) parameterizations.*

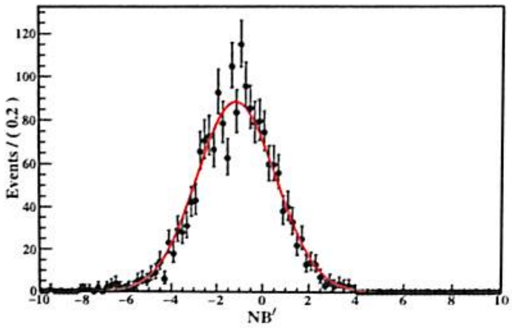

FIGURE 4.21: *Background MC NB' parameterization for $B_s^0 \to \eta_{3\pi}\eta_{3\pi}$.*

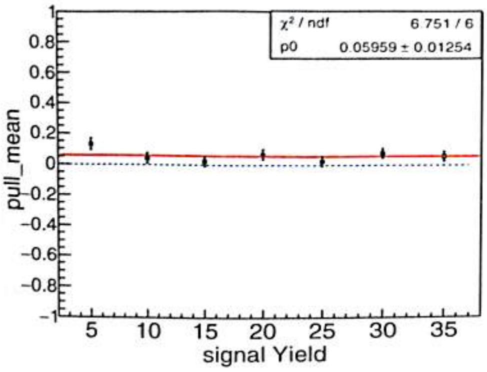

FIGURE 4.26: *Result of linearity test for $B_s^0 \to \eta_{3\pi}\eta_{3\pi}$*

4.6 GSIM Test

To get more realistic idea about possible bias in the fitting strategy, we also perform a GSIM test. GSIM MC samples, generated using EvtGen and passed through GEANT for simulating detector response are used instead of Toy MC samples. We generate 3000 such events for all the three cases: $B_s^0 \to \eta_{\gamma\gamma}\eta_{\gamma\gamma}$, $B_s^0 \to \eta_{\gamma\gamma}\eta_{3\pi}$ and $B_s^0 \to \eta_{3\pi}\eta_{3\pi}$. The events are picked up independently and randomly according to

Poisson distribution from GSIM MC samples. The results of GSIM test for all the three cases are described below. For different values of signal yield, we obtain the return pull and fit yield distributions. The pull is defined as: Pull = Fit Yield - Actual Yield. We then fit the signal pull mean with a linear polynomial to check the stability of the fitter.

4.6.1 GSIM test results

Figure 4.27, 4.28 and 4.29 show GSIM test results for signal yield 20 for $B_s^0 \to \eta_{\gamma\gamma}\eta_{\gamma\gamma}$, $B_s^0 \to \eta_{\gamma\gamma}\eta_{3\pi}$ and $B_s^0 \to \eta_{3\pi}\eta_{3\pi}$ modes, respectively. Such GSIM tests are performed for different signal yields and 4.30 and 4.31 show the results of GSIM linearity test for $B_s^0 \to \eta_{\gamma\gamma}\eta_{\gamma\gamma}$, $B_s^0 \to \eta_{\gamma\gamma}\eta_{3\pi}$ and $B_s^0 \to \eta_{3\pi}\eta_{3\pi}$ modes, respectively. From our studies we find that fit is biased by about 6%, 5% and 9% for the three modes, respectively. Since the GSIM test is a better test to understand the stability of the fit, we plan to use these fit bias values as a source of systematic uncertainty.

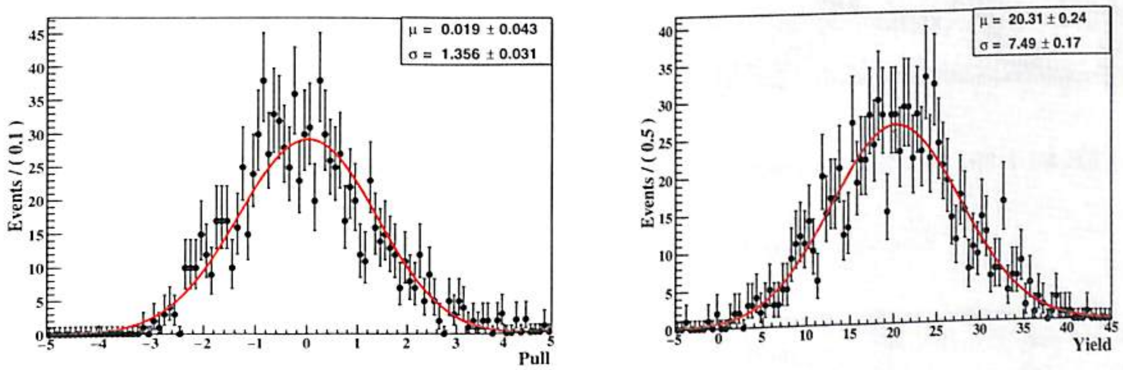

FIGURE 4.27: *Pull(left) and signal yield(right) parameterizations for nsig=20, for* $B_s^0 \to \eta_{\gamma\gamma}\eta_{\gamma\gamma}$ *mode.*

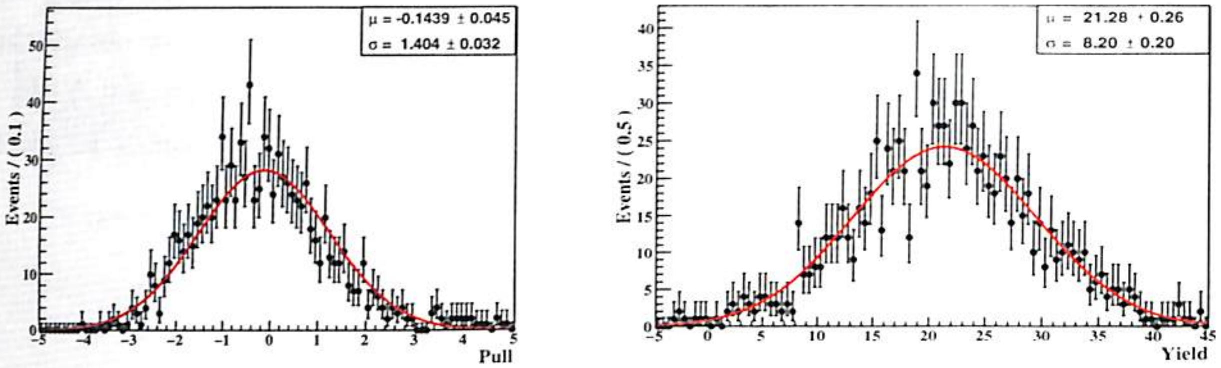

FIGURE 4.28: *Pull(left) and signal yield(right) parameterizations for nsig=20. for* $B_s^0 \rightarrow \eta_{\gamma\gamma}\eta_{3\pi}$ *mode.*

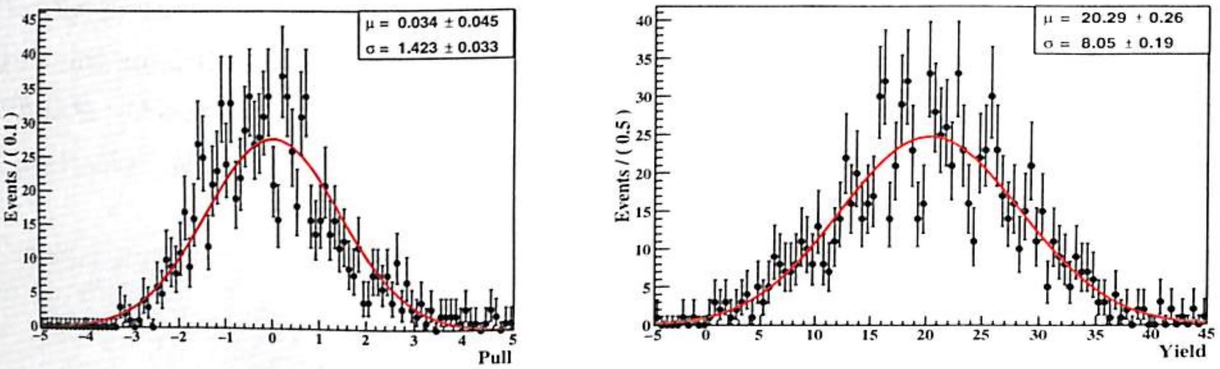

FIGURE 4.29: *Pull(left) and signal yield(right) parameterizations for nsig=20. for* $B_s^0 \rightarrow \eta_{3\pi}\eta_{3\pi}$ *mode.*

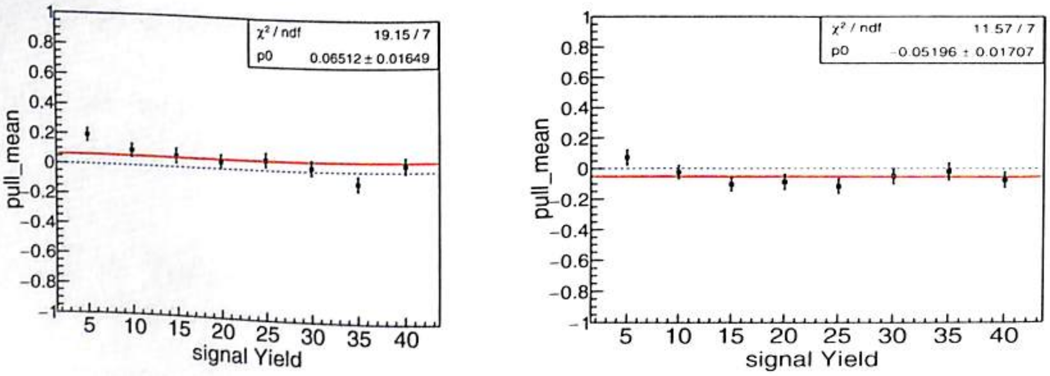

FIGURE 4.30: *Result of GSIM linearity test for* $B_s^0 \rightarrow \eta_{\gamma\gamma}\eta_{\gamma\gamma}$ *(left) and for* $B_s^0 \rightarrow \eta_{\gamma\gamma}\eta_{3\pi}$ *(right).*

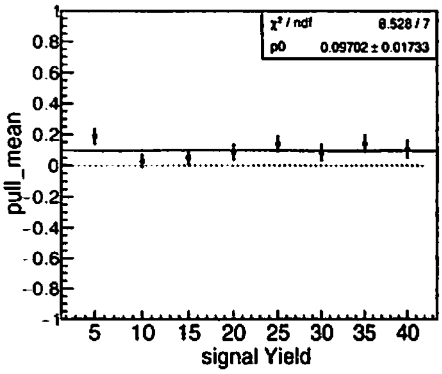

FIGURE 4.31: *Result of GSIM linearity test for* $B_s^0 \to \eta_{3\pi}\eta_{3\pi}$.

4.7 Real Data fit PDF

From the Toy MC study and GSIM test, the fitter seems to be stable. The total PDF for both signal and background is constructed by taking the product of individual 1D PDFs. Then the final PDF is formed by adding the signal and background PDFs. All the signal parameters are kept fixed to the MC values. All background parameters except the Argus endpoint are floated. The signal and background yields are also floated.

4.7.1 Fit Results for $121.4 fb^{-1}$ real data sample

The $\Upsilon(5S)$ dataset is unblinded with this fit strategy to extract the signal and background yields. Figure 4.32, 4.33 and 4.34 show the real data fits for $B_s^0 \to \eta_{\gamma\gamma}\eta_{\gamma\gamma}$, $B_s^0 \to \eta_{\gamma\gamma}\eta_{3\pi}$ and $B_s^0 \to \eta_{3\pi}\eta_{3\pi}$ mode, respectively. The fit yields (3.9±3.2), (7.7±4.4) and (0.2±5.9) signal events and (882 ± 30), (797 ± 28) and (1244 ± 36) background events for the three modes, respectively. Table4.10 presents the summary of the real data fit results.

Sub Decay mode	$B_s^0 \to \eta_{\gamma\gamma}\eta_{\gamma\gamma}$	$B_s^0 \to \eta_{\gamma\gamma}\eta_{3\pi}$	$B_s^0 \to \eta_{3\pi}\eta_{3\pi}$
Signal Yield(n_{sig})	3.9±3.2	7.7±4.4	0.2±5.9
Background Yield	882 ± 30	797 ± 28	1244 ± 36

TABLE 4.10: *Summary of the real data fit.*

The expected number of Signal and Background events from MC study are presented in Table 4.11.

Sub Decay mode	$B_s^0 \to \eta_{\gamma\gamma}\eta_{\gamma\gamma}$	$B_s^0 \to \eta_{\gamma\gamma}\eta_{3\pi}$	$B_s^0 \to \eta_{3\pi}\eta_{3\pi}$
Expected no. of signal	2.7	1.62	0.82
Expected no. of background	985	909	1132

TABLE 4.11: *Summary of the MC data fit.*

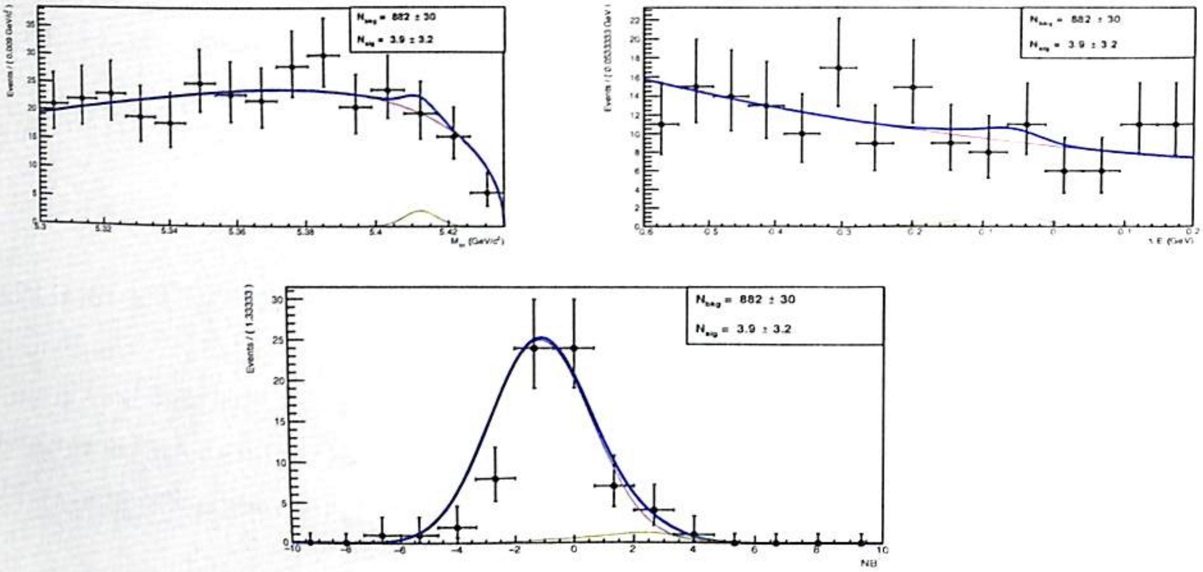

FIGURE 4.32: *Real Data Fit Results for $B_s^0 \to \eta_{\gamma\gamma}\eta_{\gamma\gamma}$ mode. The points with the error bars are the real data points and the blue, purple and green lines represent the total PDF, signal PDF and background PDF, respectively.*

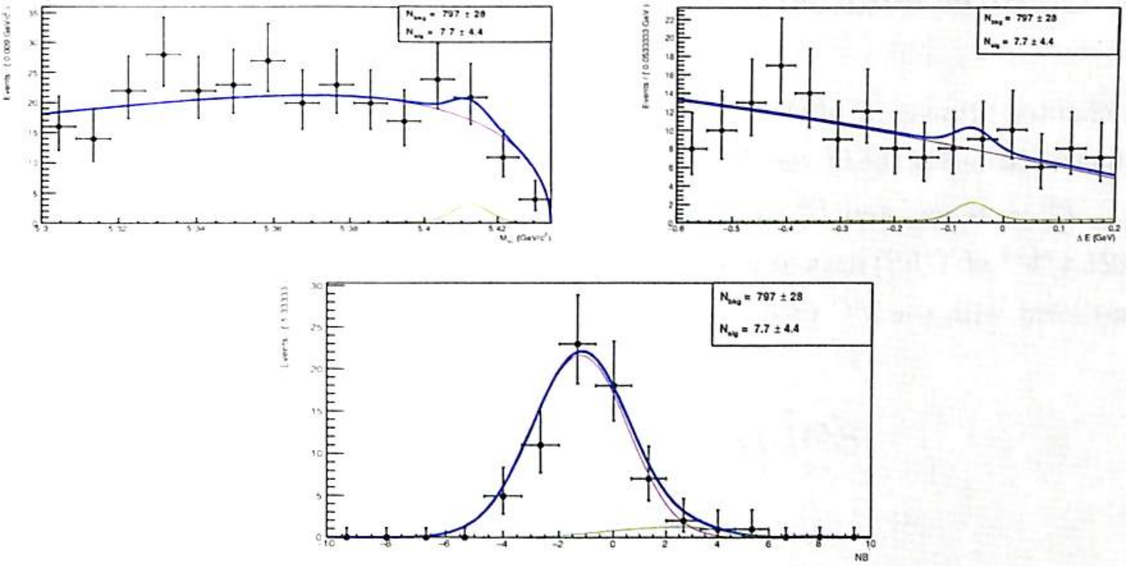

FIGURE 4.33: *Real Data Fit Results for $B_s^0 \to \eta_{\gamma\gamma}\eta_{3\pi}$ mode. The points with the error bars are the real data points and the blue, purple and green lines represent the total PDF, signal PDF and background PDF, respectively.*

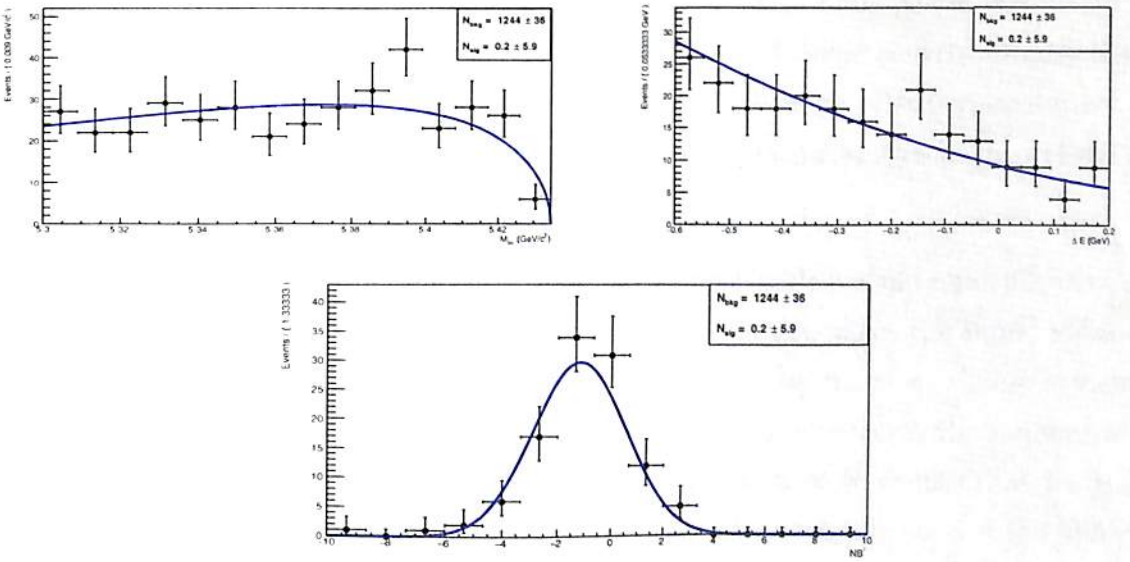

FIGURE 4.34: *Real Data Fit Results for $B_s^0 \to \eta_{3\pi}\eta_{3\pi}$ mode. The points with the error bars are the real data points and the blue, purple and green lines represent the total PDF, signal PDF and background PDF, respectively.*

4.8 Chapter summary

This chapter presents a brief introduction to the ML fit procedure and the PDF parameterizations of the fit variables of signal and background components for $B_s^0 \to \eta_{\gamma\gamma}\eta_{\gamma\gamma}$, $B_s^0 \to \eta_{\gamma\gamma}\eta_{3\pi}$ and $B_s^0 \to \eta_{3\pi}\eta_{3\pi}$ mode, respectively. Unblinded results from the $121.4 fb^{-1}$ of $\Upsilon(5S)$ data also presented. The observation in the real data sample is consistent with the MC prediction.

Chapter 5

Systematic Uncertainties

This chapter provides the different sources of the systematic uncertainties and their impact on the final results of this analysis. Systematic errors affect all the data in the same way i.e., systematically. Repeated measurements share the same systematic effect and are therefore correlated to each other. Thus, these errors can not be reduced by performing repeated measurements. Typical sources of systematics are improper calibration of the detector, poor knowledge of experimental set up, acceptance and sensitivity of detector components, uncertainties in theoretical and experimental inputs etc.

There are two types of systematic uncertainties: additive and multiplicative systematic uncertainties. Multiplicative systematics do not affect the signal yield and signal significance of the decay but affect its branching fraction. These systematics arise from the uncertainty in signal reconstruction efficiency, the number of B_s mesons and from the fraction $f_{B_s^{0*}\bar{B}_s^{0*}}$ i.e. the fraction of $b\bar{b}$ events that hadronize to $B_s^*\bar{B}_s^*$ events. Additive systematics reduce the signal significance of the observed peak and changes the branching fraction of the decay. Additive systematics arise from the fit procedure, which includes the uncertainty due to the PDF modeling and fit bias, respectively. The different sources of systematic uncertainties that may affect the decay mode studied in this analysis are discussed in this chapter.

5.0.1 Fit bias

From our fit bias studies, documented in Section 4.6, we have obtained an average fit bias of (0.07±0.02), (−0.05±0.02) and (0.10±0.02) for $B_s^0 \to \eta_{\gamma\gamma}\eta_{\gamma\gamma}$, $B_s^0 \to \eta_{\gamma\gamma}\eta_{3\pi}$ and $B_s^0 \to \eta_{3\pi}\eta_{3\pi}$ modes, respectively.

5.0.2 PDF Modeling

The systematic uncertainty due to PDF modeling is evaluated by changing each fixed parameter of PDF by $\pm 1\sigma$ and repeating the fit. Deviation in signal yield from the original fit are added in quadrature to obtain the systematic uncertainty. The PDF modeling unecrtainties are computed to be ±0.4, ±0.91 and ±0.02 events for $B_s^0 \to \eta_{\gamma\gamma}\eta_{\gamma\gamma}$, $B_s^0 \to \eta_{\gamma\gamma}\eta_{3\pi}$ and $B_s^0 \to \eta_{3\pi}\eta_{3\pi}$ modes, respectively.

5.0.3 MC statistics

The statistical error in the signal efficiency contributes to the systematic uncertainty. The uncertainty due to MC statistics is computed as:

$$\Delta\epsilon = \sqrt{\frac{\epsilon\times(1-\epsilon)}{N}}$$

where N is the total number of signal MC events processed. We have generated 100,000 signal events for each of the three modes: $B_s^0 \to \eta_{\gamma\gamma}\eta_{\gamma\gamma}$, $B_s^0 \to \eta_{\gamma\gamma}\eta_{3\pi}$ and $B_s^0 \to \eta_{3\pi}\eta_{3\pi}$. The signal efficiencies $(\epsilon \pm \Delta\epsilon)$ for $B_s^0 \to \eta_{\gamma\gamma}\eta_{\gamma\gamma}$, $B_s^0 \to \eta_{\gamma\gamma}\eta_{3\pi}$ and $B_s^0 \to \eta_{3\pi}\eta_{3\pi}$ modes are computed to be (9.62 ± 0.09)%, (9.48 ± 0.09)% and (8.14±0.08)% for , respectively. Thus, the uncertainty due to MC statistics $\left(\frac{\Delta\epsilon}{\epsilon}\right)$ is computed to be 0.93%, 0.94% and 0.98% for $B_s^0 \to \eta_{\gamma\gamma}\eta_{\gamma\gamma}$, $B_s^0 \to \eta_{\gamma\gamma}\eta_{3\pi}$ and $B_s^0 \to \eta_{3\pi}\eta_{3\pi}$ modes, respectively.

5.0.4 Uncertainty on the pion Identification Efficiency (K/π Systematics)

This uncertainty has been studied using the PID table provided by Belle PID joint group. PID performance depends on the laboratory momentum ($p = |\vec{p}|$) and polar angle (θ). In the table, the ratio of PID efficiency in data and MC are provided as a function of 'p' and 'cos(θ)'. After incorporating the PID table in our reconstruction code, we have obtained π ID efficiencies as $(94.76 \pm 0.02)\%$ and $(95.11 \pm 0.02)\%$ per pion in $B_s^0 \to \eta_{\gamma\gamma}\eta_{3\pi}$ mode and $B_s^0 \to \eta_{3\pi}\eta_{3\pi}$ mode, respectively and the corresponding systematic uncertainties are 2.8% and 4.0% in $B_s^0 \to \eta_{\gamma\gamma}\eta_{3\pi}$ mode and $B_s^0 \to \eta_{3\pi}\eta_{3\pi}$ mode, respectively.

5.0.5 Uncertainty due to the Tracking efficiency

The uncertainty on the tracking efficiency was evaluated using partially reconstructed D^* decays. Its value is estimated to be $(-0.13 \pm 0.30 \pm 0.10)\%$ for any charged track of momentum > 200 MeV/c. Since, the value is much smaller than the statistical uncertainty associated with it, therefore, the total systematic uncertainty is taken as the quadratic sum of the actual value and its uncertainties. Thus, the recommended systematic uncertainty is 0.35% per track (of momentum > 200 MeV/c) [67].

5.0.6 Branching fraction of η

The branching fractions of $\eta \to \gamma\gamma$ and $\eta \to \pi^+\pi^-\pi^0$ are $(39.41 \pm 0.20)\%$ and $(22.92 \pm 0.28)\%$ (PDG) respectively. Thus multiplicative systematic uncertainties of 0.20% and 0.28% are assigned for $\eta \to \gamma\gamma$ and $\eta \to \pi^+\pi^-\pi^0$ modes, respectively.

5.0.7 $\eta, \pi^0 \to \gamma\gamma$ selection efficiency

Systematic errors arise due to π^0 and η detection efficiencies. A 3.0% systematic error due to π^0 detection is determined from a comparison of the data and MC ratios for a large sample of $\eta \to \pi^+\pi^-\pi^0$ and $\eta \to 3\pi^0$ decays. Since $\eta \to \gamma\gamma$ decays is similar to π^0 decay, we also assign a 3.0% systematic error for $\eta \to \gamma\gamma$ reconstruction [68].

5.0.8 The number of B_s^0 mesons

The total number of B_s^0 mesons are calculated as, $N(B_s^0) = 2 \times L_{int}^{\Upsilon(5S)} \times \sigma_{b\bar{b}}^{\Upsilon(5S)} \times f_s$, where $L_{int}^{\Upsilon(5S)}$ is the integrated luminosity and $\sigma_{b\bar{b}}^{\Upsilon(5S)}$ is the $b\bar{b}$ production cross section at $\Upsilon(5S)$ resonance and f_s is the fraction of $b\bar{b}$ events that hadronize from $B_s^* \bar{B}_s^*$ events. Thus the systematic uncertainty on the number of B_s^0 mesons is the quadratic sum of the uncertainties in $L_{int}^{\Upsilon(5S)}$, $\sigma_{b\bar{b}}^{\Upsilon(5S)}$ and f_s. The uncertainties are 1.3% on $L_{int}^{\Upsilon(5S)}$, 4.7% on $\sigma_{b\bar{b}}^{\Upsilon(5S)}$ and 17.4% on f_s, respectively [69–71].

5.0.9 Fraction $f_{B_s^{0*}\bar{B}_s^{0*}}$

The value of $f_{B_s^{0*}\bar{B}_s^{0*}}$, the fraction of $b\bar{b}$ events that hadronize to $B_s^* \bar{B}_s^*$ events is $(87.0 \pm 1.7)\%$ [70, 71]. Thus, a systematic uncertainty of 2.0% is assigned due to $f_{B_s^{0*}\bar{B}_s^{0*}}$.

5.0.10 Calibration factors

To extract the signal and background yields in the real data sample, we are using PDFs which are established based on MC samples and hence to take into account any difference in data versus MC, we are using the control sample to measure this systematic uncertainty. As MC does not resemble the data exactly, therefore, we calibrate the M_{bc}, ΔE and NB' mean and sigma of $B_s^0 \to \eta\eta$ signal using $B^0 \to \eta\eta$ as control sample. The details of the $B^0 \to \eta\eta$ analyis is discussed in Belle Note 1402 [72, 73]. They use the same final state particles and decay modes to reconstruct $B^0 \to \eta\eta$ as we use to reconstruct $B_s^0 \to \eta\eta$ signal. Using the observed signals in the $B^0 \to \eta\eta$ study, the mean and sigma correction factors for M_{bc}, ΔE and NB' are estimated using the mean and sigma values from signal MC and the observed signal yield. The details of the fit parameters obtained from both signal MC and from the observed signal yields are presented in Table 5.1.

The M_{bc} mean value for MC and real data matches very well, indicating that no correction is required for M_{bc} but the ΔE mean value is shifted by about 3 MeV to take into account the difference in data and MC in the control sample. To estimate the uncertainties associated with M_{bc} sigma, ΔE sigma, NB' mean and NB' sigma,

Parameter	MC fit value (GeV/c^2)	Real Data fit value (GeV/c^2)
M_{bc} mean	5.2796645 ± 0.0000051	5.2800 ± 0.003
M_{bc} sigma	0.0031030 ± 0.0000041	0.0050 ± 0.0005
ΔE mean	-0.022587 ± 0.00017	-0.01901 ± 0.0003
ΔE sigma	0.08397 ± 0.001804	0.0859825 ± 0.002002
NB' mean	3.8781 ± 0.04365	3.1533 ± 0.05830
NB' sigma	2.3830 ± 0.058330	2.82905 ± 0.092195

TABLE 5.1: *Corrections of M_{bc}, ΔE and NB' mean and sigma for $B_s^0 \to \eta\eta$ signal.*

we will vary their values by $\pm 3\sigma$ in the final fitter and the maximum deviation in the yield will be considered as a source of systematic uncertainty.

5.0.11 Final Systematic Uncertainties

Table 5.2 and 5.3 summarize all the additive and multiplicative systamatic uncertainties considered in this analysis.

Sub decay mode	$B_s^0 \to \eta_{\gamma\gamma}\eta_{\gamma\gamma}$	$B_s^0 \to \eta_{\gamma\gamma}\eta_{3\pi}$	$B_s^0 \to \eta_{3\pi}\eta_{3\pi}$	Combined
Fit bias	-0.058 ± 0.005	0.015 ± 0.005	0.038 ± 0.005	0.059 ± 0.008
PDF Modeling	0.4	0.91	0.02	0.99

TABLE 5.2: *Summary of additive systematic uncertainties.*

Sub decay mode	$B_s^0 \to \eta_{\gamma\gamma}\eta_{\gamma\gamma}$	$B_s^0 \to \eta_{\gamma\gamma}\eta_{3\pi}$	$B_s^0 \to \eta_{3\pi}\eta_{3\pi}$	Combined
$\eta, \pi^0 \to \gamma\gamma$ selection efficiency	6.0	6.0	6.0	6.0
$B(\eta \to \gamma\gamma)$	0.28	0.20	-	0.34
$B(\eta \to \pi^+\pi^-\pi^0)$	-	0.28	0.39	0.48
NB' requirement	-	-	-	10.6
Pion Identification	-	2.8	4.0	4.8
Tracking efficiency	-	0.7	1.4	1.0
MC statistics	0.93	0.94	0.98	1.6
Calibration factors	-	-	-	3.1
L_{int}	-	-	-	1.3
$\sigma_{b\bar{b}}^{\Upsilon(5S)}$	-	-	-	4.7
Fraction $f_{B_s^{0*}\bar{B}_s^{0*}}$	-	-	-	17.4

TABLE 5.3: *Summary of multiplicative systematic uncertainties.*

5.1 Chapter summary

In this chapter we summarize the different sources of systematic uncertainties that might affect the measurement of the branching ratio for the decay $B_s^0 \to \eta\eta$. The values of different systematic uncertainties are estimated and listed for the decay.

Chapter 6

Results and Conclusions

This chapter presents the final results of the analysis for the decay $B_s \to \eta\eta$. The estimation of signal significance and the Bayesian Upper Limit on the branching fraction of the decay at 90% confidence level are discussed in this chapter.

6.1 Signal Significance

We have performed a 3D unbinned extended maximum likelihood fit to extract the signal yield for the decay $B_s^0 \to \eta\eta$. Signal significance for the observation is calculated by assuming a null or background only hypothesis [58, 59]. It is calculated as $S = sign(N_{signal}) * \sqrt{-2 * ln(\frac{L_0}{L_{max}})}$, where N_{signal} is the yield of $B_s \to \eta\eta$ signal obtained from the likelihood fit, L_0 is the likelihood value when the signal yield is constrained to 0 and L_{max} is the maximum value of the likelihood fit. To incorporate the additive systematic uncertainties, the plain likelihood curve is convolved with a Gaussian of width equal to the additive systematic uncertainties i.e., $\sigma = \sigma_{add.syst.}$ Convolution of two functions f and g over an infinite range is defined as:

$$h(x) = f(x) * g(x) = \int_{-\infty}^{+\infty} f(x-y)g(y)dy \tag{6.1}$$

Figure 6.1, 6.2 and 6.3 show the profile and plain likelihood plots for the $B_s^0 \to \eta_{\gamma\gamma}\eta_{\gamma\gamma}$, $B_s^0 \to \eta_{\gamma\gamma}\eta_{3\pi}$ and $B_s^0 \to \eta_{3\pi}\eta_{3\pi}$ modes, respectively. To calculate the final signal significance and the upper limit on the branching fraction, we have combined the individual likelihoods for the three η sub-decay modes. Figure 6.4 shows the combined profile and plain likelihood plots. The signal significance for the decay $B_s^0 \to \eta\eta$ is computed to be 1.044.

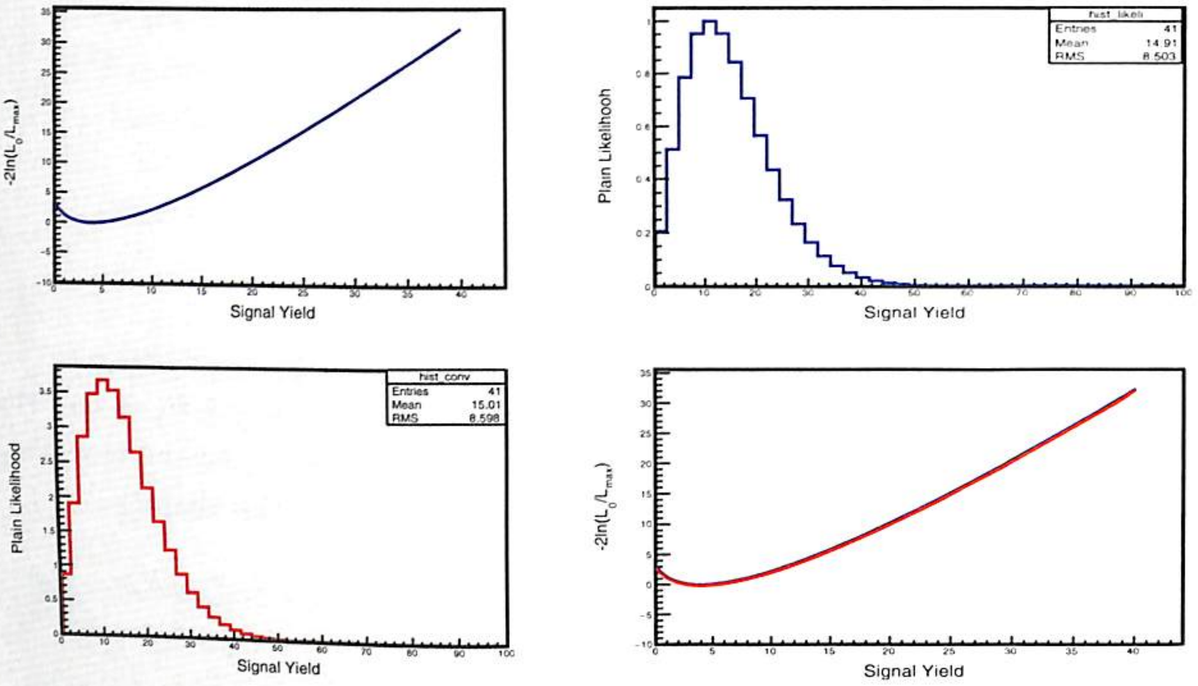

FIGURE 6.1: *Profile and plain likelihood curves for the decay $B_s^0 \to \eta_{\gamma\gamma}\eta_{\gamma\gamma}$. Blue (red) curves denotes the likelihood curves before (after) convolution.*

6.2 Calculation of Upper Limit

Since we have not seen significant signal yield for the decay $B_s^0 \to \eta\eta$, we estimate the 90% CL UL on the BF of the decay using Bayesian technique [59]. We have done this by incorporating the systematics by convolving the plain likelihood curve with a Gaussian of width equal to total additive systematics uncertainties. Then we modify the likelihood curve and integrate the curve from 0 till we obtain 90% of the total integral under the likelihood curve to obtain the 90% CL upper limit of N_{signal} and hence the BF. The UL of the BF for the decay $B_s^0 \to \eta\eta$ is computed as:

$$90\%\ \text{CL UL of}\ \mathcal{B}(B_s \to \eta\eta) \quad = \quad \frac{90\%\ \text{CL UL of}\ N_{signal}}{\epsilon \times N_{B_s^0} \times f_{B_s^{0*}\bar{B}_s^{0*}}}$$

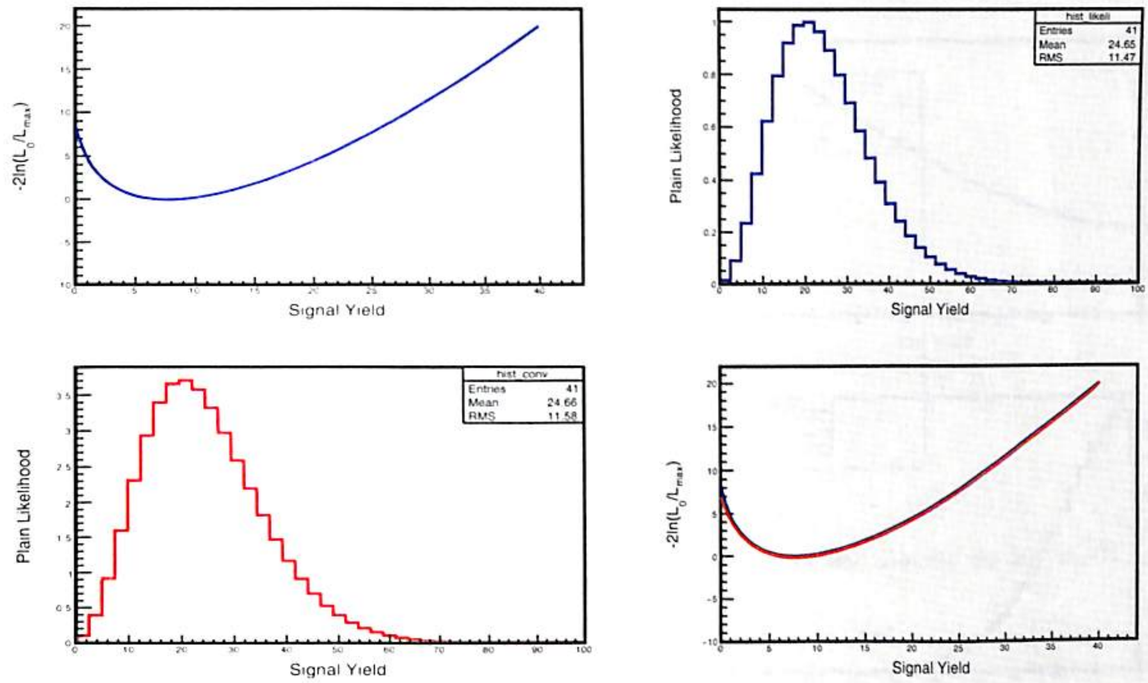

FIGURE 6.2: *Profile and plain likelihood curves for the decay* $B_s^0 \to \eta_{\gamma\gamma}\eta_{3\pi}$. *Blue (red) curves denotes the likelihood curves before (after) convolution.*

where, (90% CL UL of N_{signal}) is the 90% CL UL of the signal yield of $B_s^0 \to \eta\eta$ signal and ϵ is the signal selection efficiency of $B_s^0 \to \eta\eta$ signal. Figure 6.5 shows the likelihood vs BF for $B_s^0 \to \eta\eta$ with the blue line showing the UL at 90% CL. Thus, the 90% CL UL of $B_s^0 \to \eta\eta$ BF is estimated to be 56.53×10^{-6}. The $B_s^0 \to \eta\eta$ results are presented in Table 6.1

Parameter	**Value**
L_{int}	$(121.4 \pm 1.6)\ fb^{-1}$
ϵ (average)	$(9.08 \pm 0.08)\%$
$f_{B_s^{0*}\bar{B}_s^{0*}}$	$(87.0 \pm 1.7)\%$
$\sigma_{b\bar{b}}^{\Upsilon(5S)}$	$(0.340 \pm 0.016)\ nb$
$N_{B_s^0}$	$(14.2 \pm 2.6) \times 10^6$
90% CL UL of $\mathcal{B}(B_s^0 \to \eta\eta)$	56.53×10^{-6}

TABLE 6.1: $B_s^0 \to \eta\eta$ *results*

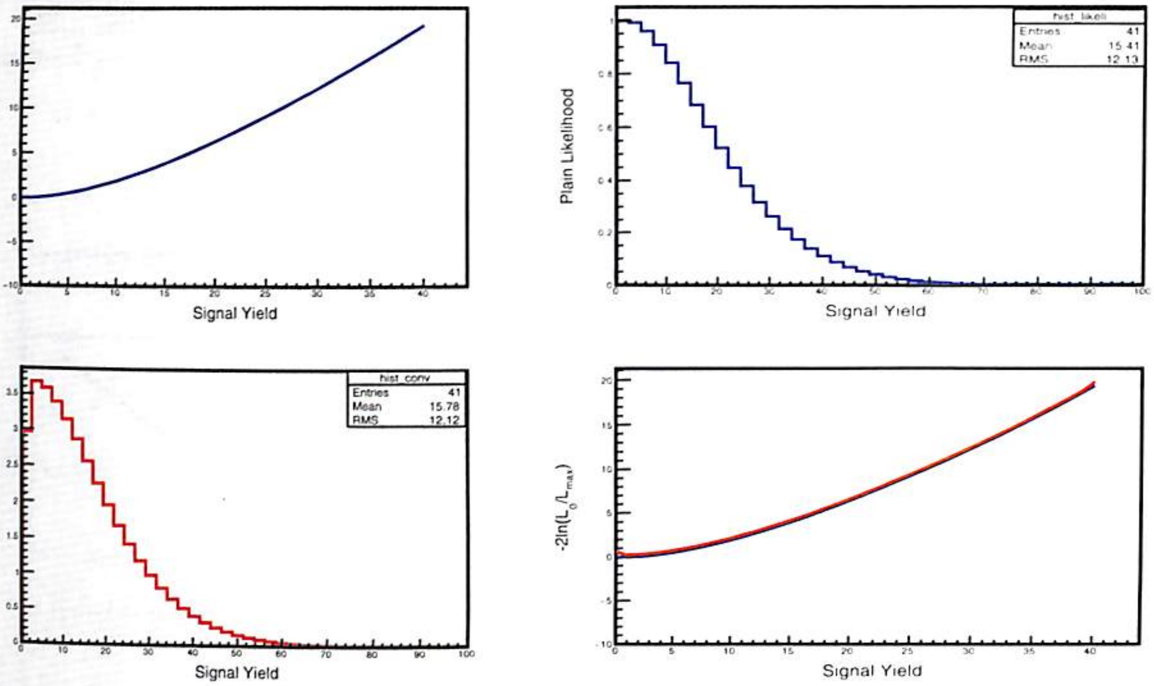

FIGURE 6.3: ***Profile and plain likelihood curves for the decay*** $B_s^0 \to \eta_{3\pi}\eta_{3\pi}$. *Blue (red) curves denotes the likelihood curves before (after) convolution.*

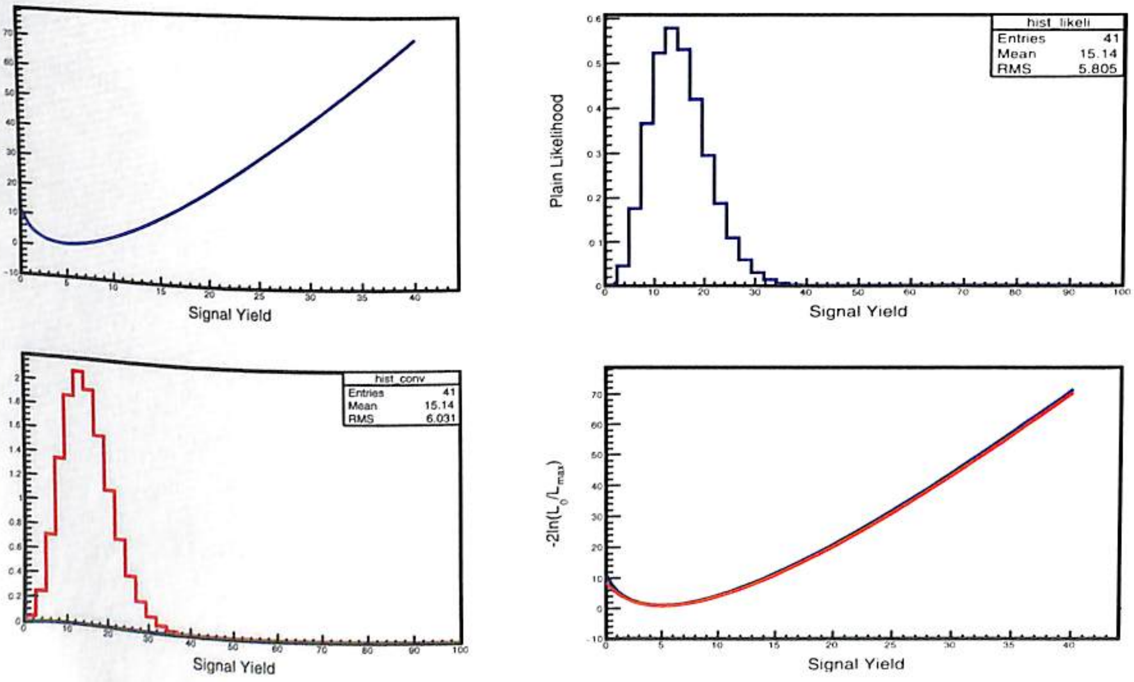

FIGURE 6.4: ***Profile and plain likelihood curves after combining all the three decay modes.*** *Blue (red) curves denotes the likelihood curves before (after) convolution.*

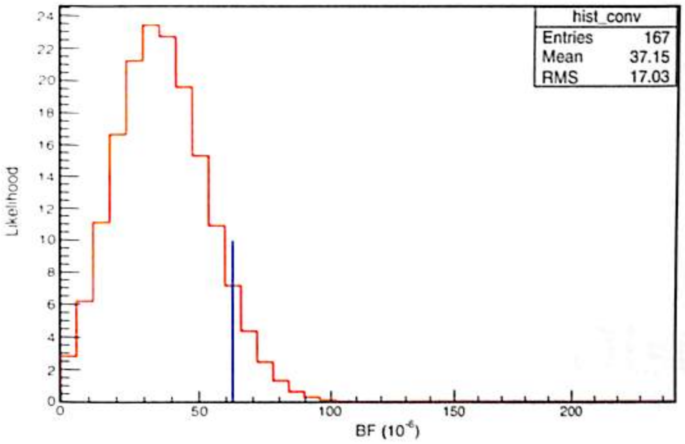

FIGURE 6.5: *Likelihood vs BF for $B_s^0 \to \eta\eta$ with the blue line showing the UL at 90% CL.*

6.3 Summary and Conclusions

This thesis presents the results of the search for the decay $B_s^0 \to \eta\eta$ at high energy e^+e^- collisions. The search is done using $121.4 fb^{-1}$ of data collected by the Belle detector at $\Upsilon(5S)$ energy. No significant signal yield is observed for the decay $B_s^0 \to \eta\eta$ and in the absence of any significant signal yield, we set the 90% CL UL on its BF to be 6.3×10^{-5}. This is an improvement of about two orders of magnitude from the previous measurement of UL by the L3 experiment. With a dedicated run at $\Upsilon(5S)$ resonance to collect an order of magnitude more statistics, the Belle II experiment has the potential to make a discovery of this charmless $B_s^0 \to \eta\eta$ decay. LHCb has the limitation on the measurement of the branching fraction for this decay since the reconstruction of η and π^0 candidates require detection of single energy clusters in the calorimeter, which may be difficult at LHCb.

Appendix A

Details of Probability Distribution Functions

In this section we present the functional form of some of the functions which we have used to model the signal and background PDFs.

A.1 Crystal Ball Function

The CBall function is a Gaussian with a power law tail that is traditionally used to describe the effect of radiative energy loss in an invariant mass or an energy difference distribution [61, 62]. It is given by:

$$f(x|\mu, \sigma, \alpha, n) = N. \begin{cases} \exp\left(\dfrac{-(x-\mu)^2}{2\,\sigma^2}\right), \text{ for } \dfrac{x-\mu}{\sigma} > -\alpha \\ \left(\dfrac{n}{\alpha}\right)^2 \exp\left(\dfrac{-|\alpha|^2}{2}\right)\left(\dfrac{n}{|\alpha|} - |\alpha| - \dfrac{x-\mu}{\sigma}\right)^{-n}, \text{ for } \dfrac{x-\mu}{\sigma} \leqslant -\alpha \end{cases}$$

where, N is the normalization factor and μ, σ, α and n are the parameters of the CBall function. μ and σ denotes the mean and sigma of the Gaussian part. The n parameter controls the slope of the exponential part and is usually held fixed in a fit. Lower values of n generate a longer tail. The parameter α determines the crossover point from the Gaussian distribution to the power law distribution, in units of the peak width σ. When α is positive, the tail is below the peak (i.e., in the left) and when it is negative, it is above the peak.

A.2 Argus Function

The Argus function [61, 62, 74] is an empirical function first used by the ARGUS collaboration. It is frequently used in B physics analysis and mostly used to model the invariant mass or $M_{\rm bc}$ distribution of the combinatorial background. It is defined as:

$$f(x|a_0, a_1) = \frac{1}{N}\, x\sqrt{1-\left(\frac{x}{a_0}\right)^2}\, \exp\left[a_1\left(1-\left(\frac{x}{a_0}\right)^2\right)\right]\Theta(x < a_0)$$

where, Θ is a step function with $\Theta(x < a_0) = 1$ and $\Theta(x > a_0) = 0$. a_0 denotes the threshold of the invariant mass distribution and is usually held fixed in a fit. a_1 denotes the curvature of the Argus distribution.

A.3 Chebychev Polynomial

The Chebyshev polynomials are a sequence of orthogonal polynomials which can be defined recursively as:

$$T_{n+1}(x) = 2xT_n(x) - T_{n-1}(x)$$

The first few Chebychev polynomials are:

$$\begin{aligned}
T_0(x) &= 1.\\
T_1(x) &= x.\\
T_2(x) &= 2x^2 - 1.\\
T_3(x) &= 4x^3 - 3x.\\
T_4(x) &= 8x^4 - 8x^2 + 1.\\
&\vdots
\end{aligned}$$

Any arbitrary polynomial of degree N can be written in terms of Chebychev polynomial [61, 62] as:

$$f(x|c_i) = \frac{1}{N}\left[T_0(x) + \sum_{i=1}^{N} c_i T_i(x)\right]$$

where, $T_i(x)$ is a i^{th} order Chebychev polynomial. The parameters c_i's are coefficients of the functions T_i's. Chebychev polynomials are orthogonal in the interval [-1,1]. Due to lower correlations between coefficients in a fit, they have superior stability than normal polynomial functions.

Appendix B

NeuroBayes input variables

In this appendix, we present the plots of the event shape variables used in the event classifier (NeuroBayes).

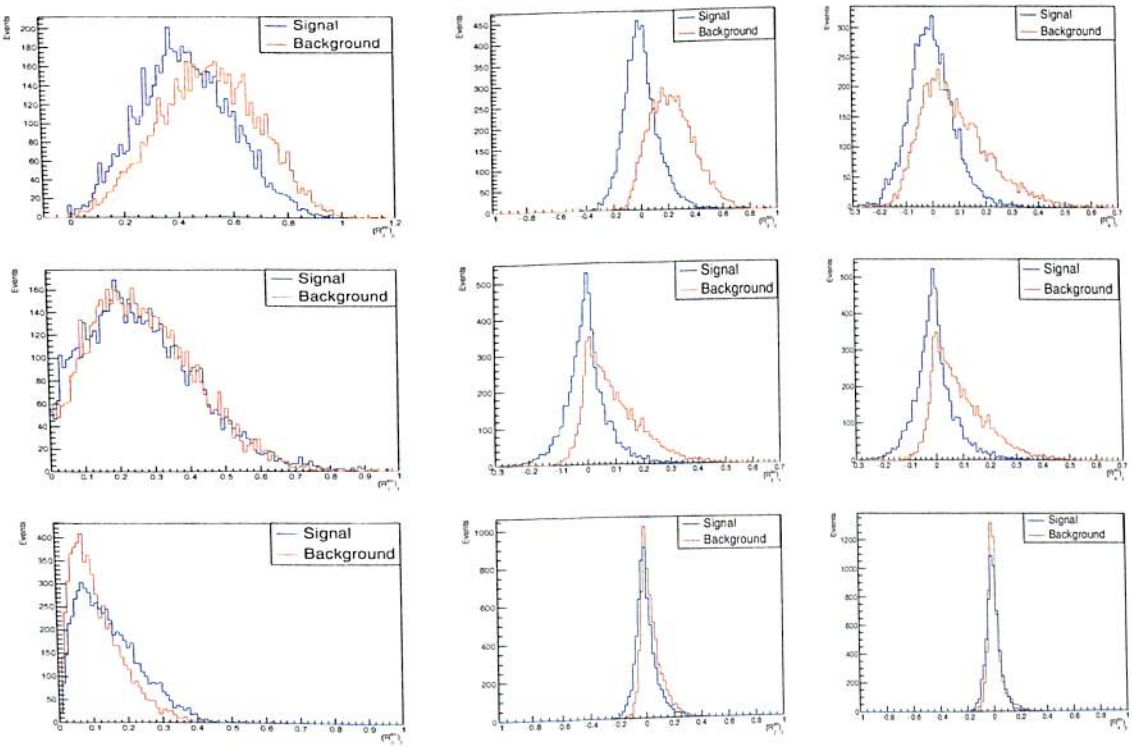

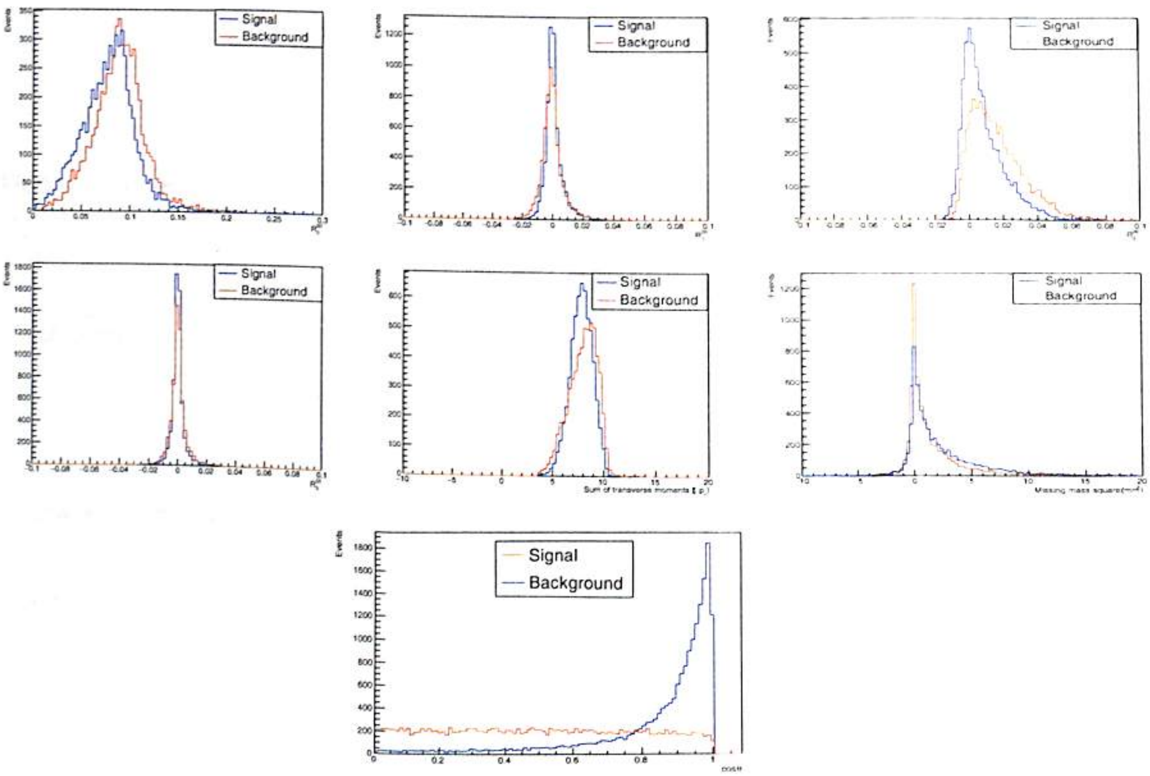

FIGURE B.1: Continuum suppression variables for $B_s^0 \to \eta_{\gamma\gamma}\eta_{\gamma\gamma}$

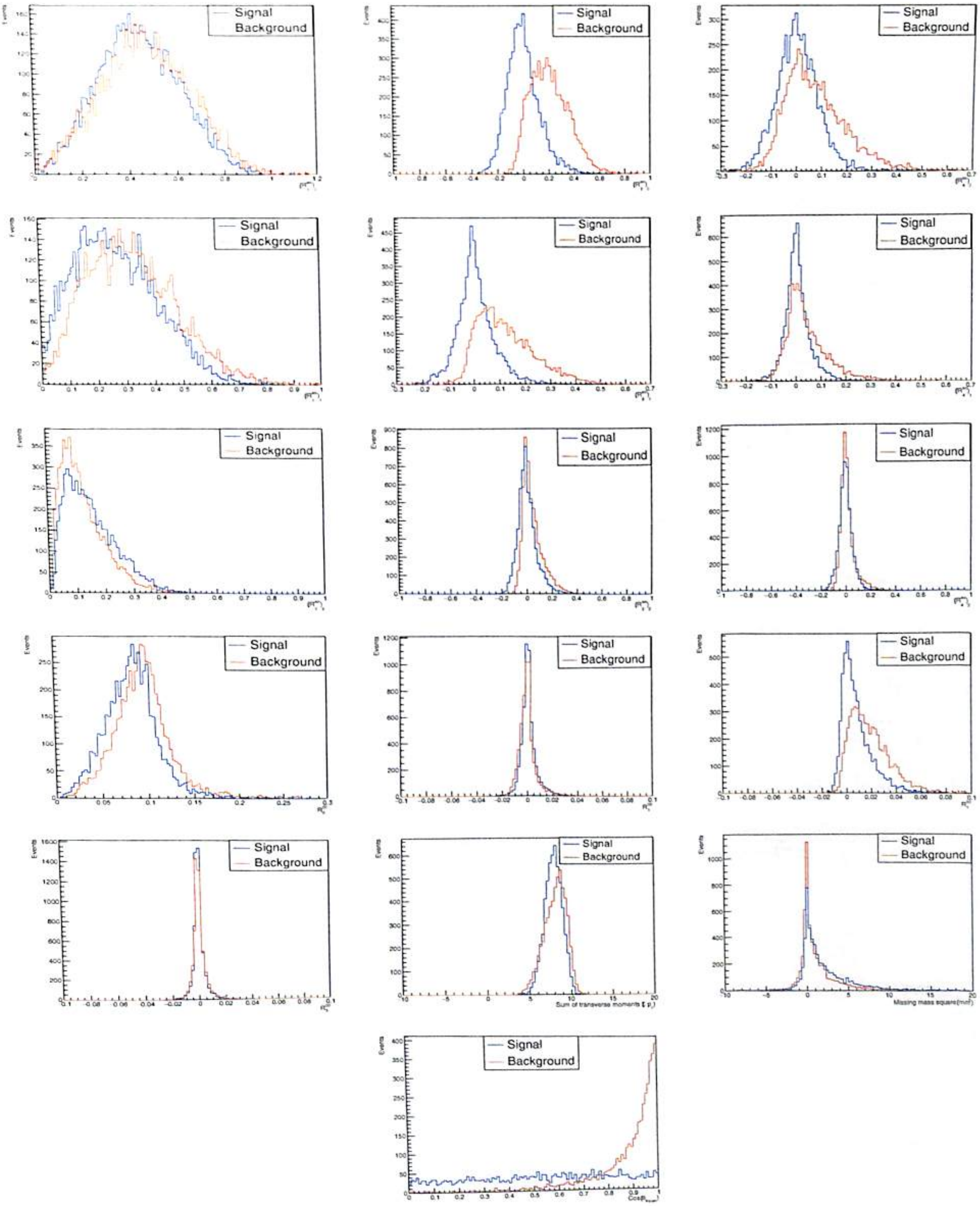

FIGURE B.2: Continuum suppression variables for $B_s^0 \to \eta_{\gamma\gamma}\eta_{3\pi}$

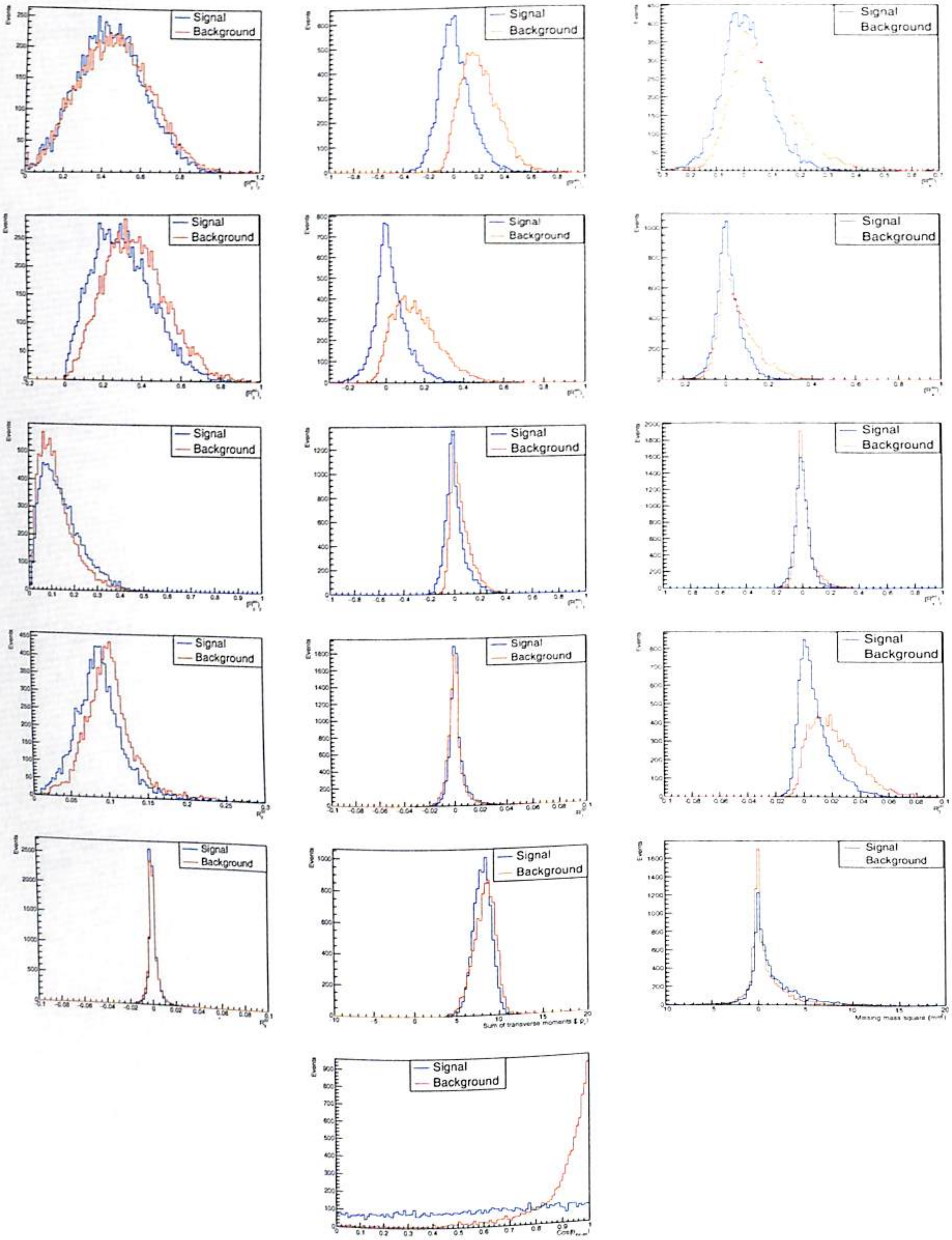

FIGURE B.3: Continuum suppression variables for $B_s^0 \to \eta_{3\pi}\eta_{3\pi}$

Appendix C

Acronyms and Abbreviations

ACC	Aerogel Cherenkov Counter
ADC	Analogue-to-Digital Converter
BASF	Belle AnalysiS Framework
BF	Branching Fraction
BFGS	Broyden-Fletcher-Goldfarb-Shanno
BGO	Bismuth Germanium Oxide ($Bi_4Ge_3O_{12}$)
CDC	Central Drift Chamber
CFS	Columbia-Fermilab-Stony Brook
CsI	Cesium Iodide
CKM	Cabibbo-Kobayashi-Maskawa
CL	Confidence Level
CM	Centre of Mass
CP	Charge-Parity
CPV	Charge-Parity Violation
DAQ	Data Acquisition
DSSD	Double sided Silicon-Strip Detectors
DST	Data Summary Tapes
ECL	Electromagnetic Calorimeter
EFC	Extreme Forward calorimeter
EFT	Effective Field Theory
FCNC	Flavor Changing Neutral Current
FM-PMT	Fine-Mesh Photo Multiplier Tubes

FSI	Final State Interactions
GDL	Global Decision Logic
GIM	Glashow-Iliopoulos-Maiani
h.c.	Hermitian conjugate
2HDM	Two Higgs Doublet Model
HER	High Energy Ring
HJM	Heavy Jet Mass
HQE	Heavy Quark Expansion
IP	Interaction Point
KEK	High Energy Accelerator Research Organization
KLM	K_L and Muon detector
KSFW	Kakuno Super Fox-Wolfram
LER	Low Energy Ring
LINAC	LINear ACcelerator
MC	Monte Carlo
MDST	Mini Data Summary Tapes
OPE	Operator Product Expansion
PDF	Probability Distribution Functions
PHSP	(N-body) PHase SPace
PID	Particle IDentity
PMT	Photo Multiplier Tubes
QCD	Quantum ChromoDynamics
QED	Quantum ElectroDynamics
QFT	Quantum Field Theory
RG	Renormalization Group
RI	Refractive Index
RPC	Resistive Plate Counter
RPV	R-Parity Violation model
SM	Standard Model
SUSY	SUper SYmmetry
SVD	Silicon Vertex Detector
SVP_HELAMP	Scalar to Vector and Photon HELicity AMPlitude
Tl	Thallium
TDC	Time-to-Digital Converter
TOF	Time Of Flight

TSC	Trigger Scintillation Counter
UL	Upper Limit
VSS	Vector to Scalar and Scalar
VSP_PWAVE	Vector to Scalar and Photon PWAVE

Appendix D

Technical Reports and Books:

- Kamal Jyoti Nath, Bipul Bhuyan, Search for the decay $B_s^0 \to \eta\eta$ at $\Upsilon(5S)$ resonance. Belle Note 1403.
- The Belle II Physics Book.

Publications:

- K.J.Nath and B.Bhuyan Search for the Decay $B_s^0 \to \eta\eta$ at $\Upsilon(5S)$ Resonance. To be published in PRD(RC). Currently under review.
- K.J.Nath and B.Bhuyan
  Search for the Decay $B_s^0 \to \eta\eta$ at $\Upsilon(5S)$ Resonance,
  SpringerProc. Phys. **174**, 203(2016).*doi* : 10.1007/978−3−319−25619−1−32
- K. J. Nath [Belle Collaboration]
  Recent results on charmless B^0 and B_s^0 decays from Belle PoS ICHEP **2016**, 535 (2016).
- http://inspirehep.net/search?ln=enp=findakjnathof=hbactionsearch=Searchsf=earliest

Schools/Workshops/Collaboration Meeting/Coferences Attended:

- SERC school on Experimental High Energy Physics, 20 June-10 July 2011, VECC, Kolkata. http://indico.vecc.gov.in/indico/conferenceDisplay.py?confId=7
- Belle Analysis Workshop 2014, February 24 - March 4, 2014, IITG. http://www.iitg.ac.in/physics/fac/bhuyan/BAW2014/index.html
- Workshop on EWSB and flavours in the light of LHC at IIT Guwahati, Assam, during 20-22 Feb, 2014. http://www.iitg.ac.in/EWSB2014/
- XXI DAE-BRNS High Energy Physics Symposium 2014, 8-12 December 2014, IITG. http://www.iitg.ac.in/DAE-HEP2014/public/
- Belle(II) Analysis Workshop, 9 - 17 March, 2015, IIT Madras. https://kds.kek.jp/indico/event/17971/
- 22 B2GM, 19-23 October, 2015, Kenkyu-Honkan, Tokyo, Japan. https://kds.kek.jp/indico/event/19519/registration/registrants
- 38th International Conference on High Energy Physics, August 3 - 10, 2016, Chicago, U.S.A. https://www.ichep2016.org/
- CKM2016, 9th International Workshop on the CKM Unitarity Triangle TIFR, Mumbai, November 28 - December 2, 2016. http://www.tifr.res.in/ ckm16/
- Post-CKM school, December 3 - 7, TIFR, Mumbai.
- National Seminar on Nuclear and High Energy Physics, 30 -31 March, 2018, Gauhati University. http://web.gauhati.ac.in/nahep/about

Bibliography

[1] M. G. et al., Preprint TECHNION-PH-95-11 .

[2] A. Ali et al., Phys. Rev. D **76**, 074018 (2007).

[3] G. L. Kane, *Modern Elementary Particle Physics*, Addison-Wesley, 1987.

[4] M. Herrero, arXiv: hep-ph/9812242 **3** (1998).

[5] S. Oggero, *Beauty in the Crowd:Commissioning of the LHCb pile-up detector and First evidence of $B_s \rightarrow \mu^+\mu^-$*, PhD thesis, Amsterdam: Vrije Universiteit, LHCb collaboration, 2013.

[6] E. Salvati, Open Access Dissertations , 201 (2010).

[7] C. Caso et al., Eur. Phys. J. C, 1998.

[8] B. Martin and G. Shaw, *Particle Physics*, volume 45, John Wiley & Sons, 2008.

[9] D. Decamp et al., Phys. Lett. **B231**, 519 (1989).

[10] D. Decamp et al., Phys. Lett. **B235**, 399 (1990).

[11] M. Fukugita and T. Yanagida, Phys. Lett. **B174**, 45 (1986).

[12] L. Bergström, Rep. Progr. Phys. **63**, 793 (2000).

[13] Y. Fukuda et al., Phys. Rev. Lett. **81**, 1562 (1998).

[14] L.-L. Chau and W.-Y. Keung, Phys. Rev. Lett. **53**, 1802 (1984).

[15] L. Wolfenstein, Phys. Rev. Lett. **51**, 1945 (1983).

[16] F. Lehner, *Flavor changing neutral currents at hadron colliders*, PhD thesis, Universitat Zurich, $D\phi$ collaboration, 2005.

[17] R. P. Bernhard, *Search for rare decays of the B_s meson with the $D\phi$ experiment*, PhD thesis, Universitat Zurich, $D\phi$ collaboration, 2005.

[18] Y. Sato, *Measurement of Forward-Backward asymmetry in the $B \to X_s l^+ l^-$ decay with semi-inclusive method*, PhD thesis, Tohoku University, Belle collaboration, 2013.

[19] S. L. Glashow, J. Iliopoulos, and L. Maiani, Phys. Rev. D **2**, 1285 (1970).

[20] G. Buchalla, A. J. Buras, and M. E. Lautenbacher, Rev. of Mod. Phys. **68**, 1125 (1996).

[21] A. J. Buras, Operator product expansion, renormalization group and weak decays, in *Quantum Field Theory*, pages 65–85, Springer, 2000.

[22] A. J. Buras and R. Fleischer, arXiv: hep-ph/9704376 (1997).

[23] A. J. Buras, arXiv: hep-ph/9806471 (1998).

[24] A. J. Buras, Nucl. Instrum. Meth. Phys. Res., Sect. A **368**, 1 (1995).

[25] M. E. Peskin and D. V. Schroeder, *An introduction to quantum field theory*, Westview, 1995.

[26] F. Su, Y.-L. Wu, Y.-B. Yang, and C. Zhuang, Journal of Physics G: Nuclear and Particle Physics **38**, 015006 (2011).

[27] Y.-Y. Keum, H.-n. Li, and A. I. Sanda, Phys. Rev. D **63**, 054008 (2001).

[28] M. Beneke, G. Buchalla, M. Neubert, and C. Sachrajda, Nuclear Physics B **591**, 313 (2000).

[29] C. W. Bauer, D. Pirjol, I. Z. Rothstein, and I. W. Stewart, Phys. Rev. D **70**, 054015 (2004).

[30] G. Buchalla, A. J. Buras, and M. E. Lautenbacher, Rev. Mod. Phys. **68**, 1125 (1996).

[31] F. Su, Y.-L. Wu, Y.-B. Yang, and C. Zhuang, Journal of Physics G: Nuclear and Particle Physics **38**, 015006 (2011).

[32] S. Glashow., Nucl. Phys. **22**, 579 (1961).

[33] T. M. M. Kobayashi. Prog. Theor. Phys. **49**, 652 (1973).

[34] L. C. et. al., Phys. Rev. D **43**, 2176 (1991).

[35] S. L. Glashow and E. E. Jenkins, Physics Letters B **196**, 233 (1987).

[36] R. Barbieri and G. Giudice, Physics Letters B **309**, 86 (1993).

[37] M. Acciarri et al., Physics Letters B **363**, 127 (1995).

[38] J. Brodzicka et al., Prog. Theo. Expt. Phys. **1**, 04D001 (2012).

[39] M. Kobayashi and T. Maskawa, Prog. Theo. Phys. **49**, 652 (1973).

[40] S. Kurokawa and E. Kikutani, Nucl. Instrum. Meth. Phys. Res., Sect. A **499**, 1 (2003).

[41] A. Abashian et al., Nucl. Instrum. Meth. Phys. Res., Sect. A **479**, 117 (2002).

[42] Z. Natkaniec et al., Nucl. Instrum. Meth. Phys. Res., Sect. A **560**, 1 (2006).

[43] H. Hirano et al., Nucl. Instrum. Meth. Phys. Res., Sect. A **455**, 294 (2000).

[44] T. Iijima et al., Nucl. Instrum. Meth. Phys. Res., Sect. A **453**, 321 (2000).

[45] H. Kichimi et al., Nucl. Instrum. Meth. Phys. Res., Sect. A **453**, 315 (2000).

[46] K. Miyabayashi, Nucl. Instrum. Meth. Phys. Res., Sect. A **494**, 298 (2002).

[47] R. Akhmetshin et al., Nucl. Instrum. Meth. Phys. Res., Sect. A **455**, 324 (2000).

[48] M. Yamaga et al., Nucl. Instrum. Meth. Phys. Res., Sect. A **456**, 109 (2000).

[49] A. Abashian et al., Nucl. Instrum. Meth. Phys. Res., Sect. A **449**, 112 (2000).

[50] Y. Ushiroda et al., Nucl. Instrum. Meth. Phys. Res., Sect. A **438**, 460 (1999).

[51] T. Ziegler et al., Nucl. Sc., IEEE Trans. **51**, 1852 (2004).

[52] D. J. Lange, Nucl. Instrum. Meth. Phys. Res., Sect. A **462**, 152 (2001).

[53] S. Agostinelli et al., Nucl. Instrum. Meth. Phys. Res., Sect. A **506**, 250 (2003).

[54] R. Brun, R. Hagelberg, M. Hansroul, and J. Lassalle, CERN Rep. CERN-DD-78-2 (1978).

[55] R. Brun, F. Bruyant, and M. Marie, Appl. Software Group. CND.-1994 (1995).

[56] K. Hanagaki et al., Nucl. Instrum. Meth. Phys. Res., Sect. A **485**, 490 (2002).

[57] G. C. Fox and S. Wolfram, Phys. Rev. Lett. **41**, 1581 (1978).

[58] R. J. Barlow, *Statistics: a guide to the use of statistical methods in the physical sciences*, volume 29, John Wiley & Sons, 1989.

[59] R. J. Barlow et al., BABAR analysis document **318** (2002).

[60] W. R. Leo, *Techniques for nuclear and particle physics experiments: a how-to approach*, Springer, 1994.

[61] W. Verkerke and D. Kirkby, RooFit Users Manual v2. 91, Document version (2008).

[62] B. John et al., BABAR analysis document **18** (2001).

[63] F. James and M. Winkler, Minuit user2s guide, CERN (2004).

[64] F. James et al., Function Minimization and Error Analysis, Version **94** (1994).

[65] A. Lazzaro and L. Moneta, MINUIT package parallelization and applications using the RooFit package, in *Journal of Phys.: Conf. Series*, volume 219, page 042044, IOP Publishing, 2010.

[66] F. James and M. Roos, Comp. Phys. Comm. **10**, 343 (1975).

[67] B. Bhuyan, High P_T Tracking Efficiency Using Partially Reconstructed D^* Decays, Belle Note **1165**.

[68] M.-C. Chang et al., Phys. Rev. D **85**, 091102 (2012).

[69] A. Drutskoy et al., Phys. Rev. Lett. **98**, 052001 (2007. This result is obtained by Belle using 121.4 fb^{-1} of $\Upsilon(5S)$ data and the method described in this paper.).

[70] S. Esen et al., Phys. Rev. D **87**, 031101 (2013).

[71] R. Louvot et al., Phys. Rev. Lett. **102**, 021801 (2009.This result is obtained by Belle using 121.4 fb^{-1} of $\Upsilon(5S)$ data and the method described in this paper.).

[72] A. Abdesselam et al., (2016).

[73] U. Y. Insoo Lee and B. Cheon, (2016).

[74] H. Albrecht et al., Phys. Lett. **B241**, 278 (1990).